THE DYNAMICS AND PREDICTABILITY OF RAINFALL PRODUCING SYSTEMS IN THE SOUTH AFRICAN DOMAIN

Report to the
Water Research Commission

by

Thando Ndarana[a], Tsholanang Rammopo[a], Donald Nkabinde[a], Mary Jane Bopape[b], Siyabonga Mpati[a,b], Patience Mulovhezi[b] and Mthobisi Nxumalo[b]
[a]Department of Geography, Geoinformatics and Meteorology, University of Pretoria
[b]Research and Innovation Department, South African Weather Service

WRC Report No. 2829/1/21
ISBN 978-0-6392-0270-9

August 2021

UNIVERSITEIT VAN PRETORIA
UNIVERSITY OF PRETORIA
YUNIBESITHI YA PRETORIA

WATER
RESEARCH
COMMISSION

Obtainable from:
Water Research Commission
Private Bag X03
Gezina,
PRETORIA, 0031

orders@wrc.org.za or download from www.wrc.org.za

DISCLAIMER

This report has been reviewed by the Water Research Commission (WRC) and approved for publication. Approval does not signify that the contents necessarily reflect the views and policies of the WRC nor does mention of trade names or commercial products constitute endorsement or recommendation for use.

EXECUTIVE SUMMARY

1. Project rationale

Research that focused on the dynamics and predictability of weather systems was a prominent component of the 10-tear THe Observing System Research and Predictability Experiment (THORPEX) of the World Meteorological Organisation (WMO). THORPEX was conducted from 2004 to 2014. Many of the dynamical process and predictability research questions that were highlighted by that project have not been addressed in the South Atlantic Ocean/Southern African domain. This is largely due to the fact that over South Africa the research into dynamics and predictability that have not yet received much attention during the last few decades are those that occur at the medium-range forecasting (MRF) time scale, which, according to the WMO, is forecasting with lead times between two to ten days ahead. Experience in this area of meteorological activities in South Africa has largely been operational rather than research-focused.

MRF is an initial value forecasting problem, during which the forecast skill (and therefore predictability of synoptic weather systems) diminishes exponentially by the end of the ten-day cut-off period. This reduction in forecast skill has been attributed to inadequate observations that have errors, imperfect numerical weather prediction model physics and poorly understood dynamical processes that underlie the evolutions of the weather systems. Based on these problems aforementioned, the motivation behind this project was that to improve the predictive forecast skill at this MRF time scale, it is necessary to identify and understand the dynamical processes that precede the weather systems of interest. In the case of this project, the weather systems of interest were the ridging South Atlantic anticyclones and the cut-off low (COL) pressure systems. The former is not, by itself a rainfall producing system, but it plays a central role in transporting moisture into South Africa from the Southwest Indian Ocean. The COLs are often combined with these ridging highs to produce rainfall over South Africa. In some cases, the rainfall events that are associated with these systems can lead to flood, extensive damage to property and loss of life. It is therefore necessary to improve their predictability at the MRF time scale so that more reliable (or improved) early warning systems can be developed.

Based on the above, the specific objectives of the project were

1. To implement the latest bias correction measures in NCEP EPS data;
2. To develop objective methods for identifying rainfall producing systems and establish their dynamical processes;
3. To develop an automated scheme that will identify specific rainfall producing systems in NCEP EPS forecast products; and
4. To assess the value added by incorporating dynamic meteorology knowledge to the predictability of rainfall producing systems at the MRF time scale.

2. Results and conclusions

The project showed that ridging high pressure systems are regulated by large scale Rossby wave packets that develop in the South American region. These wave packets propagate in a north-easterly direction to reach South Africa and appear to be reflected there. Embedded in these Rossby waves are breaking processes that are most clearly seen by examining potential vorticity contours on isentropic surfaces. The Rossby waves break as ridging occurs, and bring about the high potential vorticity anomalies that are communicated to the surface, via vertical coupling, to induce the ridging process. Wave breaking precedes the ridging process. In this project, through quantification, we could determine how the ridging high pressure system brings moisture into the South African mainland. Here dynamic meteorology knowledge was exploited to show that ageostrophic and geostrophic components of the horizontal flow bring moisture into South Africa from different parts of the South Indian Ocean. In case of the former, the moisture appears to originate from the ocean waters that are adjacent to the country and the associated fluxes then enter the country south of the 30°S longitude line and follow the geometry of the eastern coast. The geostrophic moisture fluxes dominate further north. This branch of moisture flux breaks into two, with one component transporting the moisture towards Botswana and Namibia in a cyclonic fashion while the other component turns anticyclonically around the continental high of the northeast of South Africa.

About a decade before the time of writing this report, wave breaking was shown to be responsible for bringing about the high potential vorticity anomaly that induces the cyclonic circulation and therefore precedes the formation of these systems. In this project, the dynamics of the jet streaks that bring about the flow conditions that induce the wave breaking were explained. The eastward propagation of the jet streak is caused by the zonal flow redistribution of momentum from the jet entrance to the exit, where the diffluent flow is found. The jet streak that is associated with COLs also changes orientation as it is propelled eastward. This is caused by the poleward (equatorward) advection of zonal momentum at the jet entrance (exit). These meridional zonal momentum patterns are induced by the transverse thermally direct and indirect circulations at the jet entrance and exit, respectively. The movement of the jet is tightly coupled to the evolution of the eddy kinetic energy, which describes the downstream development mechanism that precedes COLs. This mechanism is facilitated by the downstream energy transfer that is made possible by the breaking waves, thus clarifying the role of Rossby wave breaking in the formation of COLs, in addition, it brings about the potential vorticity anomaly.

Characteristics of Rossby wave packets (RWPs) affecting South African weather processes have been examined and diagnosed objectively from the latest filtered finite-amplitude wave activity diagnostic (FAWA) in isentropic coordinates. The morphological characteristics of such RWPs were established. It was found that the evolution of RWPs in question is consistent with the known life-cycle of baroclinic RWPs. The development phase involved the north-eastward propagation of an initial disturbance, followed by zonal propagation briefly before the onset of the termination stage indicated by Rossby wave breaking. Subsequently, the RWP propagates approximately south-eastward. In addition, the climatology of RWPs revealed that most events occur during the transition seasons, with a majority of the events being detected within the South Indian Ocean domain. The evolutionary characteristics of RWPs were also analysed using an eddy kinetic energy (EKE) diagnostic. The EKE evolution essentially diagnoses the ensuing downstream development associated with baroclinic waves. Key processes involved in the evolution of the EKE structure were found to be a baroclinic conversion and the divergence of the ageostrophic geopotential fluxes. The utility of RWPs as a diagnostic tool was explored through two examples. The first showed that the onset of 11 composited heatwave events was preceded by a pre-existing RWP structure located in the vicinity of the SACZ. Furthermore, it was shown that the 22 April 2019 cut-off low event was also associated with a RWP that developed at an earlier time upstream. It was shown that the ensemble mean of a forecast issued on 14 April 2019 at 00Z by the NCEP EPS system revealed the development of the RWP at about t = + 96 hours of the forecast window.

The project presented an opportunity for developing objective methods for identifying the ridging high and COL pressure systems. These methods were then implemented in MRF data, which enabled event-based forecasts at this time scale. In this way, the skill of the MRF EPS to actual weather system event can be easily assessed. The use of mathematical diagnostics to understand the dynamical processes that precede the weather systems also presented an opportunity to add value to the MRF data, so that wave breaking that precedes ridging highs and COLs, as well as downstream development, can then be objectively predicted.

3. Recommendations

1. The understanding of the dynamical processes that precede South African weather systems is far from complete. A follow-up study is required in order to systematically undertake this task.
2. This project showed that there is potential for improving the predictive skill of rainfall producing systems over South Africa by means of implementing dynamic meteorology knowledge in the forecasts. A proper systematic assessment of the improvements in forecast skill should be undertaken, using an extensive dataset. This was a severe limitation in this project due to data storage facilities and bandwidth.
3. Objective event-based MRF forecasting methods should be investigated and developed for South Africa.

4. Knowledge dissemination

1. The following publications were produced from the project
   (a) Ndarana, T., Bopape, M., Waugh, D., and Dyson, L. (2018). The influence of the lower stratosphere on ridging Atlantic Ocean anticyclones over South Africa. *Journal of Climate* 31: 6175-6187.
   (b) Ndarana, T., Mpati, S., Bopape, M., Engelbrecht, F., and Chikoore, H. (2021). The flow and moisture fluxes associated with ridging South Atlantic Ocean anticyclones during the subtropical southern African summer. *International Journal of Climatology*. 41: E1000-E1017.
   (c) Ndarana, T., Rammopo, T.S., Bopape, M., Reason, C. and Chikoore, H. (2021). Downstream development during South African cut-off pressure systems. *Atmospheric Research*, 249, 105315.
   (d) Ndarana, T., Rammopo, T.S., Chikoore, H., Barnes, M.A. and Bopape, M. (2020). A quasi-geostrophic diagnosis of cut-off low pressure systems over South Africa and surrounding ocean. *Climate Dynamics*. 55, 2631-2644.
2. The following publications are under construction
   (a) Rammopo, T.S. and Ndarana, T. (2021). The characteristics of Rossby wave packets dissipating over South Africa. To be submitted to *Climate Dynamics.*
   (b) Rammopo, T.S. and Ndarana, T. (2021). Investigating the relationship between Rossby wave packets and weather systems over South Africa. To be submitted to *Atmospheric Research.*

5. Acknowledgements

1. Dr B. Petja for the efficient management of the project and interest in the work.

2. The authors also thank the Project Steering Committee for their guidance during the course of the project: Prof B. Abiodun, Prof R. Burger, Prof H. Chikoore, Dr S. Hatchingota, Dr C. Lennard, Mr R. Maisha and Dr M. Mdoka.

TABLE OF CONTENTS

LIST OF FIGURES

LIST OF ABBREVIATIONS

00:00 UCT	:	(00:00) Greenwich Mean Time, (UCT) Coordinated Universal Time
AWB	:	Anticyclonic (Rossby) wave breaking
COL	:	Cut-off low
DJF	:	December-January-February
DoE	:	U.S. Department of Energy
E	:	East
ECMWF	:	European Centre for Medium-Range Weather Forecasts
EKE	:	Eddy kinetic energy
EPS	:	Ensemble prediction system
ERA-Interim	:	**A** global atmospheric reanalysis dataset from 1 January 1979 to 31 August 2019
ETKF	:	Ensemble Transform Kalman Filter
FAWA	:	Finite Amplitude Wave Activity
ITCZ	:	Inter-Tropical Convergence Zone
JJA	:	June-July-August
JRA-55	:	Japanese 55-year reanalysis
LC1	:	Life Cycle 1
LC2	:	Life Cycle 2
MAM	:	March-April-May
MATLAB	:	Matrix Laboratory
MRF	:	Medium-range forecasting
MRF EPS	:	Medium-range forecasting ensemble prediction system
MSLP	:	Mean surface level pressure
NCEP	:	National Centres of Environmental Prediction – U.S.
NCEP DoE AMIP II	:	National Centres for Environmental Prediction – U.S. Department of EnergyAtmospheric Model Intercomparison Project 2
NCEP EPS	:	National Centres of Environmental Prediction Ensemble prediction system
NCEP GEPS	:	National Centres of Environmental Prediction Canadian Global Ensemble Prediction System
NOAA	:	National Oceanic and Atmospheric Administration (U.S. Department of Commerce)
NVA	:	Negative vorticity advection
NWP	:	Numerical Weather Prediction
PV	:	Potential vorticity
RMSE	:	Root mean square error
RWB	:	Rossby wave breaking

RWB (AWB)	:	Rossy wave breaking (anticyclonic wave breaking)
RWP	:	Rossby wave packet
SA	:	South Africa
SACZ	:	South African Convergence Zone
SAT	:	South Atlantic domain
SAWS	:	South African Weather Service
SH	:	Southern Hemisphere
SH FAWA	:	Southern Hemisphere Finite Amplitude Wave Activity
SI	:	South Indian Ocean domain
SON	:	September-October-November
SSA	:	South of South Africa
SWIO	:	Southwest Indian Ocean
THORPEX	:	THe Observing system Research and Predictability EXperiment
VAC	:	Vorticity advection convergence
VAD	:	Vorticity advection divergence
W	:	West
WMO	:	World Meteorological Organisation
WWRP	:	World Weather Research Programme

This page was intentionally left blank

1

Introduction

1.1 Background

The atmospheric prediction problem is divided into time scales, depending on the lead time[1] involved. There is the nowcasting time scale, which is the prediction of weather phenomena up to a few hours ahead. Next, the lead time that is associated with short-range forecasts is between approximately 12 hours up to two days. Then medium-range forecasting (MRF) takes over from the short-range to predict phenomena that would occur between two days and ten days. Forecasting at these time scales is an initial value problem because the current or initial state of the atmosphere must be established. This is done by continuously observing the atmosphere and then integrating these observations into the operational forecasting process, either subjectively by means of synoptic analysis in the case of subjective weather forecasting or objectively into numerical weather prediction (NWP) systems through sophisticated data assimilation methods. This information is then integrated forward in space and time. This integration requires knowledge of the physical laws, such as the conservation of momentum, energy and mass (Holton and Hakim, 2014), which are formulated as partial differential equations and solved numerically to produce dynamical cores of NWP models. These models are central to our ability to produce forecasts at the short to medium-range time scales (Bauer et al., 2015). Beyond ten days atmospheric prediction gradually becomes a boundary value problem, with the slowly varying conditions such as sea surface temperatures, soil moisture and sea-ice progressively becoming more important.

For lead times up to ten days ahead, aspects of atmospheric predictability come from initial atmospheric conditions, and it diminishes exponentially as a function of lead-time (see Figure 1.1). Therefore errors in atmospheric observations, a lack of them and how they are assimilated into NWP systems all have implications to the predictability of weather phenomena at the nowcasting to MRF time scales. They may improve or limit predictability depending on how accurate they are or how sophisticated or advanced the assimilation methods are. Another source of limitations to predictability at these time scales is an incomplete understanding of physical processes that underlie the dynamical evolution of the weather systems that are predicted. It follows then improving the understanding of these dynamical processes and incorporating this information into forecasting systems is one area that could be exploited in order to improve the predictability of weather processes, and in particular that of rainfall producing synoptic weather systems. In fact, research on the dynamics and predictability of midlatitude weather systems was a major component of the 10-year World Meteorological Organization (WMO)/World

[1] Lead time: The time between the present and the point at which the event of interest is supposed to take place

Weather Research Programme (WWRP) THe Observing System Research and Predictability EXperiment (THORPEX); that was conducted from 2004 to 2014 (Gray and Wernli, 2015; Parsons et al., 2017). Such research activities, and outputs therefrom, are the most feasible way for improving forecast skill for countries in which there is little data assimilation and ensemble system development capability for MRF.

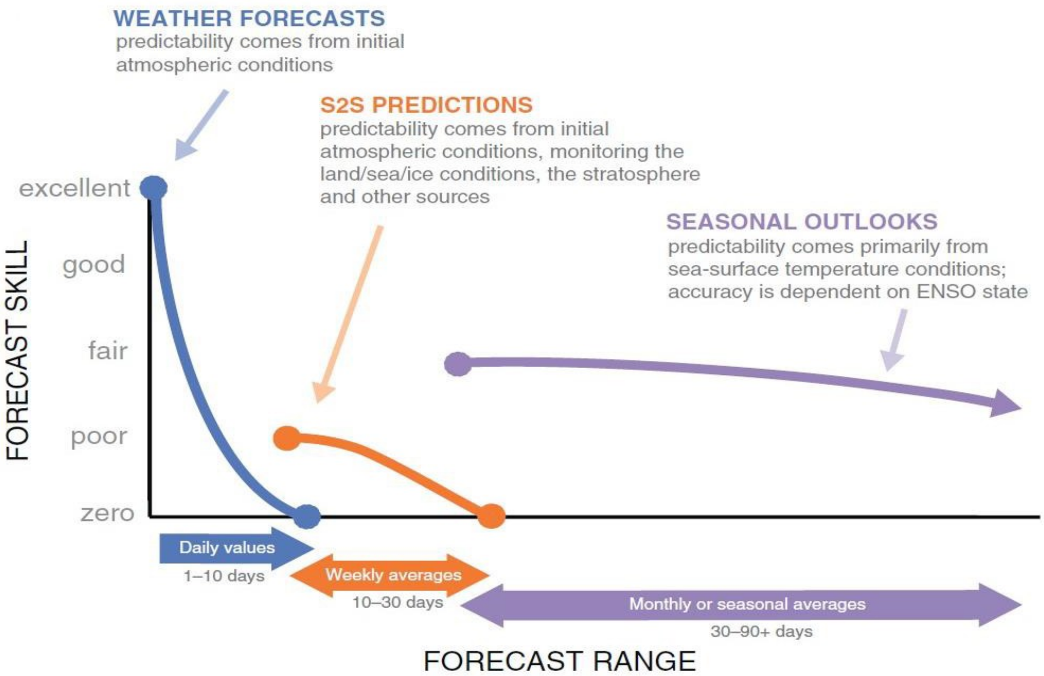

Figure 1.1: *Schematic representation of forecast skill based on forecast range from short-range weather forecasts to long-range seasonal predictions, including potential sources of predictability (Adapted from White et al., 2017).*

South Africa has a relatively long history of MRF activities (Tennant et al., 2007). Most of the operational and research experience in this area can be found at the South African Weather Service (SAWS). Output from National Centres for Environmental Prediction (NCEP) Ensemble Prediction Systems (EPS) that are downloaded operationally from the NOAA Operational Model Archive and Distribution System [2] and post-processed to provide guidance to operational weather forecasters. These data also used to develop weather forecast products that can be consumed by the public and industry, thus contributing to ”weather smart” decision making processes. Also one of the main contributions of MRF is in the area of early warning systems. The effectiveness of such early warning systems depends heavily on how predictable the weather systems that bring about extreme weather are at this time scale. Whilst there is experience needed in using these MRF products in the country, the question of the predictability of the weather systems that produce rainfall over South Africa remains unattended.

There is also extensive experience of synoptic meteorology in South Africa. Forecasters employ their expert knowledge of the subject, experience and NCEP EPS data to produce MRF forecast products in the country. By its very nature, synoptic meteorology is difficult to objectively operationalize, except in special circumstances when a weather system can be identified objectively in gridded datasets. If this is assumed as feasible, then implementing operational dynamical meteorology diagnostics becomes possible, which can add value to the EPS products to give credence to forecasts of the weather systems

[2] https://nomads.ncep.noaa.gov/

which they precede, thus contributing to improved predictability of these weather systems. Therefore, the overall aim of the project was to address these issues, which requires that the systems be objectively identified in EPS output, after having been dynamically characterised in ”observational” datasets such as reanalysis products.

1.2 Project objectives

Based on the research problem outlined in Section 1.1, the specific objectives of the project were to

1. To implement the latest bias correction measures in NCEP EPS data;
2. To develop objective methods for identifying rainfall producing systems and establish their dynamical processes;
3. To develop an automated scheme that will identify specific rainfall producing systems in NCEP EPS forecast products; and
4. To assess the value added by incorporating dynamic meteorology knowledge to the predictability of rainfall producing systems at the MRF time scale.

1.3 Organisation of the report

- Chapter 2 outlines a bias correction measure and assess its impact on the forecast skill.
- Chapters 3 and 4 present the dynamics of ridging high pressure systems and assess the ability to predict them better, given the new dynamical meteorology knowledge associated with them. Building on a previous finding that relates cut-off low pressure systems to the so-called Rossby wave breaking, the latter is shown to precede ridging high pressure systems and that it is central to downstream development that is associated with cut-off lows.
- In Chapter 5 a more general approach to precursors of South African weather, namely Rossby wave packets, is considered.
- Concluding remarks and recommendations for further research are presented.

2

Bias correction of NCEP EPS data

2.1 Background

As noted in the previous chapter, NWP models are based on numerical solutions to partial differential equations. This means that the variables from these solutions can only be available at discrete points in space and time (i.e. in four dimensions) in the Earth's atmosphere. Depending on the grid spacing (which is sometimes referred to as model resolution), it is inevitable that some of the important processes, such as cumulus convection (and other mesoscale processes) might not be resolved by these models, which gives rises to the parameterization of these processes (e.g. Krasnopolsky et al., 2005). This, combined with initial conditions that are imperfect because of instrument and human errors, inadequacy of coverage of that observations through the initial conditions are created, data assimilation systems that are sophisticated but require further improvements (e.g. Kalnay, 2002) and limitations to computation resources, models suffer from biases that contaminate the forecasts they produce. This gives rise to the need for bias correction measures to be implemented, such as the one that is currently in operational use at the SAWS (Tennant et al., 2007).

2.2 Bias correction

The bias correction chosen is the decaying average method (Cui et al., 2012), which is an autoregression scheme (Du and Zhou, 2011). It is applied to raw NCEP GEPS standard output available daily at 00:00, 06:00, 12:00 and 18:00 UCT (Hamill et al., 2013) from 01 November 2018 to 30 April 2019 (the 2018/2019 summer seasons). The data are available at 1° resolution at standard pressure levels, from 1000 hPa to 10 hPa. In the interest of disk space, only the 00:00 UCT runs were downloaded and used in this study. The NCEP GEPS produces 14 ensemble-member forecasts daily at 6 hourly intervals up to 384 hours (16 days) ahead. Only the analysis (00 hours run), the 6, 42, ..., 384 hour forecasts are available for download from the server.

The bias correction is implemented in steps. Following Cui et al. (2012) the first step is to estimate the bias $b(i,j,t)$ at each grid point (i,j) and lead time t (see Equation 2.1). It is defined as the difference between the analysis $a(i,j,t)$ and the forecast $f(i,j,t)$, as follows

$$b(i,j,t) = f(i,j,t) - a(i,j,t) \tag{2.1}$$

Note the analysis used is the latest available one and the forecast is the one that is valid at that time. As an example, consider forecasts produced on the 00:00 UCT 02 November 2018. The analysis fields are the initial conditions produced on this date and on the basis of which of the forecasts are produced. Therefore at each forecast hour for this day, the analysis is subtracted. This is done for all the dates during the 2018/2019 summer season.

Unlike Du and Zhou (2011) and Cui et al. (2012), in the second step more emphasis is put on the latest error so that the bias estimate at time t is then calculated by updating the average bias $B(i,j,t)$ using

$$B(i,j,t) = wB(i,j,t-1)+(1-w)b(i,j,t) \tag{2.2}$$

where $B(i,j,t-1)$ is the bias from the previous forecast hour and $b(i,j,t)$ is the current bias. Experimentation with various values of w showed that this form of the bias estimate reduced the bias (which is the difference between the correct/uncorrected forecast and the latest analysis) by a factor of ten and w = 0.1 was chosen. Equation 2.2 allows the incorporation of the most recent behaviour of weather systems to the current state of the atmosphere as forecast (Cui et al., 2012). The use of $B(i,j,t-1)$ means that the bias estimate must be initialised. Given the data that is available, bias correction begins at t = 48 hours and therefore the initial value of B is obtained by

$$B(i,j,42\text{ hours}) = f(i,j,42\text{ hours})-A(i,j) \tag{2.3}$$

where $A(i,j)$ is the analysis for that day. In calculating B, after having initialised it as described above, leading to the final step of bias correcting the forecasts using

$$F(i,j,t) = f(i,j,t)-B(i,j,t) \tag{2.4}$$

where $F(i,j,t)$ is the bias corrected forecast, at each lead time t.

Given the need to initialise the decaying average B, the actual bias correction begins at t = 42 to 384 hours, in 6 hourly increments. However, the opportunity to verify the two sets of forecasts only occurs at 48 to 384 hours at only 24 hour intervals. The reason for this is that the analyses against which the verification statistics may be calculated are only available at these intervals. For example, the 48 hour forecast produced on 00:00 02 November 2018 is verified against the analysis of the forecast generated 00:00 UCT 04 November 2018, the 72 hour forecast is verified against the analysis of the 00:00 UCT05 November 2018, and so on.

2.3 Forecast verification

To demonstrate the impact of the bias correction procedure that was presented in the previoussubsection, we present the spatial bias before and after correction in Figure 2.1 for ensemble mean forecasts of 500 hPa geopotential height fields. Only the T + 48, 144, 240 and 366 hours are shown. The spatial bias is calculated by subtracting the latest available analysis fields from the forecasts, as inEquation 2.1 above for both the uncorrected and corrected forecasts. It is clear that the proposed post-processing procedure reduced the model bias by a factor of ten.

Before bias correction, the NCEP GEPS tends to over forecast the geopotential height fields in the midlatitudes, just south of South Africa. As shown by inspecting the left panels of Figure 2.1 from top

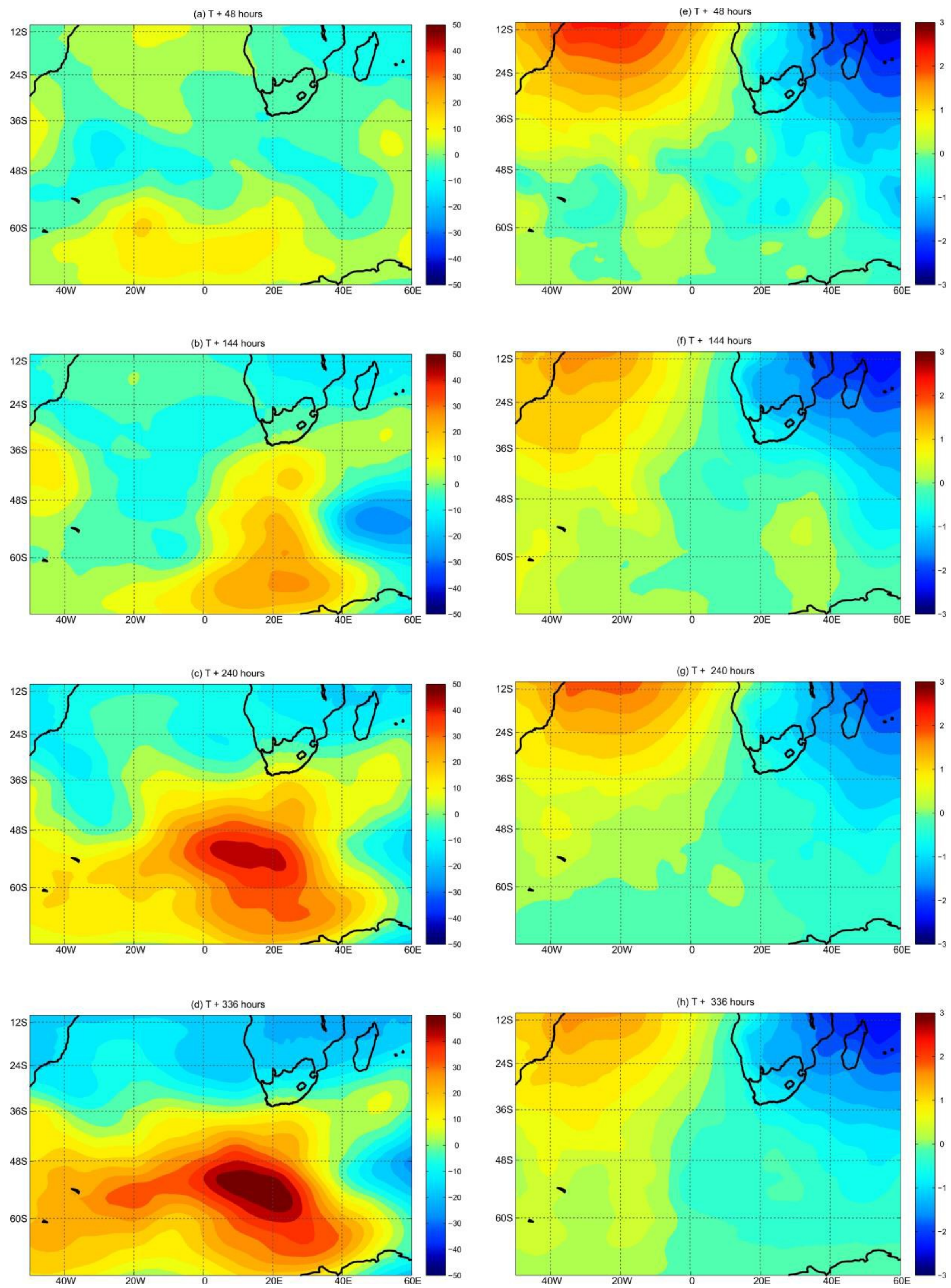

Figure 2.1: *Ensemble mean spatial bias for the uncorrected (left panels: (a) to (d) and corrected (right panels: (e) to (h)) NCEP GEPS forecasts of geopotential heights at 500 hPa. The spatial bias is shown for (a,e) T + 48 hours, (b,f) T + 144 hours, (c,g) T + 240 hours and (d,h) T + 366 hours.*

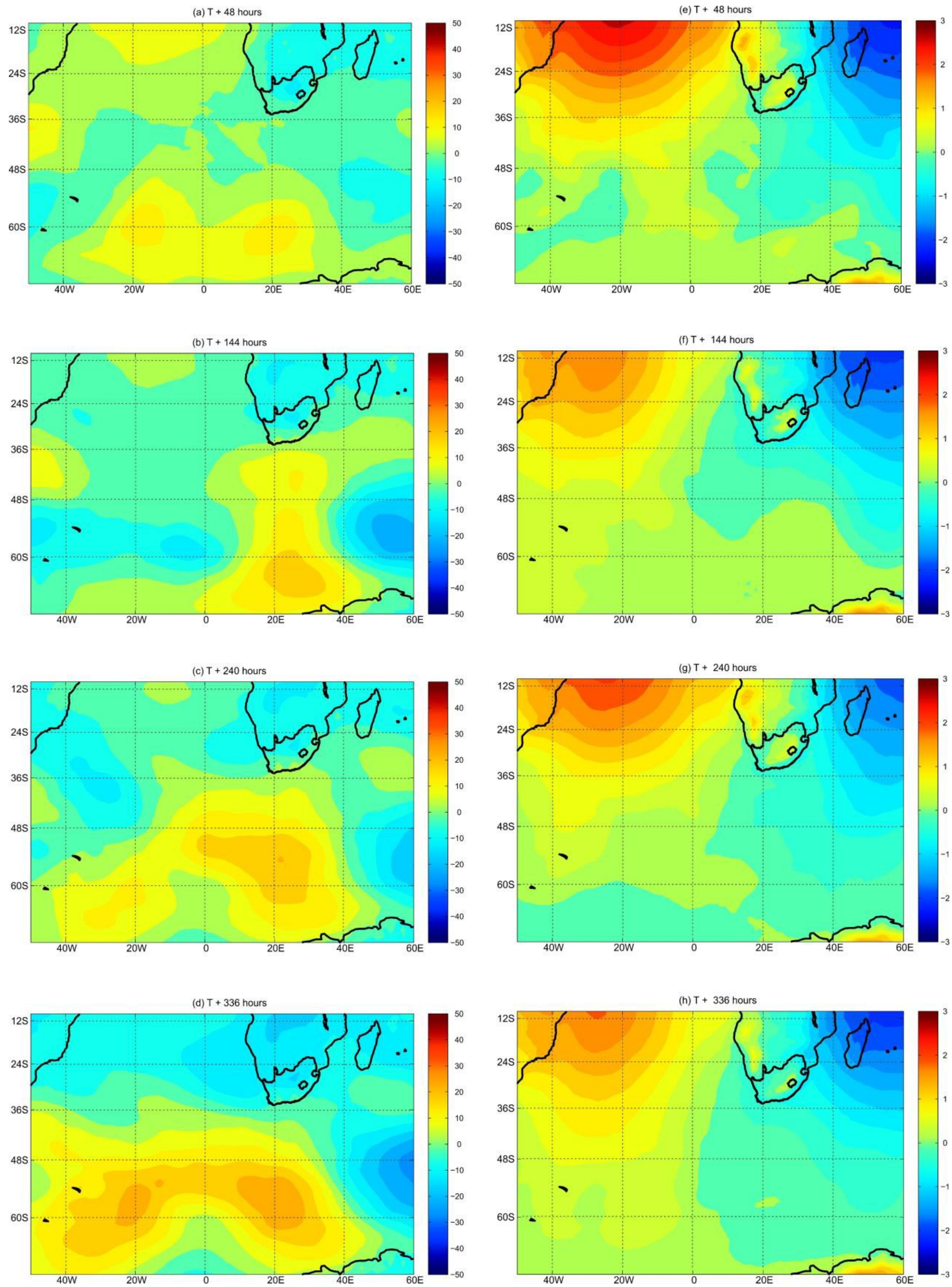

Figure 2.2: *Same as in Figure 2.1, but for 850 hPa geopotential heights.*

to bottom, the model bias tends to amplify, with time. As will be shown in the coming chapters, South African weather systems are affected by large scale processes such as Rossby wave trains that propagate from the South American region towards South African and then along the midlatitude wave guide (Ambrizzi et al., 1995) towards Australia. For this reason, these model deficiencies are not desirable as they can be expected to contaminate the forecasts of rainfall producing systems over the country. The version of the Cui et al. (2012) bias correction procedure that has been implemented in this project removed this error almost entirely. It, however, introduces a new area of systematic biases in the tropics. This is not a major concern because as noted, South African rainfall producing systems are mostly affected by midlatitude dynamical processes. As these midlatitude processes are baroclinic in nature, that is to say, that surface processes such as heat fluxes, affect the upper echelons of the troposphere, via wave activity propagation during baroclinic life cycles (Thorncroft et al., 1993), it is also important to examine surface fields. Figure 2.2 shows the spatial bias of the 850 hPa NCEP GEPS forecasts for the same forecast lead times that are shown in Figure 2.1. Again, there is a clear positive bias in the geopotential height fields, even though it does not appear to intensify immediately south of the country, it does appear to do so at about 60°S and 20°S, which is a region of high cyclogenesis activity (Sinclair, 1995; Reboita et al., 2010).

In the next chapters, weather systems such as ridging high and cut-off low pressure systems will be characterised, the interest will be on those systems that enter the southern African domain. This is defined as the region bounded by 10-40°E longitude and 20-40°S latitude, as in Singleton and Reason (2007), in their study of cut off lows over southern Africa. Also as indicated by Figures 2.1 and 2.2, another region of interest is clearly over the Southern Atlantic and Southwest Indian Oceans, which is bounded by 50°W to 60°E and 35°S to 70°S. These domains will be referred to as the land and marine domains, respectively, for brevity.

The root mean square error (RMSE) graphs for the whole, marine and land domains are shown in Figure 2.3. The EPS model bias increases significantly with increasing lead time. This is largely due to the fact that the validity of the initial conditions wane as the model is integrated into the future, as these

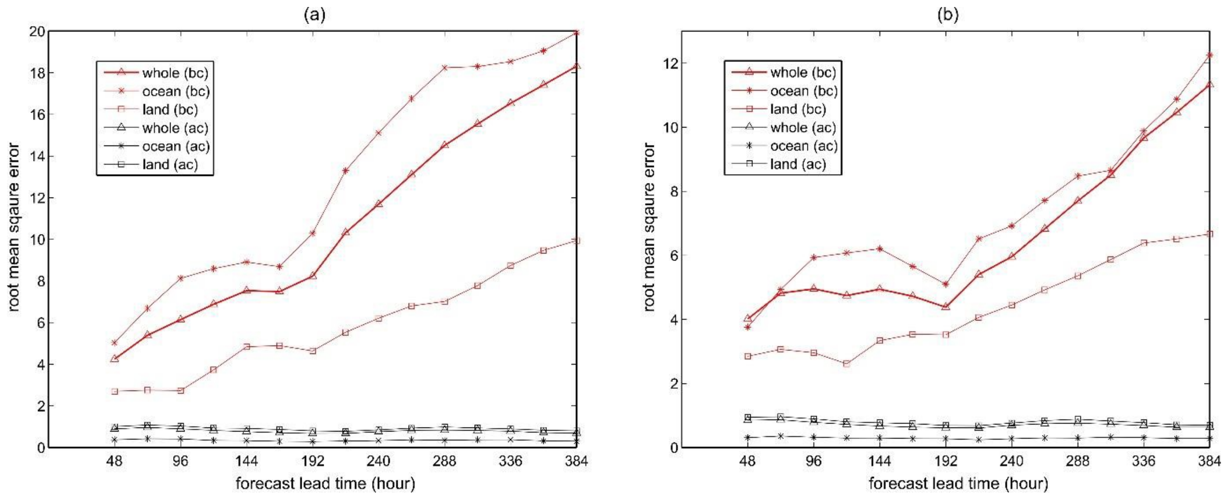

Figure 2.3: *Root mean square error (RMSE) for geopotential heights at (a) 200 hPa and (b) 850 hPa. The symbols "bc" (red curves) and "ac" (black curves) in the brackets stand for "before correction" and "after correction", respectively. The RMSE is presented by the whole domain, for land (bounded by 10-40°E longitude and 20-40°S latitude), ocean (50°W to 60°E and 35°S to 70°S). These are represented by curves with stars, triangles and squares, respectively.*

conditions cannot be updated once the model run has been initiated. Over the ocean, the model bias is much larger than over land. This could be caused by the fact that there are more in situ observations on land. The bias correction improves the RMSE of the model quite significantly, particularly over the oceans. This is a critical observation as we require that fields in the middle latitudes be accurate there.

2.4 Summary

The Cui et al. (2012) bias correction procedure, to the extent of the available data, has shown to be effective in removing the model biases in the South African domain and surrounding oceans. It was shown in this chapter, as would be expected because of the lack of observations there, that there are much larger model biases over the oceans than over land. If not removed, these errors would propagate into the South African domain from the South Atlantic Ocean, most likely through Rossby wave trains (Gray and Wernli 2015), and contaminate the EPS forecast, particularly at larger lead times. These larger are precisely when the EPS forecast needs to be improved to produce reliable early warning systems. It will be shown in the following chapters that the most important weather systems that bring rainfall over South Africa are regulated by these Rossby wave trains (wave packets) and therefore the errors, if not removed, could limit the predictability of the systems. The strength of the Cui et al. (2012) procedure is its simplicity and does not require large archives of data to be successfully implemented. It can therefore be easily operationalized.

3

Ridging high pressure system

Chapter 3 is based on the following research outputs and funded by this project:

- Ndarana, T., Bopape M., Waugh D., and Dyson L. (2018) The influence of the lower stratosphere on ridging Atlantic Ocean anticyclones over South Africa. *Journal of Climate* 31: 6175-6187.
- Ndarana, T., Mpati, S., Bopape, M., Engelbrecht, F., and Chikoore, H. (2021). The flow and moisture fluxes associated with ridging South Atlantic Ocean anticyclones during the subtropical southern African summer. *International Journal of Climatology*. 41: E1000-E1017.

3.1 Background

The prerequisite to understanding rainfall at synoptic time scales in a particular region is understanding where the moisture comes from and the associated mechanisms that generate it. South Africa is primarily a summer rainfall country (Roffe et al., 2019) with a pronounced zonal gradient where most of the rainfall occurs over the eastern parts of the country, as seen in many classic reviews of South African meteorology (see Taljaard and van Heerden, 1998; Tyson and Preston-Whyte, 2000). The western and Southwestern parts of South Africa receive rainfall during the winter months (Weldon and Reason, 2014) with cold fronts that are associated with midlatitude cyclones being the main rainfall bearing systems. The south coast is an all-season rainfall region (Engelbrecht et al., 2015). During the summer months, the main systems that bear rainfall are the upper air westerly troughs (Favre et al., 2013) that sometimes develop into cut-off low pressure systems (Singleton and Reason, 2007; Favre et al., 2013). These upper level westerly waves may combine with tropical disturbances as the Inter-Tropical Convergences Zone (ITCZ) migrates southward (Suzuki, 2011) to form the tropical temperate troughs (TTTs; Fauchereau et al., 2009; Hart et al., 2010; Ratna et al., 2013; Macron et al., 2014). Other important rain-bearing systems are the tropical lows (Malherbe et al., 2012; Rapolaki et al., 2019), which is the often devastating tropical cyclone. All of these are of synoptic scale but some of the rainfall comes from thunderstorms. These rain-bearing systems are mesoscale in spatial extent (Markowski and Richardson, 2010), with convective complexes contributing about 20% to the total summer rainfall (Blamey and Reason, 2012) of the country. These systems provide the lifting mechanisms that are required for rainfall to occur but do not on their own bring the moist air.

Part of the moisture that South Africa needs for rainfall has its sources in the tropical regions, both from the Equatorial South Atlantic (Vigaud et al., 2009) and Indian Oceans (D'Abreton and Lindesay, 1993;

D'Abreton and Tyson, 1995). These studies showed that moisture originates from the moisture divergence on either side of the continent and travels towards southern Africa in a manner consistent with the cyclonic flow that is associated with the Angola low (Mulenga, 1998; Rounalt et al., 2003; Cook et al., 2004; Reason and Jagadheesha, 2005; Howard and Washington, 2018). In fact, the variability in the strength of the Angola low determines the amount of moisture that eventually becomes available for cloud bands.

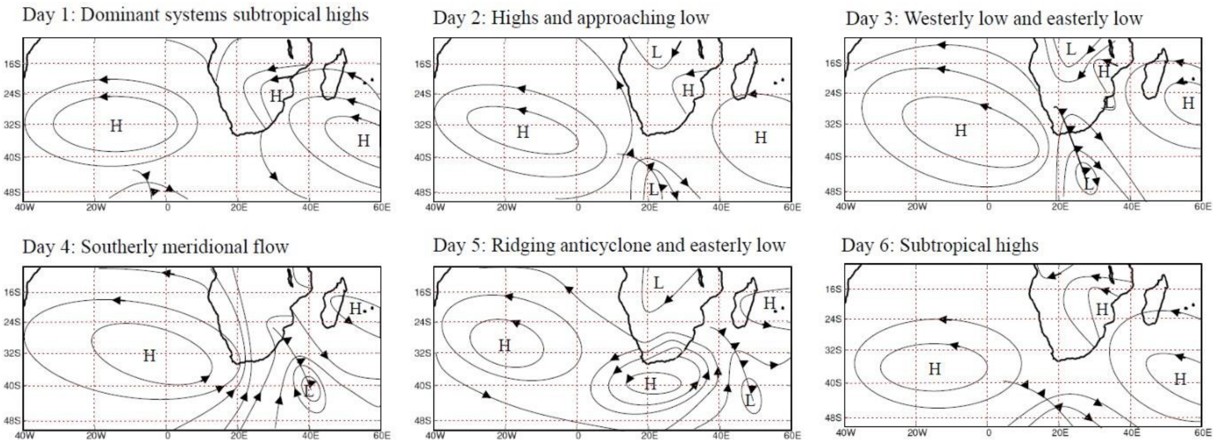

Figure 3.1: *A schematic representation of the ridging high from inception when the South Atlantic anticyclone extends eastward to cessation, and when the leading edge that has broken off from the parent anticyclone amalgamates with the Indian Ocean system. [Adapted from Tyson and Preston-Whyte (2000)].*

Reason et al. (2006) proposed that if it is stronger then there is more low level moisture, and the opposite is true when it is weaker. Another source of moisture for the summer rainfall region over South Africa is the Southwest Indian Ocean (SWIO; Cook et al., 2004; Dyson, 2015). Most of this moisture is facilitated by the flow that is brought about by the ridging South Atlantic anticyclone (here referred to simply as the ridging high). Recent studies (e.g. Barimalala et al., 2019) have also shown that the moisture transport that occurs from SWIO can be substantially modified by the variability of the cyclonic circulation in the Mozambique Channel. As such, there are outstanding questions associated with the moisture transport that is associated with the ridging high, which should be addressed by first understanding the dynamics of these systems, as it describes the flow, after which the moisture transport issues may then be addressed. The purpose of this chapter is to address some of the outstanding dynamical processes questions of the ridging highs and then consider how these systems transport moisture into South Africa from the SWIO and the predictability issues associated with them.

The ridging high is an important synoptic weather system in South African meteorology. As described in textbooks (e.g. Tyson and Preston-Whyte, 2000), the ridging process occurs in stages. These are summarised in Figure 3.1 above and describes in points below

- Early stages (on day 1): The flow and circulation is characterised by subtropical highs in the South Atlantic and Indian Oceans. These, as it is well known, are associated with the fact that there is climatologically descending air that is caused by the thermally direct Hadley cell and thethermally indirect Ferrel cell. There would also be an approaching cold front to the south of the South Atlantic high.
- Development stages (on days 2 and 3): The South Atlantic high begins to extend east, trailing the cold front as the latter drifts slightly east, so that its tail end sweeps the southern parts of South Africa, causing the flow into the country to be oriented Southwesterly (note that atmospheric flow

direction is defined in terms of where the wind comes from). This flow is an effect of the cyclonic circulation to the west of the cold front.

- Matured stages (on day 5): At this point, the eastward extension has gone beyond 25°E and this process continues until the leading edge breaks off from the parent South Atlantic Ocean anticyclone and drifts past the subcontinent. As the pinched component moves eastward, the flow into the country is now south-easterly and brings moisture from the SWIO.
- Final stages (on day 6): The pinched part of the high then continues to propagate eastward until it merges with the Indian Ocean system.

Several studies have considered ridging highs, but none have considered the dynamics of these systems to answer the following question

- What initiates the ridging process?
- Precisely how do ridging highs bring moisture into South Africa?
- Can the predictability of these systems be enhanced on the basis of improved dynamical understanding?

The rest of the chapter is organised as follows: In Section 3.2 we provide the data and methods that were used in this part of the project. This is followed by a dynamical analysis Section 3.4, which is divided into several subsections that discuss the variability of the ridging events, their links to lower stratospheric dynamics and large scale propagating Rossby waves to answer the first question as well as moisture transport processes to answer the second question. In Section 3.5 we present the predictability issues associated with these systems and provide the concluding remarks in Section 3.6.

3.2 Data and methods

3.2.1 Data

Several reanalysis products were used to identify ridging highs from 1979 to 2017 or 2018, depending on when the analyses were conducted during the duration of the project. We limit the study to a post-1979 period because, as it is well known, reanalyses data are not reliable prior to this cut-off year (Tennant, 2004). Note that all these products are available at a grid spacing of 2.5°× 2.5°, which translates into an average of 278 km × 278 km resolution in the southern African domain, which we define here to include the surrounding oceans. So this would be the area bounded by 40°W and 60°E as well as by the Equator and 50°S. Some of the products listed below are available at higher resolution than stipulated above, but since the horizontal extent of processes involved in ridging highs are of synoptic scale, i.e. $L \sim 10^6$m or slightly larger, 2.5°× 2.5° is considered adequate. All the data are available on 17 standard pressure levels at 6-hourly intervals. These are summarised below in point form:

- The National Centres for Environmental Prediction (NCEP) – U.S. Department of Energy (DoE) AMIP II (Kanamitsu et al., 2002), which is referred to simply as NCEP-2 is produced using a three dimensional variational analysis data assimilation scheme. It is a significant improvement from the first version of NCEP reanalysis (Kalnay et al., 1996).
- The European Centre for Medium-Range Weather Forecasts (ECMWF) – Interim (ERA-Interim, Dee et al., 2011) is produced by means of a four dimensional variational analysis scheme.
- The Japanese 55-year reanalysis product is also producing by a four dimensional variational data assimilation scheme (Kobayashi et al., 2015) and is considered to be a high quality product and compares well with the others.

3.2.2 Methods

(a) Ridging detection algorithm

To identify ridging anticyclones in the South African domain (defined above) a simple three step objective algorithm was developed. This process exploits MATLAB®'s capabilities for approximating the vector indices of the latitudes and longitudes through which a contour passes within the domain. The domain was chosen to be large enough for all the South Atlantic systems to be considered, including those that extend eastward, as the ridging process takes place, but small enough to exclude other anticyclones on the subtropical belt and closed temperate cyclones.

The steps in the algorithm are outlined as follows

1. For each six-hourly time step, minimum and maximum mean sea level pressure (MSLP) values are identified and contours of MSLP from each minimum value to the corresponding maximum value are then calculated at 1 hPa intervals. Only closed contours longer than 20 grid points are recorded as potentially belonging to an anticyclone. The 20 grid point restriction is aimed at excluding subsynoptic scale processes;

2. All concentric contours are grouped together starting with the largest one and ending with the smallest. Concentric contours are recorded as belonging to the same anticyclonic circulation (see Days 1 to 3 panels in Figure 3.1), and each one of the anticyclones is labelled accordingly;

3. The anticyclones are then categorised as ridging (see Days 4 and 5 panels in Figure 3.1), if at least the outer most contour extends from the South Atlantic Ocean across the 25° longitude line.This enables the calculation of the duration of each ridging anticyclonic event. Two centres of anticyclone activity have been identified in the South Atlantic Ocean (Jones and Simmonds, 1994), this step automatically disqualifies the centres that occur upstream, closer to South America, as they would be too far west to ridge into the Indian Ocean.

(b) Potential vorticity, Rossby wave breaking and wave activity diagnostics

Diagnosis of the vertical structure of potential vorticity (PV) requires its calculation on isobaric surfaces (Hoskins et al., 1985; Tamarin and Kaspi, 2016), using

$$p = -g(f\mathbf{k} + \nabla_p \times \mathbf{u}) \,.\, \nabla_p\theta \qquad (3.1)$$

where ∇_p is the horizontal gradient operator keeping the pressure constant (i.e. on isobaric surfaces), for which the derivatives are calculated using second order differencing on a sphere, f is the planetary vorticity and $\nabla_p \times \mathbf{u}$ is the relative vorticity. The vertical derivatives of potential temperature θ, $\partial_p\theta$, are calculated using a second order finite differencing method that takes unequal spacing of the standard pressure levels into consideration.

To find the link between ridging anticyclones and the lower stratosphere the notion of Rossby wave breaking (RWB) was considered. RWB is most clearly seen by examining potential vorticity (PV) contours on isentropic surfaces and is defined as the irreversible deformation and overturning of the contours such that $\partial_y P < 0$, where P is the PV (McIntyre and Palmer (1983). In this project, the PV values are obtained using Equation (3.1) and linearly interpolated to the 330 and 350 K isentropic surface as in Ndarana and Waugh (2011).

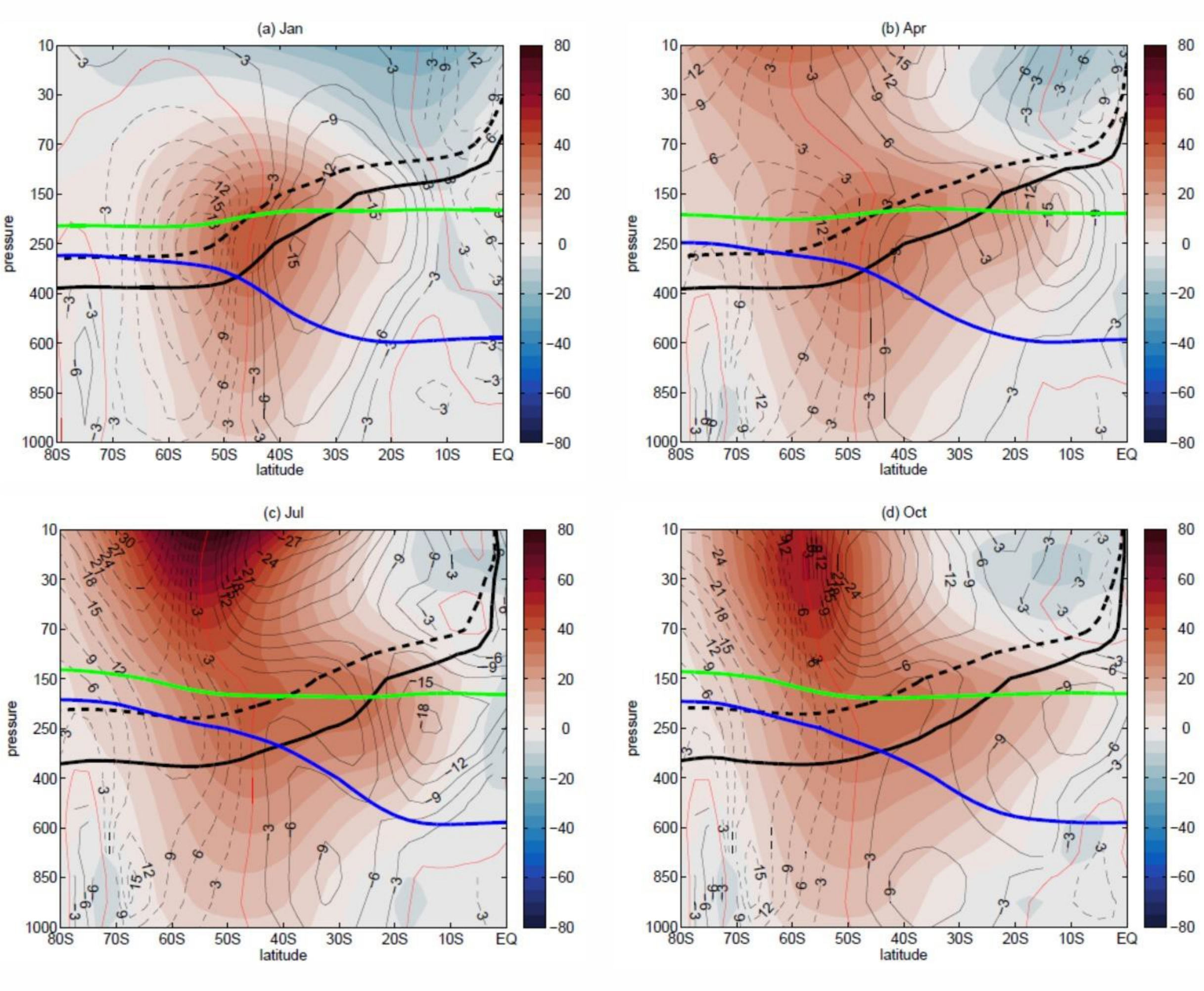

Figure 3.2*: Vertical profiles of zonal wind (shaded), anticyclonic (thin black contours) and cyclonic (thin dashed contours) barotropic shear. The dynamical tropopause is represented by PV = -2 PVU (thick black contour), the PV = -5 PVU (thick black dashed contour), the 350 K isentropic surface (thick green contour) and 330 K isentropic surface (thick blue contour) are shown for (a) January, (b)April, (c) July and (d) September. The fields are averaged in the South Atlantic Ocean from 20°W to 20°E. The thin red contour represents areas where barotropic shear is zero. The barotropic shear is plotted in intervals of $3 \times 10^{6}\, s^{-2}$.*

The actual level that might be important for the ridging high will first be established from a PV-θ point of view and then the vertical PV anomaly structure will be considered. The rationale for choosing the 330 and 350 K isentropic surfaces can be explained based on Figure 3.2. As shown in this figure, the intersection of the PV = -2PVU contour with the 350 K (green contour) and the 330 K (blue contour) isentropic surface occurs in the subtropics and midlatitudes, thus defining the dynamical tropopause at these regions, and these vary with the season but these seasonal changes are not significant. Figure 3.2 also shows that for the most part, the subtropical and midlatitude dynamical tropopause occurs on the anticyclonic barotropic shear of the jet streams (i.e. north of the thin red contour), thus the wave breaking on these tropopause levels would be oriented in the manner shown in Figure 3.3.

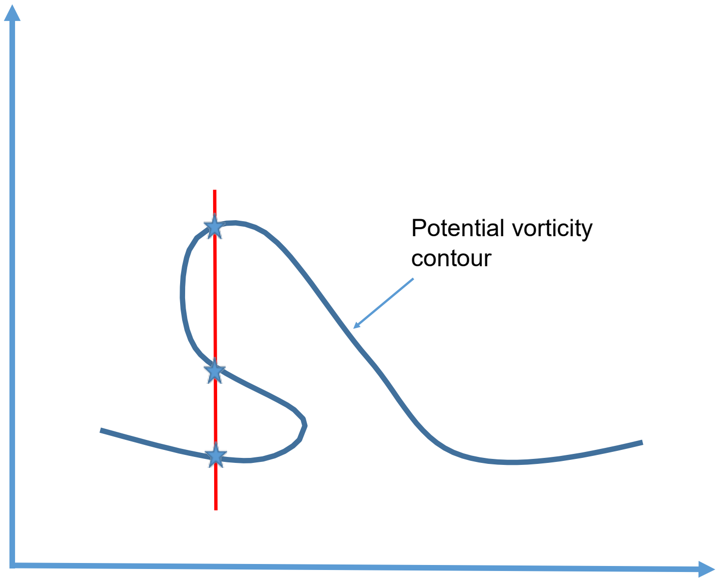

Figure 3.3: *Schematic representation of a potential vorticity contour demonstrating the methodology used in the study for identifying RWB events. This schematic shows an example of anticyclonic RWB that is found on the anticyclonic barotropic shear side of the jet stream (Thorncroft et al., 1993).*

To identify the wave breaking events in the PV data, we search for regions of overturning along each contour, following Ndarana and Waugh (2011) as demonstrated in the schematic representation in Figure 3.3. A region of PV overturning is said to have been found if a meridional line (red line) intersects the contour at least three times (represented by the blue stars). This takes place at consecutive longitudes until the test fails. All the grid points where it passes, are then collected to define the PV overturning region and the RWB point is considered to be the middlemost grid point of the fold.

To categorise RWB in the Southern Hemisphere we follow Gabriel and Peters (2008) and Ndarana and Waugh (2011) and used the meridional component of a phase independent wave activity flux (Takaya and Nakamura, 2001), given by

$$F_y = \cos\phi(2|\overline{\mathbf{V}}|)^{-1}\left[\overline{U}\left(-uv - \phi f^{-1}a^{-1}\partial_\phi v\right) + \overline{V}\left(u^2 + \phi f^{-1}a^{-1}\partial_\phi u\right)\right] \tag{3.2}$$

where all the symbols represent geostrophic variables. The upper case symbols with over bars represent basic state fields, whilst the lower case ones are the perturbations. In addition to making the quasi-geostrophic assumption (which might limit its applicability over South Africa), this diagnostic assumes small amplitude wave propagation, whereas RWB is a nonlinear process. Nonetheless, this diagnostics can still provide useful information about the nature of RWB, in particular its morphology.

The basic state flow is defined here as the seasonal average and perturbations are deviations from it. F_y is calculated for each six-hourly time step, and then a 48-hour window running mean, a nine grid point smoother and a pressure weighted vertical average (i.e. $\langle A\rangle = (p_2 - p_1)^{-1}\int_{p_1}^{p_2}(A)dp$ – Hotlon, 2004) from 400 to 100 hPa are calculated for reasons detailed in Gabriel and Peters (2008) and Ndarana and Waugh (2011).

(c) Composite analysis

To establish relationships between fields, composite analysis is used. A different, slightly more complicated compositing strategy will be followed in Chapter 3, as was done in previous studies (e.g. Ndarana and Waugh, 2010; 2011) to extract climatological behaviour of dynamical processes of weather systems. In this chapter, the composite analysis is simplified by the fact that ridging highs occur around South Africa and within a specific band of latitudes and therefore there are few geographical variations.

The basis for compositing then is simply the duration of the ridging events, and no other assumption is made.

3.3 Dynamical analysis

3.3.1 Intra-annual variations of ridging highs

The development of objective methods for identifying ridging highs presents us with the first opportunity since Tyson and Preston-Whyte (2000) to update the intra-annual variations of these systems. Ridging high-pressure systems exhibit a clear seasonal cycle, with 5 to 10% more than the annual average of 260 ERA-Interim and 268 JRA ridging events per annum occurring during the summer months on the average (Figure 3.4 (a)). As few as 15%, less than the annual average develop during the colder months of the year. Figure 3.4 (a) also shows that there is significant month-to-month variability in the frequency of ridging highs. This is particularly true from the end of summer to the beginning of autumn when the number of events increase by about 10% and then generally decrease to the middle of winter. The number of events increases substantially from July to August by approximately 20%. The number of events then decreases by 10% and then increases steadily until the summer. These variations are in good agreement between ERA-Interim and JRA-55 (with a correlation coefficient of 0.93 between datasets), except perhaps in May and June when more events were identified in the former dataset and in November when the opposite is true. The results obtained here with significantly more events, confirm previous climatological studies of ridging highs (Vowinckel, 1956) which used 73 events, whereas in this study we identified 3119 and 3216 ridging high events in ERA-Interim and JRA-55 reanalyses, respectively.

Ridging high-pressure systems last for several days, with shorter lived events generally occurring more frequently than those with higher longevity. To produce the average latitudinal positions of the events, the average latitude was calculated for each event over its duration and these were then plotted as a function of the month (Figure 3.4 (b)). Ridging high-pressure systems occur at the southernmost latitude during the late summer and early autumn and migrate north to occur at the northernmost latitude in July. They appear to migrate south during the spring and then slightly back north toward the summer months. This W-like structure in the annual profile of their preferred latitudinal positions of occurrence is consistent with the behaviour of the SAOH in general (Tyson and Preston-Whyte, 2000; Sun et al., 2017). Again there is an excellent agreement between ERA-Interim and JRA-55 ridging events, thus demonstrating the robustness of this result.

Wave breaking on the dynamical tropopause and in the lower stratosphere on the 350 K isentropic surface also shows a clear seasonal cycle, with about 25% more events than the annual average identified in March in both ERA-Interim and JRA-55 products. The events decrease steadily by as muchas about 45% to reach minimum frequencies right through the winter months, and increase again towards the summer. This seasonal cycle in wave breaking events is consistent with changes in anticyclonic barotropic shear in the lower stratosphere, which decreases significantly from summer to winter (Figure 3.2). This is clearly caused by the development of the subtropical jet as the polar vortexis established and the former reaches its highest intensity in midwinter (Waugh and Polvani, 2010). There is broad agreement between the seasonal profiles of ridging highs and wave breaking events. However, month-to-month variations are not present in the latter. So, whilst wave breaking that occursin the subtropical lower stratosphere may explain the seasonal cycle of ridging events, it might not be sufficient for explaining the large late winter and spring monthly variability. In addition, the seasonal migration of wave breaking events in latitude is consistent with that of ridging highs, except during themiddle of spring to December (compare Figures 3.4 (b) and (d)). Therefore, wave breaking may explain the position of ridging. An attempt to show this will require that a relationship between ridging highs and RWB events be established.

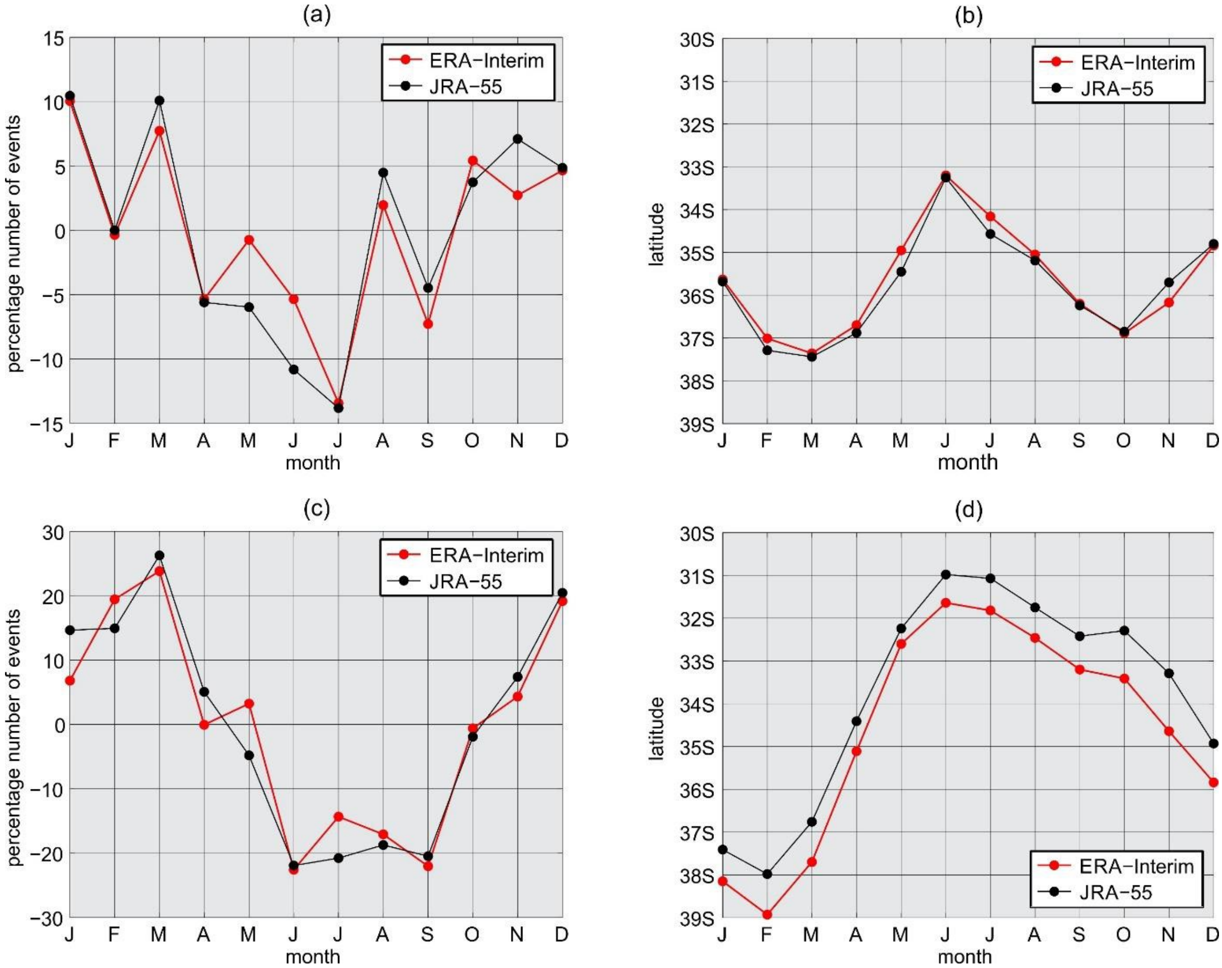

Figure 3.4: *Percentage of (a) ridging highs relative to the annual mean number events calculated as* $(n - N)\times 100\%$*, where n and N are the monthly and annual average number of events, plotted as a function of months. (b) Latitude position of the ridging high point plotted as a function of months. (c) and (d) are the same as (a) and (b) respectively but for wave breaking events.*

About 65% of all ridging high-pressure systems that were identified in ERA-Interim and JRA-55 reanalyses are linked to wave breaking events that occur in the lower stratosphere and on the dynamical tropopause along the 350 K isentropic surface. The inception of all wave breaking events that have a ridging event associated with them precede that of the latter ($\Delta\tau < 0$ in Figure 3.5 (a)). In addition to this, wave breaking occurs upstream from the leading edge of ridging highs ($\Delta\lambda < 0$ in Figure 3.5 (b)). Also not all wave breaking events are associated with ridging highs. Once all those breaking events that had this association was identified, it was found that about 75% of the remaining ones do not have any ridging associated with them.

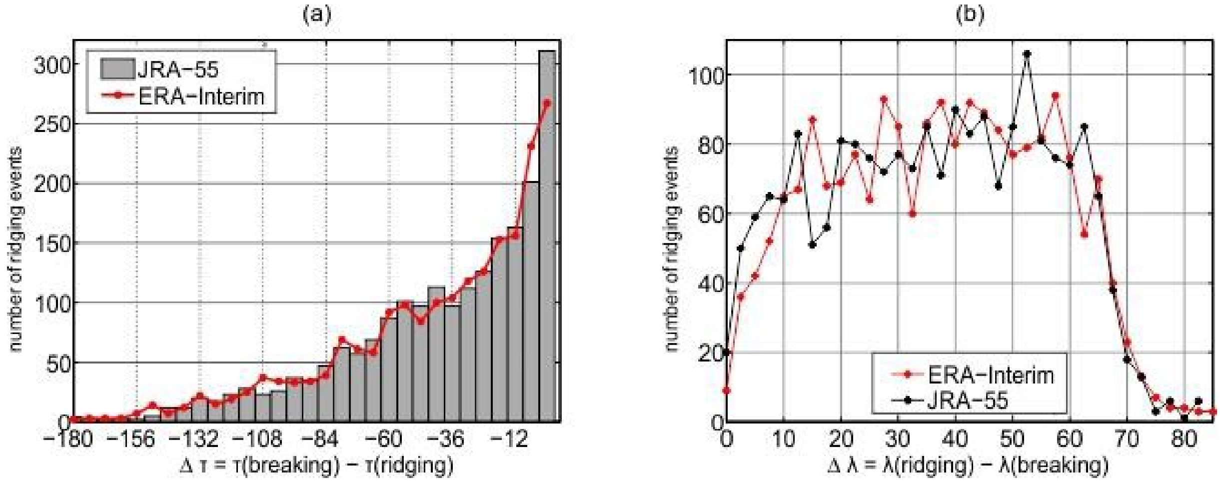

Figure 3.5: *(a) The frequency of ridging events that have lower stratospheric wave breaking associated with them, plotted as a function of $\Delta\tau = \tau(ridging) - \tau(breaking)$, which is the difference in hours between the hour of inception of the processes. (b) Same as (a) but plotted as a function of the differencebetween the longitude of the leading edge of the ridging highs and the wave breaking events (i.e. $\Delta\lambda = \lambda(ridging) - \lambda(breaking)$.*

The three issues discussed above, together with the fact that wave breaking occurs aloft, whilst ridging is a low level process, suggest that if one of the processes influences the other, it would be wave breaking playing the role of causation. The remaining 35% of ridging events are linked to PV intrusions, which are special cases of wave breaking and defined as tongues of tropospheric (stratospheric) air into the stratosphere (troposphere) without any significant PV overturning (Waugh and Polvani, 2000). A similar relationship was found between RWB and cut-off lows (Ndarana and Waugh, 2010). This relationship is confirmed by visual inspection of individual events and their composites, which show perturbed PV contours and PV anomalies on the 350 K isentropic surface.

Linking ridging high-pressure systems to some wave breaking events in the lower stratosphere provides a possible explanation of the source of the intra-annual variability of the former. When the frequency of the ridging events that are associated with wave breaking are plotted as a function of month (Figure 3.6 (a)) as in Figure 3.4 (a), it becomes apparent the summer maximum and winter minimum in their frequency is similar to that of wave breaking in Figure 3.4 (c). The correlation coefficient between the intra-annual variability of wave breaking (Figure 3.4 (c)) and ridging that is associated with them (Figure 3.6 (a)) is 0.95 (0.93) for ERA-Interim (JRA-55) data. The similarity and high correlations between the variability of wave breaking and ridging events, as well as the fact former plausibly induces the latter suggests that the summer maximum and winter minimum of ridging events seen in Figure 3.4 (a) is caused by that of wave breaking. By extension, the reduction in barotropic shear in the lower stratosphere and upper troposphere, which in turn is caused by the development of the subtropical jet and the weakening of the eddy driven jet (Bals-Elsholz, 2001), play a role in the summer maximum and winter minimum in the frequency of ridging high-pressure systems.

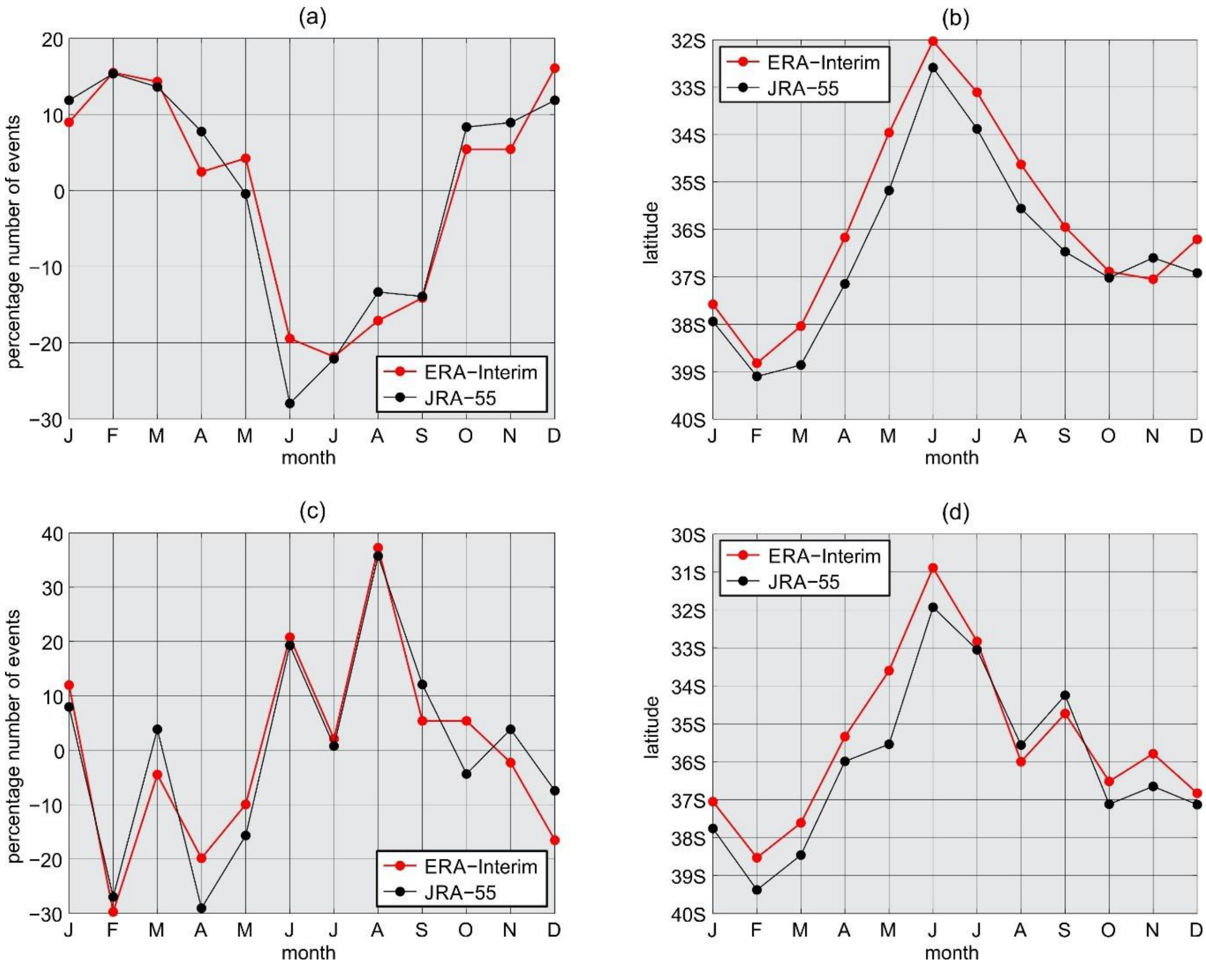

Figure 3.6: *Percentage of (a) ridging highs that are associated with wave breaking relative to the annual mean number events calculated as* $(n - N) \times 100\%$*, where n and N are the monthly and annual average number of such events, plotted as a function of months. (b) Latitude position of the ridging highs in (a) plotted as a function of months. (c) and (d) are the same as (a) and (b) respectively but for wave breaking events that are not associated with wave breaking.*

The large month-to-month variations seen in Figure 3.4 (a) and not present in Figure 3.6 (a), thus suggests that wave breaking does not play a role in these variations, as Figure 3.4 (c) also confirms. These large month-to-month variations might be associated with PV intrusions. The frequency of ridging events (Figure 3.6 (c)) that are associated with intrusions attains a maximum in August and a minimum in February and another in March, which is in contrast to what we see in Figure 3.6 (a).

Figures 3.6 (c) and (d), when compared to Figure 3.4 (d) and combined with the seasonal position of the dynamical tropopause in Figure 3.2, suggest that meridional migration of ridging high events is correlated with the seasonal cycle in the meridional shift of wave breaking. This is particularly clear in the case of wave breaking events that have wave breaking associations (Figure 3.6 (c)). For the intrusion cases, there is pronounced variability during the spring through to the beginning of summer, but the general poleward migration is still observed.

3.3.2 Dynamical aspects of the links between RWB and ridging highs

The discussion presented in Subsection 3.3.1 suggests a dynamical link between RWB and ridging highs predictability at the MRF time scale. In this subsection we explore the dynamical aspects of this link and employ the power of composite analysis in doing so. As noted in subsection 3.2.2 (c), the only assumption made as a basis for the compositing strategy is the duration of the ridging events, and so the associated fields are established in an automatic fashion. As shown in Figure 3.7, the number of ridging events decreases exponentially as a function of duration, with the shorter lived events occurring more frequently than the ones with loner durations. The composite horizontal evolution of ridging highs, presented in Figure 3.8, shows that there is co-evolution that occurs at the surface and in the upper troposphere and lower stratosphere. The RWB signature becomes apparent as early as $\tau = 0$ hour (Figure 3.8 (b)), as indicated by the red contour turning back on itself such that $\partial_y P < 0$, at which point the ridging process begins to take place. This happens in the region between the Greenwich meridian and 20°E the breaking matures at about τ = 24 hours and 36 hours (Figures 3.8 (d) and (e)). This occurs together with the maturation of the ridging process and is indicated by the leading edge of the Atlantic Ocean high extending eastward to cross the 25°E latitude line. It curls backs as it does so and forms a bean-like shape. As will be seen later in this chapter, at this point moisture is transported into the southern African mainland from SWIO. The bean shape occurs when the RWB is located just south of the country. The RWB is at its most mature stage when the leading edge has broken off from the parent anticyclone and the former dissipates as the broken off part merges with the Indian Ocean system.

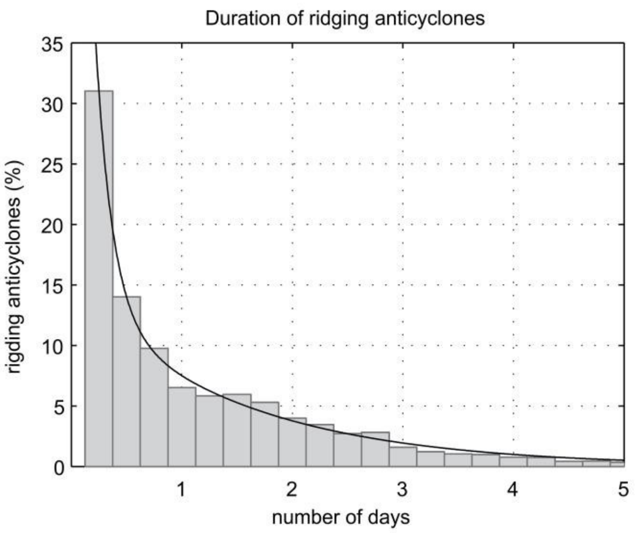

Figure 3.7: *Histogram showing the frequency of occurrence of South Atlantic ridging anticyclones (y-axis) as a function of duration n days. The curve is a fitted exponential function.*

We propose that the RWB process identified in Figure 3.8 is part of a wave pocket that develops from South America. To support this proposal, we first present composites of RWB events that were produced by bringing these invents into phase, so that the RWB points, as identified in Subsection 3.2.2 (b) and Figure 3.3, coincide, together with composite perturbation meridional velocity anomalies at 200 hPa and 850 hPa geopotential height anomalies (see Figure 3.9). The structure of $v^0 > 0$ m s^{-1} in Figure 3.9 (e) in the region of PV overturning presents an alternate view of wave breaking as viewed from the point of view of meridional perturbation fields. Therefore, when the meridional zonal flow elongates in this manner, there exits wave breaking there. This v^0 RWB signal is can also be observed in Figure 3.10 (h), which is the point at which the South Atlantic anticyclone extends east, as indicated by the thick black contours. The main point of Figure 3.10 is that the RWB process that is associated with ridging highs is part of a larger scale process and that is a propagating Rossby wave train or packet that develops near the Drake passage between South America and Antarctica. This wave train propagates in a north-easterly direction and appears to be reflected over South Africa, as the waves break. O'Brien and Reeder (2019) observed a similar process, even though their analysis was based on the interaction of the propagating Rossby waves and the jet stream. This provides a broader context within which ridging highs occur.

A visual inspection of the RWB in Figure 3.8 is anticyclonic. This is expected, of course, because it occurs on the anticyclonic side of the jet, where the zonal flow decrease towards the north from the jet core (see also Figure 3.2 as indicated by the thin black contours, relative to the shading representing the zonal isotachs in which the jet stream is evident). Thorncroft et al. (1995) suggested that the shearing strain caused by the increase in the speed of the zonal flow towards the jet core and decrease of the speed equatorward leads to the anticyclonic twisting and thinning of the PV contours. Whilst the anticyclonic sense of the wave breaking that is associated with ridging highs can be observed, it needs to be ascertained by means of wave activity (see Equation 3.2). Elser and Haynes (1999) showed that anticyclonic wave breaking is associated with an equatorward wave activity flux, and Gabriel and Peters

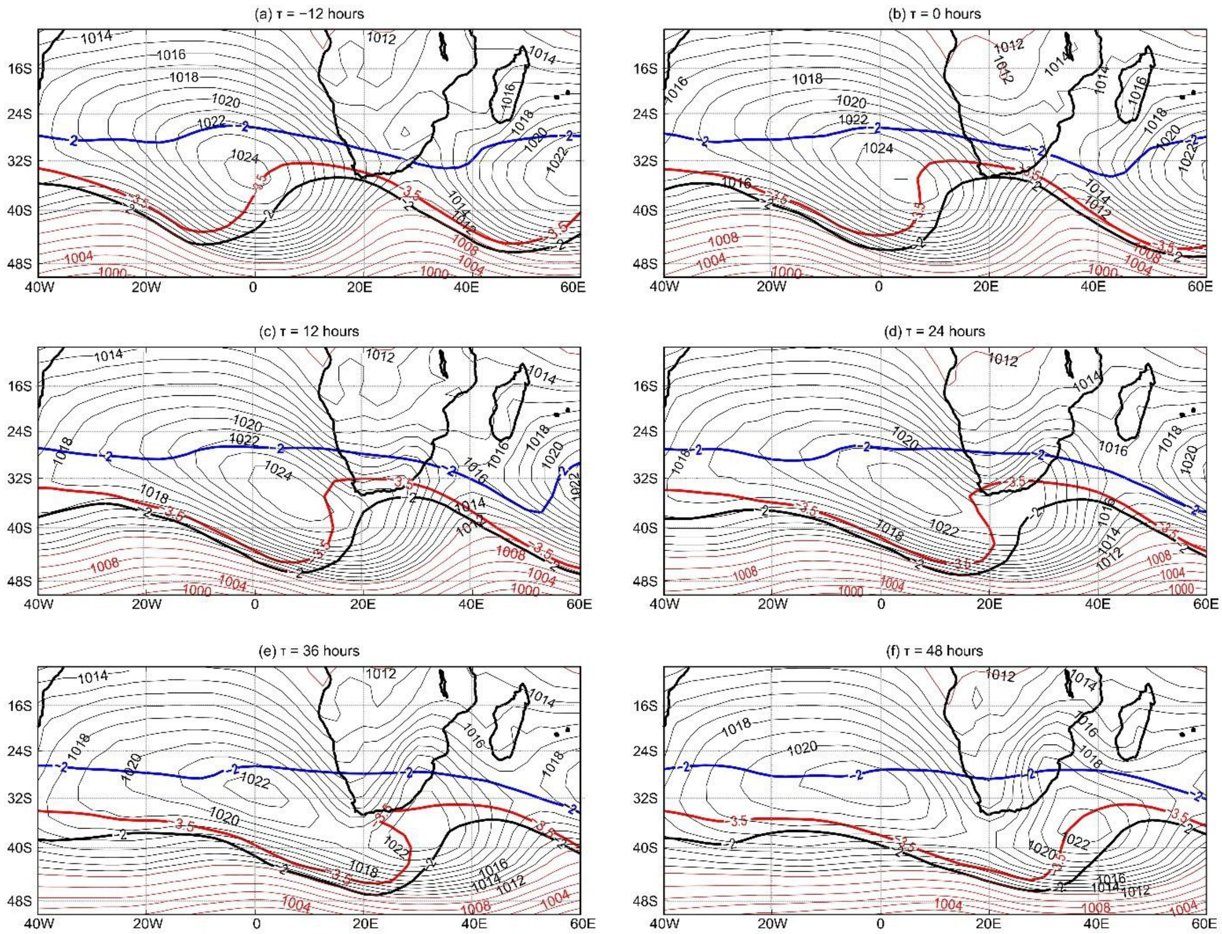

Figure 3.8*: Mean sea level pressure (thin black contours for values ≥ 1012 hPa and thin red contours for values ¡ 1012 hPa), PV = -2 PVU (thick blue contour), PV = - 3.5 PVU (thick red contour) on the 350 K isentropic surface and the thick black contour represents the PV = -2 PVU contour on the 330 K isentropic surface for (a) τ = - 12 hours and (b) τ = 0, (c) τ = 12 hours, (d) τ = 24 hours, (e) τ =36 hours (f) τ = 48 hours. MSLP contour interval is 1 hPa.*

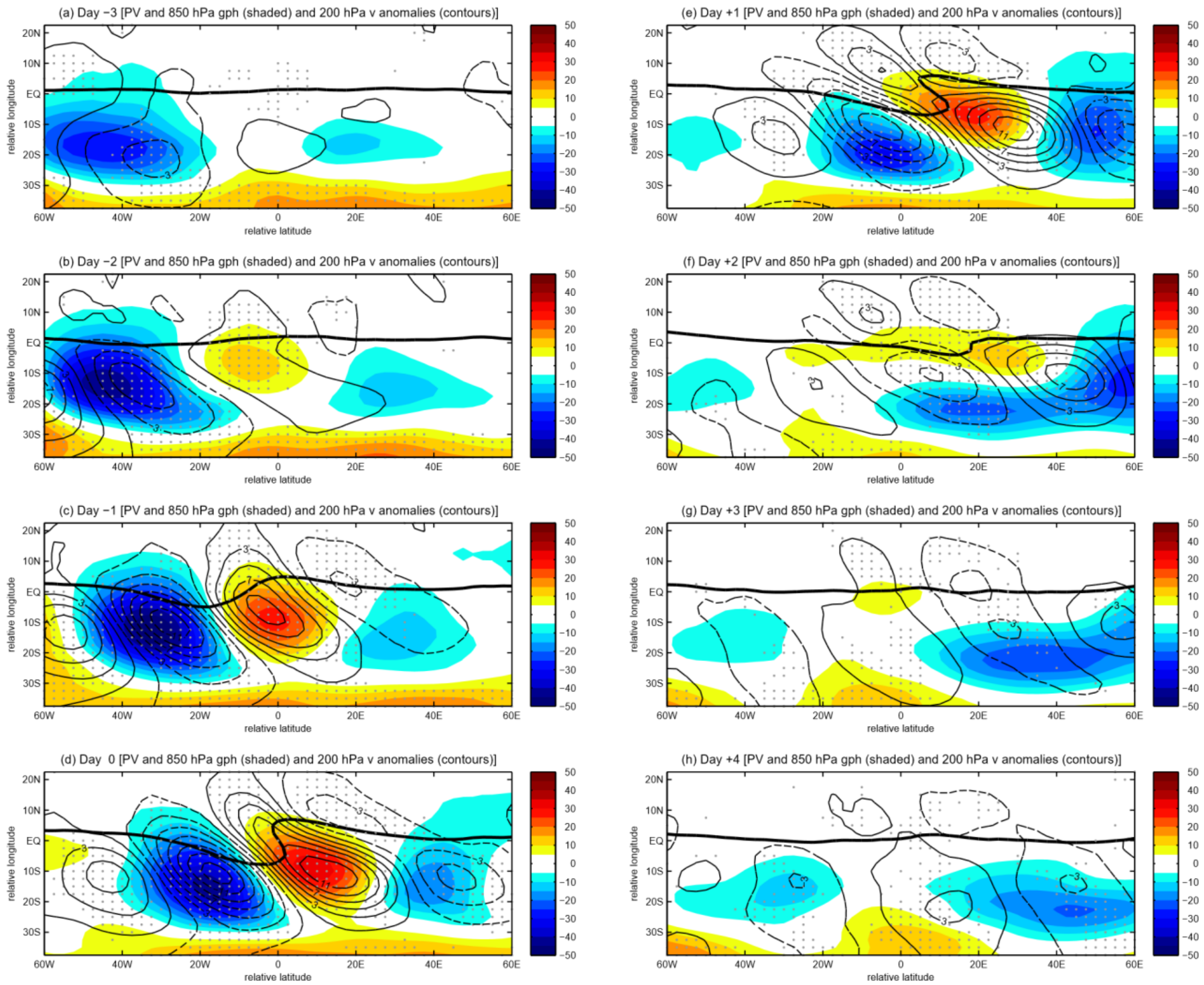

Figure 3.9*: Time-lagged, RWB event-based composites of the PV = -2 PVU contour at the 350 K isentropic surface and 200 hPa geopotential height (think black contours). The solid and dashed contours represent positive and negative values, respectively. The shading represents the 850 hPa geopotential height anomalies.*

(2008) and Ndarana and Waugh (2011) employed this idea to objectively categorise wave breaking in the Northern and Southern Hemispheres, respectively. The PV overturning region is clearly associated with $F_y > 0$, thus confirming that the wave breaking is anticyclonic. This is shown in Figure 3.11 (a).

The co-evolution of lower stratospheric wave breaking and ridging anticyclones discussed above suggests that the two processes are tightly coupled. We now explore this issue further using vertical profiles of isobaric PV and geopotential height anomalies. To determine the anomalies, the zonal average in the domain of interest is calculated and subtracted from the original PV and geopotential fields to obtain them. Their vertical profiles are constructed by taking the anomalies at 35°S (where the wave breaking and ridging occurs) at each level and longitude; to produce longitude vs. pressure plots. We opted not to take the average over a range of latitudes because this tends to cloud the point to be raised here as we desired to understand what dynamically transpires when the climatological bean-like shape forms. These vertical profiles are shown in panels of Figure 3.12. The two sets of figures should be interpreted together, observing that corresponding points in the evolution are on corresponding panels.

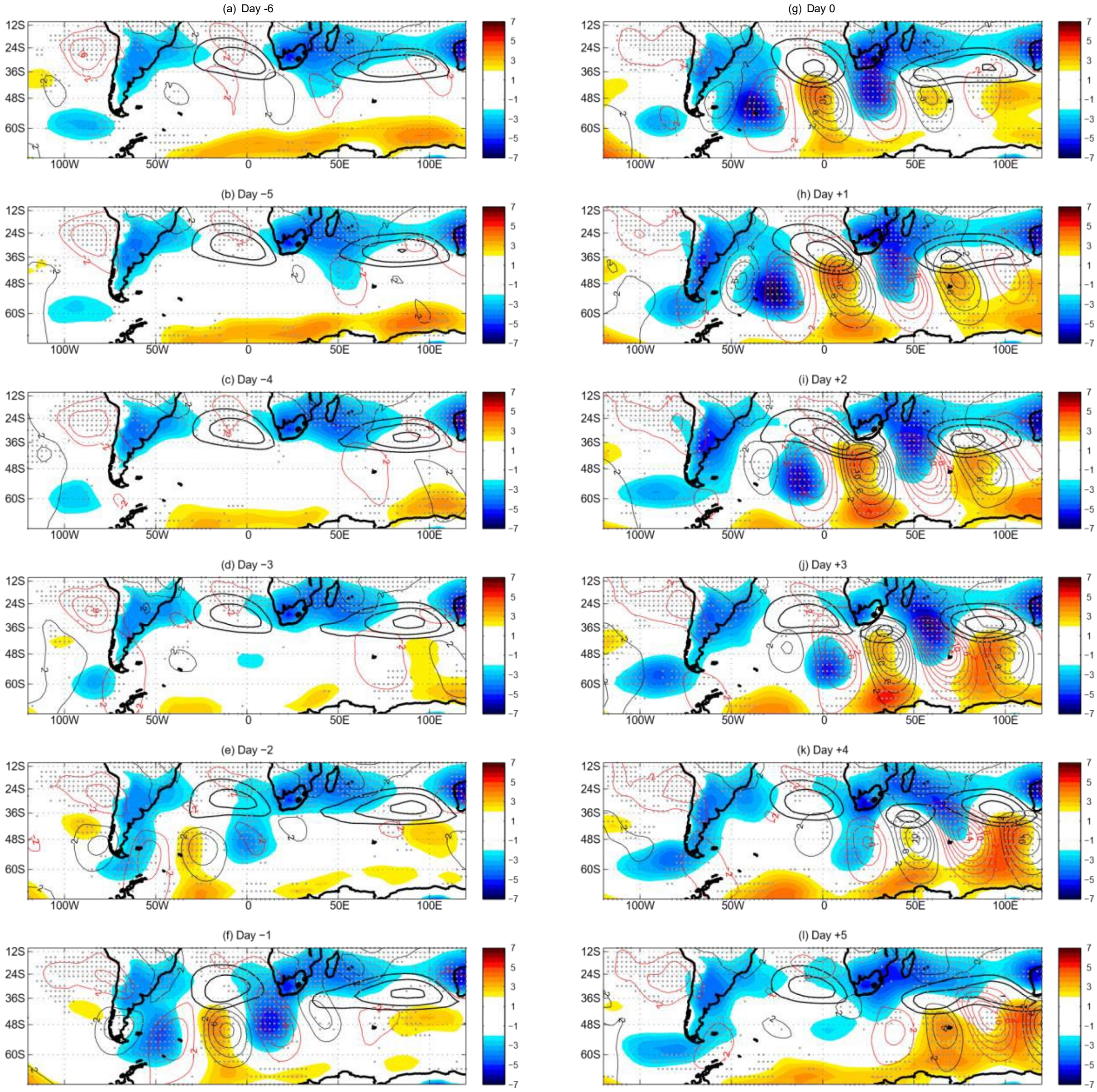

Figure 3.10*: Time-lagged, RWB event-based composites of the PV = -2 PVU contour at the 350 K isentropic surface and 200 hPa geopotential height (think black contours). The solid and dashed contours represent positive and negative values, respectively. The shading represents the 850 hPa geopotential height anomalies.*

Before discussing the actual vertical coupling that takes place when Atlantic Ocean anticyclones ridge, we consider the distribution of the PV anomalies in the lower stratosphere and briefly contemplate how they form. Figure 3.11 (b) shows a snapshot of lower stratospheric wave breaking and the associated 350 K isentropic PV anomalies at τ = 24 hours, which corresponds to Figure 3.8 (d). Clearly, the southern and northern lobes of the RWB are associated with positive and negative anomalies, respectively. This PV anomaly structure is brought about by southward isentropic transport of low PV air from the subtropics and northward transport of high PV air from the midlatitudes. This two-way transport is facilitated by RWB.

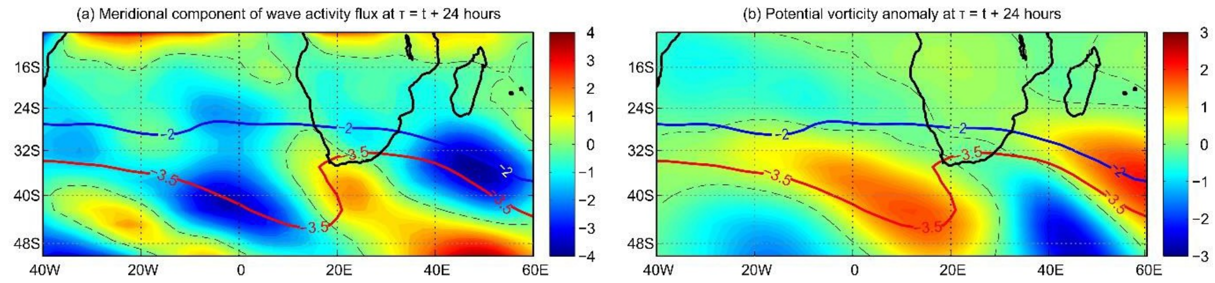

Figure 3.11: *(a) Composites of PV as in Figure 3.8 (d) with F_y represented by the shading at τ = +24 hours. In (b) the shading represents the PV anomalies at the 350 K isentropic surface.*

The PV anomalies extend from above the 350K isentropic surface in the lower stratosphere to the midlatitude dynamical tropopause, but decrease in strength as they approach this level (Figure 3.12). On an annual average, the tropopause pressure in the midlatitudes of the Southern Hemisphere is about 250 hPa (Hoinka, 1998), as confirmed also by the intersection between the PV = -2 PVU and 330 K isentrope (see Figure 3.2). This means that the strongest PV anomalies are located above the tropopause. It may then be concluded that the vertical structure of the PV anomalies suggests that the wave breaking, which is associated with ridging anticyclones, as discussed above has a three dimensional structure but it is weakest (or vanishes) just above the midlatitude tropopause. The diminishing strength of the PV anomalies near the 250 hPa level is consistent with the climatological structure of the midlatitude dynamical tropopause, which is perturbed but does not show as much overturning on average as PV in the lower stratosphere. This confirms the aforementioned suggestion that the RWB which is associated with (or that it is important for) ridging anticyclones is indeed predominantly a lower stratospheric phenomenon.

The evolution of the vertical profiles of PV and geopotential height anomalies (Figure 3.12) are consistent with the evolution of RWB and ridging anticyclones. Before the ridging takes place, the Atlantic anticyclone pressure system appears to be coupled with the upper air positive PV anomaly. This is indicated by the colocation of the vertical PV anomaly structure and that of the geopotential height anomalies. This PV anomaly extends down to the surface to the region of strongest positive geopotential height anomaly (i.e. just west of the centre of Atlantic to about the eastern edge of the anticyclone – observe the location of the thick white contour between 20°W and the Greenwich Meridian and at about 20°E relative to the thin black contours in Figure 3.12(a). East of this positive PV anomaly, there exists a negative anomaly (Figure 3.12 (a)). The latter also extends down to the surface of the region between the Atlantic and Indian Oceans systems. A westerly wave low-cold front system is found in this region, as shown by the negative geopotential height anomalies found there. In both structures, the westward tilt with height is clear, which is characteristic of baroclinic systems (Charney, 1947), and signals the extraction of eddy available potential energy from the mean flow (Holton, 2004). Note also that the lower stratospheric PV anomaly field appears before the breaking takes place. This pre-existing PV anomaly arrangement would most likely be associated with undulations in the PV contours and, therefore, linear Rossby wave propagation.

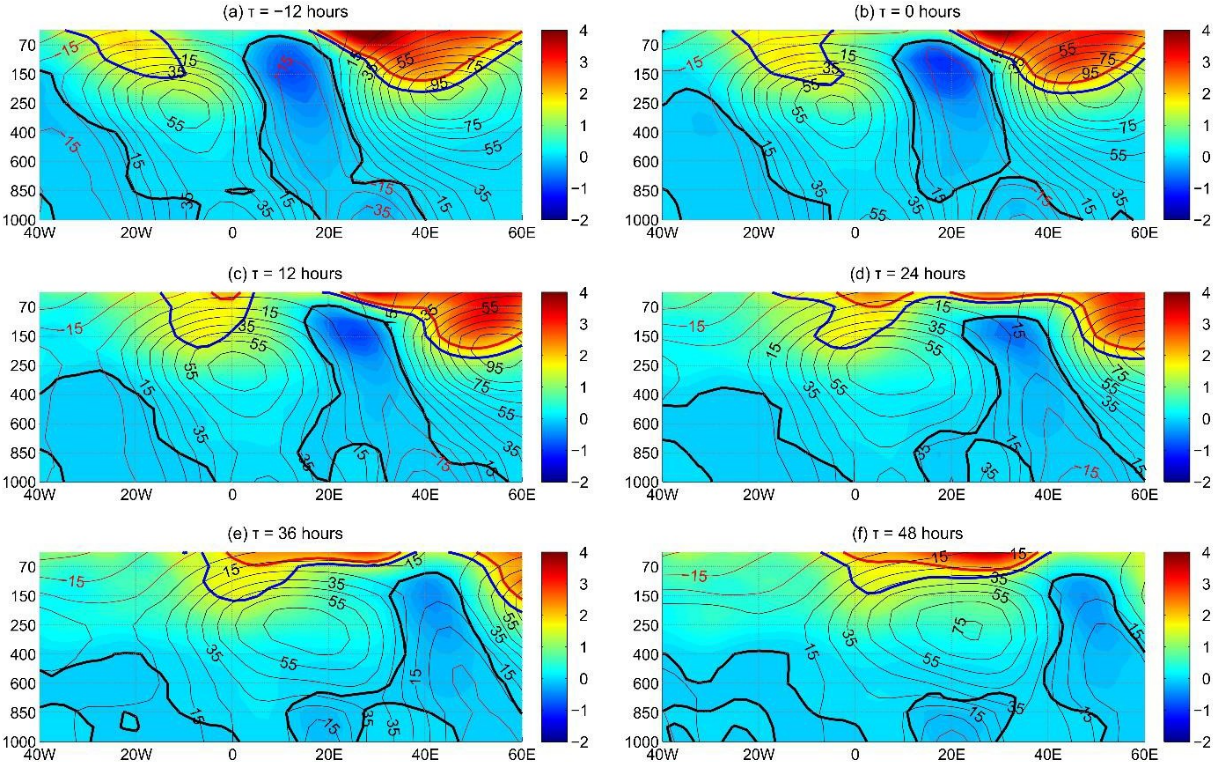

Figure 3.12: *Vertical profiles of potential vorticity and geopotential height anomalies for τ = t - 12 hours, with the thick red, blue and black contours representing the -2, -1.5 and 0 PVU PV anomaly contour levels. The thin black and red contours represent the positive and negative anomalies, respectively, plotted at intervals of 10 gpm. The fields are shown for (a) τ = - 12 hours and (b) τ = + 0, (c) τ = 12 hours, (d) τ = 24 hours, (e)τ = 6 hours (f) τ = 48 hours.*

As the breaking events propagate eastward, the strong lower stratospheric PV anomalies are also advected eastward. The pre-existing lower stratospheric PV anomaly is elevated slightly (observe the vertical displacement of the 1.5 PVU anomaly contour in Figure 3.12) and strengthened with time (as the appearance of the thick red contour and the wave breaking wave propagates eastward), whilst its negative counterpart is lowered. This stands to reason because, whilst the 350 K isentropic surface appears to be quasi-horizontal, the isentropic surfaces below that level have a negative gradient with respect to decreasing pressure. The wave breaking occurring at these levels will tend to transport the low (high) PV air up (down) the gradient, taking the sign convention of PV in the Southern Hemisphere into consideration, in addition to advecting the alternating lower stratospheric PV anomaly eastward.

It is clear from Figure 3.12 that lower stratospheric air that is advected southward continues to be important during the ridging process until the ridging anticyclone amalgamates with the Indian Ocean system. At that point, the lower stratosphere and surface are decoupled. The initiation of the ridging process is evident from Figure 3.12 (b) at $\tau = 0$ hours to Figure 3.12 (c) at $\tau = 12$ hours near the surface eastward of 20°E, as shown by the movement of the geopotential height anomalies. This movement of the geopotential anomaly is preceded by a low level positive PV anomaly forming there, which in turn is informed by an eastward propagation of the wave breaking. This suggests that the lower stratospheric wave breaking could be responsible for moving the whole positive PV structure so that the low level part of it can induce anticyclonic flow, where there wasn't any before.

As the system evolves, the interesting observation to make here is that the negative PV anomaly found upstream is important for ridging and it appears to be playing a role in inducing the cyclonic flow (trough) over the interior of the country, as the anticyclone takes the bean shape. As the ridging begins, the negative anomaly extends a tongue in a downward and westward direction (Figure 3.12 (c) at $\tau = 12$ hours). The tip of this tongue extends to the surface (Figure 3.12 (d) at $\tau = 24$ hours) and in some cases forms an isolated blob in the manner shown in Figure 3.12 (f) at $\tau = 48$ hours and in others it remains attached to the main vertical negative PV anomaly structure.

The high PV air starts reaching the surface as the ridging takes place (compare Figures 3.8 (d) and 3.12 (d) at $\tau = 12$ hours) and at $\tau = 48$ hours it has landed and covering a range of longitudes centred at around 20°E (Figure 3.12 (d) at $\tau = 24$ hours as the bean shape of the ridging anticyclone is at its advanced stage of formation, Figure 3.8 (d) just before it breaks off). The system that has broken off has a positive anomaly associated with it and continues to be coupled with the eastward propagating positive stratospheric anomaly, as the Rossby waves continue breaking and dissipating after $\tau = 48$ hours. This behaviour is again climatological and it is observed for all the composites, except for the short lived events.

To complete this three dimensional structure of the relationship between lower stratospheric dynamical processes and ridging highs we present the latitude/longitude low level anomalies. These are shown in Figure 3.13. The dynamics and possible role of the surface negative PV anomaly that forms, as discussed above, the horizontal PV anomaly field at 1000 hPa (shaded) – with MSLP (thick dashed bluecontours) and the thin black dashed contours representing the PV anomalies at the 350 K isentropic surface, are examined. There are three centres of negative PV anomalies that are observed at the 1000 hPa. The PV anomaly of interest at this point is climatologically located on the west coast of the subcontinent (i.e. the Namibian west coast). As the ridging occurs (represented here only by 1018, 1020and 1022 hPa contours (thick dashed contours in blue)), this anomaly extends southward following thestructure of the coast. The leading edge of this extension arrives in the Cape Town area as the bean shape of the anticyclone forms. Note that regions with negative anomalies stronger than -0.1 PVU are enclosed by the thin black contour. The region of the bean shape that curves southward is a trough andit is characterised by cyclonic flow (see also examples in Crimp and Mason, 1999, Blamey and Reason, 2009).

The source of the pre-existing Namibian west coast anomaly is unknown at this time, and requires further investigation, but we hypothesise that it is causing the large $\nabla_p \theta$ and the climatological trough that is known to exist in that region. Note also that the question of how it extends southward (Figures 3.13 (d) to (f)) cannot be answered without the benefit of the vertical profiles of the previous subsection. On this basis, we hypothesise that this extension is caused by the high level negative PV anomaly that is lowered by isentropic transport of high PV air facilitated RWB in the lower stratosphere, as it propagates eastward. Furthermore, when the low level negative PV anomaly reaches the Cape Town area, it induces the cyclonic flow that characterises the bean shape of the ridging system.

3.3.3 The flow and moisture fluxes associated with ridging highs

As noted in the Introduction (Section 3.1), ridging highs are not, on their own, rainfall producing systems; they have to be accompanied by synoptic weather systems aloft that provide the lifting mechanism. If there are no such weather systems and the moist air is transported into the KwaZulu-Natal region, then orographic uplift can then provide the required lifting for rainfall to occur. It follows then that the primary role of ridging highs in the dynamics of rainfall production in South Africa is to transport moisture. Because of the objective methodology presented here, this is the first opportunity to diagnose the flow associated with the ridging process and the moisture transport that this flow induces.

Studies that have analysed moisture transport have decomposed it into its basic state and perturbation components (e.g. Chen, 1985) and some use the velocity potential (D'Abreton and Tyson, 1995). Whilst these frameworks are useful and contribute immensely to our understanding of moisture transport dynamics, they are also quite abstract and are therefore very difficult to interpret. For that reason, they are of little practical value and so they would have limited applications in weather forecasting at the South African Weather Service. We acknowledge in this project that merely diagnosing the moisture transport using the velocity field as it stands or provided in reanalysis or forecast model data might not be enough to reveal the underlying dynamical complexities embedded in moisture transport. Therefore, the project proposed a different approach based on fundamental dynamic meteorology.

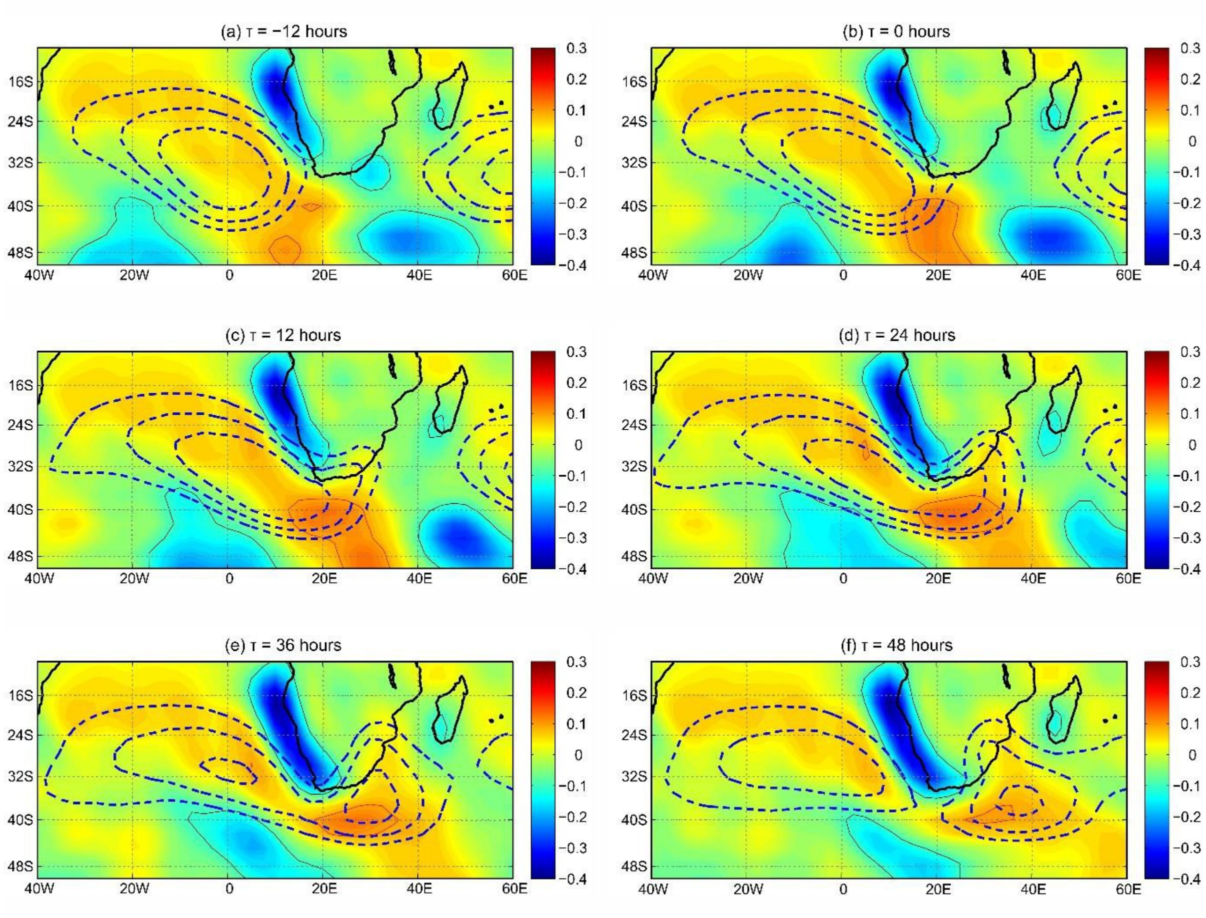

Figure 3.13: *Composites of PV anomalies (shaded; PVU) at 1000 hPa (just above MSLP) associated with the ridging Atlantic Ocean anticyclones in Figure 3.8 for τ (a) -12, (b) 0, (c) 12, (d) 24, (e) 36, and (f) 48 h. The lighter (darker) shading represents areas of positive (negative) PV anomalies. The thick dashed black contours represent 1018, 1020, and 1022 hPa. The anomalies over the western parts of South Africa are statistically significant at the 95% level.*

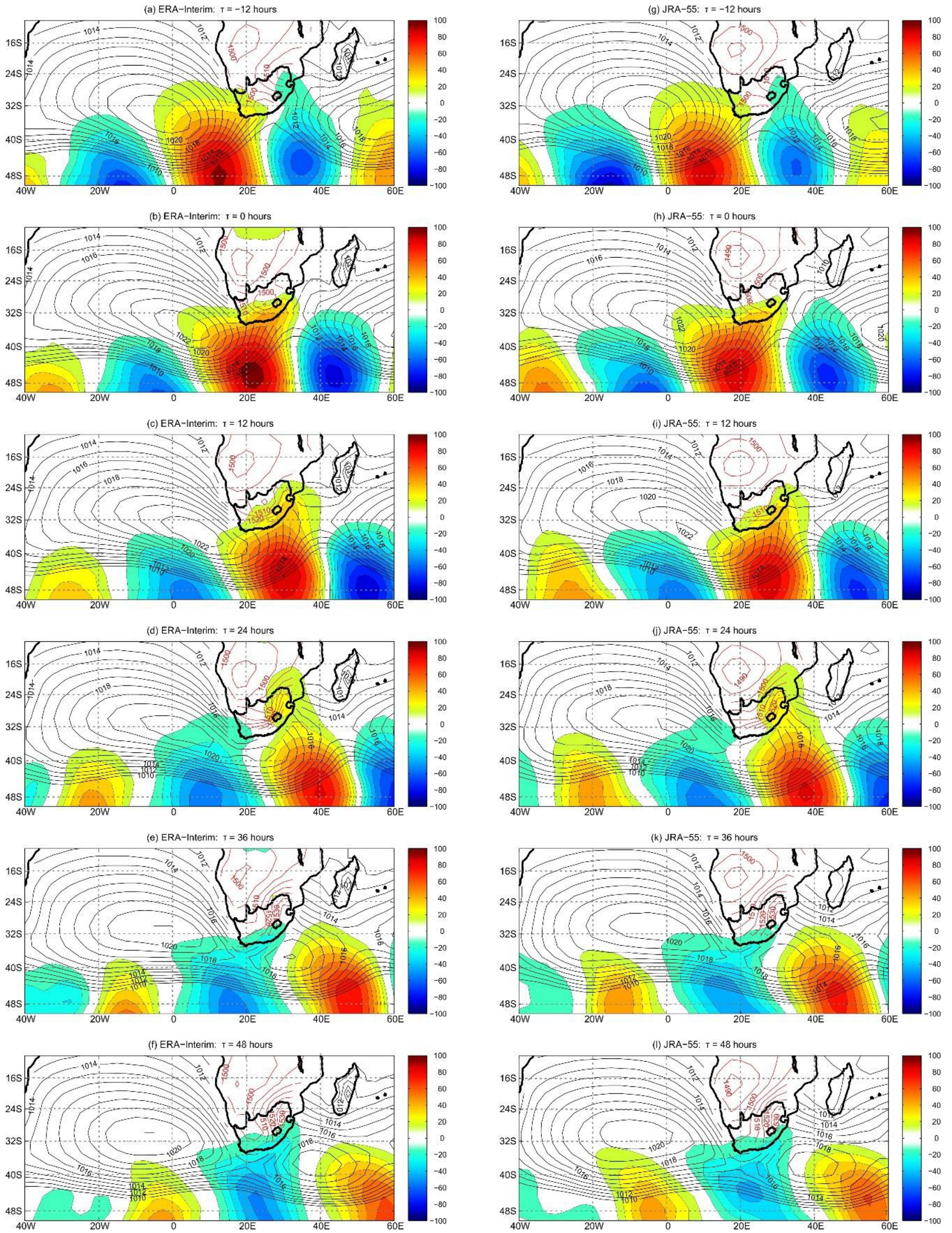

Figure 3.14*: Lagged composite evolution of the 850 hPa geostrophic (left panels) and ageostrophic (right panels) wind together with their divergence (brown shading) and convergence (blue shading) fields. The vector scale is 10 m s^{-1} and the shading plotted at 10^6 s^{-1}. The thick blue dashed contours represent the 1017 (outer), 1018 (middle) and 1021 (inner) hPa MSLP contours. The thick green curve is the 10 m day-1. The evolution of the fields begins from (a, g) one day before the inception of the ridging process (Day -1) to (e, j) the day after the ridging ceases (Day +4). The composites were produced using DJF ridging systems* from 1979 to 2018.

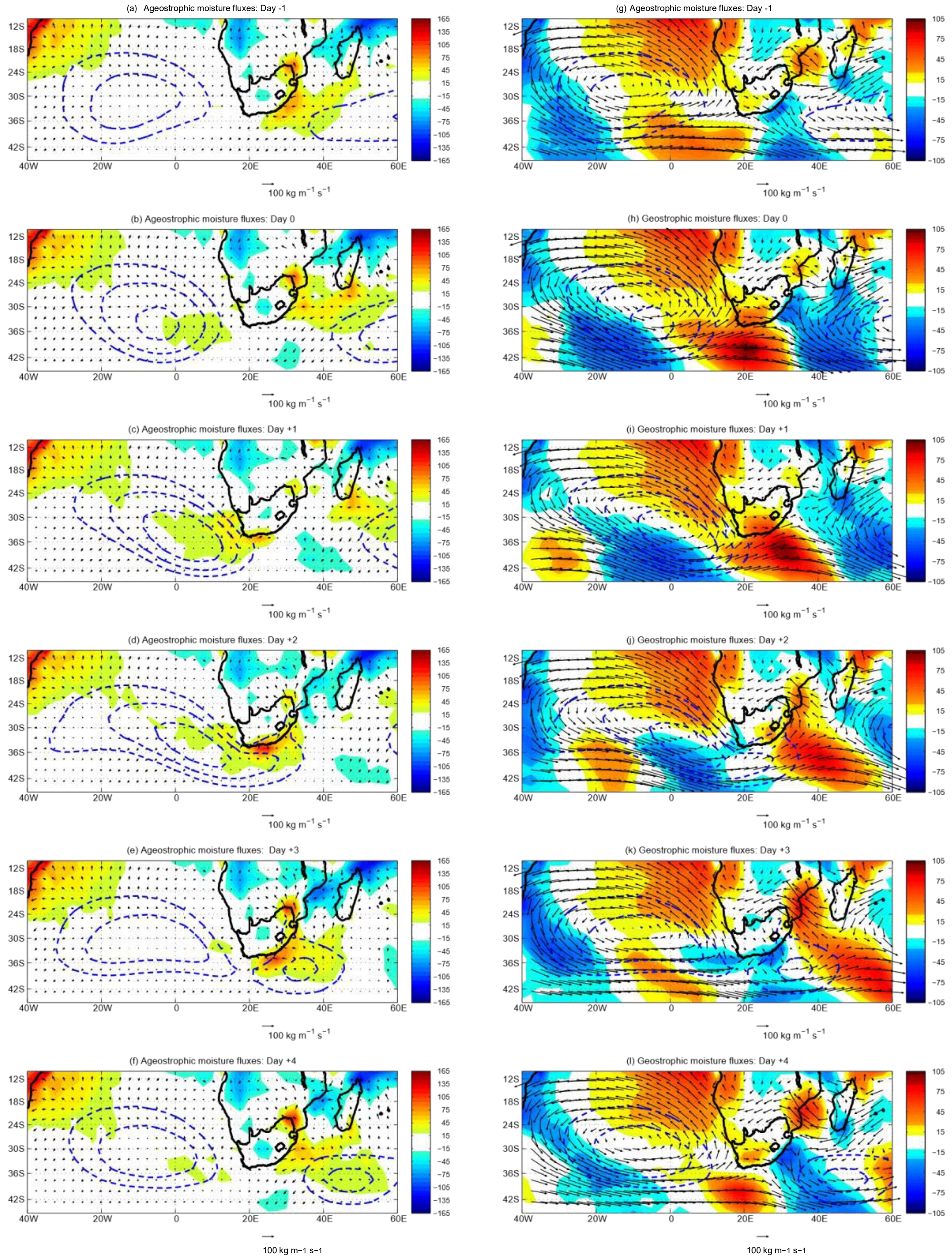

Figure 3.15: *Composites of ECMWF (left panels) and JRA (right panels) ridging anticyclones with a 48hour duration events shown as the evolution of MSLP over the oceans, contours plotted at 1 hPa intervals, and 850 hPa geopotential heights over land, contours at 5 gpm intervals. The shading represents positive (yellow to dark red) and negative (cyan to dark blue) 850 hPa geopotential height tendency. The composite evolution of the events begins from (a,f) τ = -12 hours to (e,j) τ = 48 hours, presented in intervals of 12hours.*

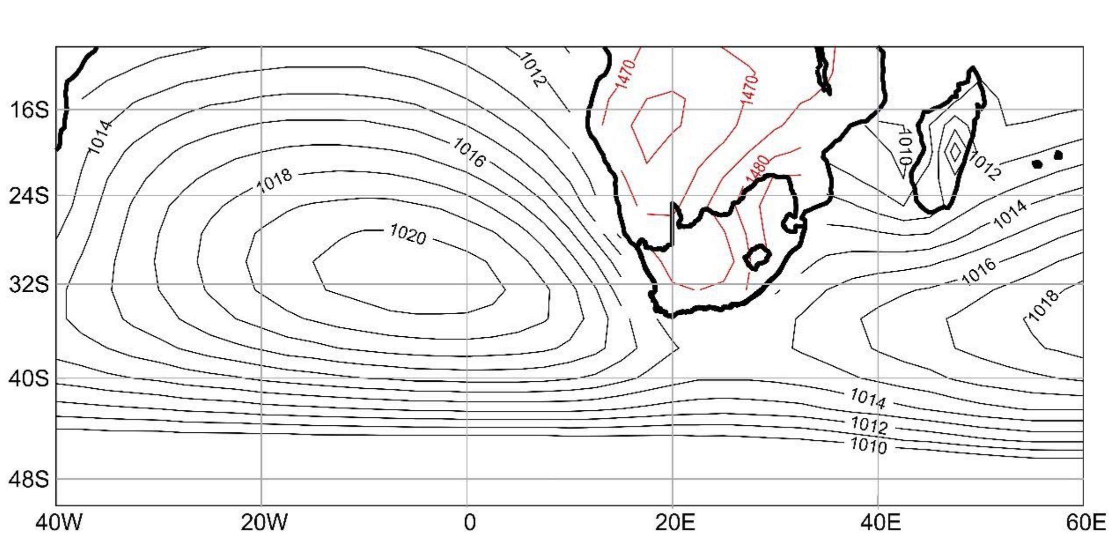

Figure 3.16: *December, January and February climatology of mean sea level pressure (black contours over the Ocean) and 850 hPa geopotential heights (black contours over southern African mainland) plotted at 1 hPa and 10 gpm contour intervals, respectively. The figure was produced using ERA-Interim reanalysis data sets for the 1979 to 2018 period.*

As a prerequisite to understanding the dynamics that influence the moisture transport or flux, we need to have a good understanding of the dynamics of the flow. One of the many novel contributions of this project is a diagnosis of the flow that is associated with ridging highs that decompose the flow into its geostrophic and ageostrophic components and assume that the Coriolis parameter changes with latitude, which Blackburn (1985) termed the geostrophy-1. When the geostrophic flow is defined in this manner, it is therefore not non-divergent, that is, $\nabla \cdot \mathbf{V_g} = -\beta f^{-1} v_g$ (Cook, 1999), which generally does not vanish. The ageostrophic flow, given by $\mathbf{V_a} = \mathbf{V} - \mathbf{V_g}$, therefore depends on how we define the geostrophic flow. In addition, to understanding the behaviour of the moisture fluxes over South Africa, particularly along the eastern coast, we follow Lima et al. (1991), Kwon and Lim (1999) and Holton and Hakim (2013) to decompose the ageostrophic flow into its isallobaric wind and the component representing advective effects. This decomposition can be represented more explicitly as follows

$$\mathbf{V_a} = f^{-1}\mathbf{k} \times \partial_t \mathbf{V_g} + f^{-1}\mathbf{k} \times (\mathbf{V_g} \cdot \nabla)\mathbf{V_g} \tag{3.3}$$

So due to the local increase in the strength of the geostrophic flow (first term on the right of Equation 3.3), the geopotential tendencies, that would be induced by the ridging high as it invades South Africa, have implications for the development, structure and orientation of the ageostrophic flow.

To understand this, we first briefly consider the geopotential height tendency fields that are induced by the ridging process, as shown in Figure 3.14. There exists a positive low level geopotential height anomaly located at the leading edge of the ridging, but unexpectedly, its centre is located in the midlatitude so that only the northern tip of it invades South Africa as the mean sea level isobars are oriented at acute angles to the eastern coast of the country. It is important to note that the part of the tongue of positive anomalies remains confined to the eastern parts of the country and it vanishes as soon as the leading edge of the ridging high has separated from the parent anticyclone, as the main geopotential anomaly pattern drifts eastward. This intruding tongue of positive low level geopotential anomalies is critical to the understanding of the ageostrophic flow that establishes over the south-eastern, eastern and northeastern interior of South Africa. The direction of the ageostrophic flow is mostly northeastward and is consistent with the positive geopotential tendency field (highlighted in Figure 3.15 by the green curve, which represents the 10 $m^{-2}\,s^{-1}\,day^{-1}$ contour). It is also consistent with the flow divergence and convergence patterns. We expect from the idealised model of the low level ageostrophic wind in baroclinic waves (Lim et al., 1991; Kwon and Lim, 1999; Holton and Hakim, 2013), that the flow will point away from the centre of positive geopotential tendencies. This is the case in Figures 3.15 (b) to (d).

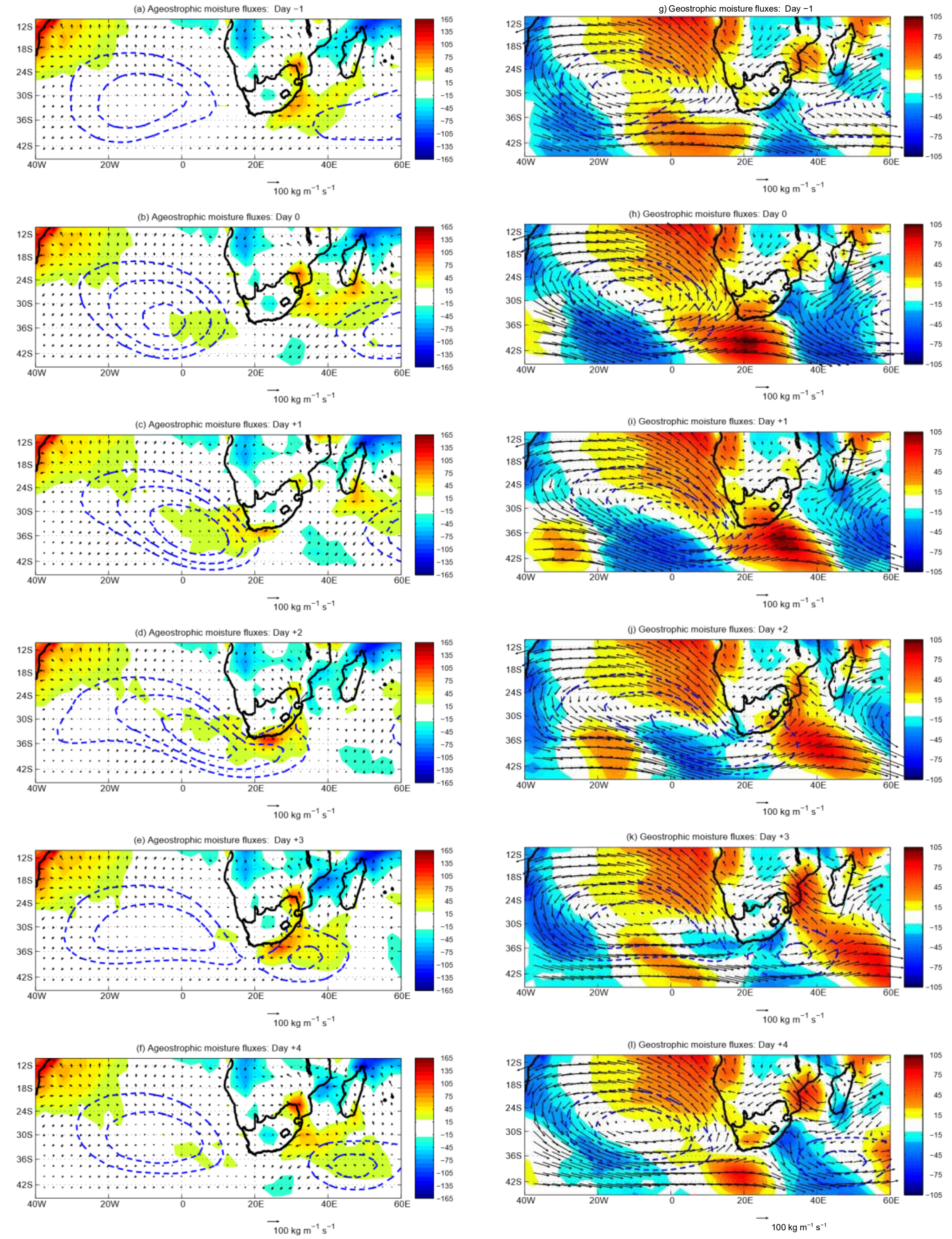

Figure 3.17: *As in Figure 3.15 but for low level moisture fluxes as defined in Equation 3.4.*

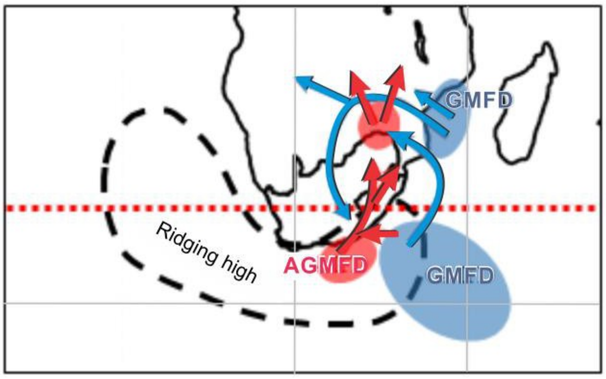

Figure 3.18: *Schematic summary of ageostrophic (red arrows) and geostrophic (blue arrows) moisture fluxes. The red and blue shaded areas represent the ageostrophic (AGMFD) and geostrophic moisture flux divergence (GMFD), respectively. The dashed contour represents a mean sea level pressure contour depicting a ridging South Atlantic Ocean Anticyclone and the red dashed line represents the 30˚S latitude line.*

As noted above, the ageostrophic flow may be decomposed into isallobaric and advective components. The largest Eulerian acceleration of the geostrophic flow occurs on land, precisely where the ageostrophic flow increases from one time step to the next (Figure 3.15). Composites of the isallobaric wind suggest that, in particular Eulerian acceleration of the zonal component of the geostrophic wind ($\partial u_g/\partial t > 0$), which spatially coincide with the arrows representing the ageostrophic wind, contributes the most to these increases. This shows that the magnitude of the latter is informed by the former.

The form of the geostrophic flow used in this study is not non-divergent. Examination of Figures 3.15(g) to (l) shows that before the inception of ridging at day 0, there is a weak geostrophic convergence in the SWIO. As the ridging evolves and matures, flow divergence extends from the South Atlantic Ocean, eastward following the MSLP isobars, as they also extend eastward. From day +2, the geostrophic flow divergence dominates in the SWIO, with a local maximum found in the Mozambique Channel. Overland, flow convergence extends south, forming a tongue that dominates much of South Africa. The geostrophic flow, represented by the arrows, is consistent with the flow divergence/convergence fields. It starts off parallel to the coast (see Figures 3.15 (h) to (i)), and then turns anticyclonically, to enter the country north of 30˚S (Figures 3.15 (j) and (l)). The flow entering the country originates from the SWIO flow divergence just described, and it continues to turn anticyclonically into the interior of the country. In contrast, the ageostrophic divergence field tails behind that of its geostrophic counterpart, right through the evolution of the ridging and is confined south of 30˚S. They are also largely confined to the coast. So before the orientation of the ageostrophic flow discussed above is established by the isallobaric forcing, it enters the country along the southern coast.

One issue to note is the behaviour of the ageostrophic flow over the north-eastern part of South Africa, where a climatological terrestrial that appears to be an extension of the Indian Ocean anticyclone (see Figure 3.16). Due to the physical arguments made above, the ageostrophic flow points in all directions from the north-west to the north-east, whilst the geostrophic wind flows around it in an anticyclonic fashion that is consistent with the geopotential heights, after entering the subcontinent from the Mozambique Channel.

As noted above, based on the decomposition of the flow as described above, the moisture flux into South Africa from the SWIO is defined as follows.

$$\mathbf{Q} = \frac{1}{g}\int_{600}^{p_s} q\mathbf{V_h}dp = \frac{1}{g}\int_{600}^{p_s} q\mathbf{V_g}dp + \frac{1}{g}\int_{600}^{p_s} q\mathbf{V_a}dp = \mathbf{Q_g} + \mathbf{Q_a} \tag{3.4}$$

Unlike previous studies that have considered this issue in the southern African domain, in this project the moisture fluxes are decomposed into geostrophic and ageostrophic components. In this way, it is much more straight forward to link the moisture fluxes to the characteristics and behaviour of the flow. Similar to the ageostrophic flow, the ageostrophic fluxes enter the country from the southern coast (and always south of 30°S), from the SWIO waters that are adjacent to the country, as the South Atlantic high forms the bean shape, and the leading edge of the high breaking off. The ageostrophic moisture is transported in a northeasterly direction, confined over the eastern half of the country, into the terrestrial continental high. It is further transported out of the high in different directions, as the flow. The geostrophic fluxes enter the country from the Mozambique Channel. This moisture breaks up into two branches, one that is anticyclonic around the terrestrial high, and another that eventually becomes cyclonic, in a manner that is consistent with the Angola low.

3.4 Medium-range forecasts of ridging high pressure systems

In this subsection, a case study of a ridging high event is used to demonstrate the value of implementing dynamical and regime specific post-processing of EPS data, in particular, the relationship between RWB and ridging highs as discussed in Subsection 3.3.2. Prior to this project, no objective methodologies had been developed to identify ridging highs and RWB events in EPS forecast outputs.Therefore the forecasting of these two types of dynamical processes in EPS data is largely subjective and based on visual inspection and experience of forecasters at the South African Weather Service. Figure 3.20 (a) shows NCEP EPS forecasts of ridging high and Figures 3.2 (b) to (e) show EPS forecastsof RWB events on the 320, 330, 340 and 350 K dynamical tropopause, respectively. These were produced by implementing the methods of this chapter as described in Subsection 3.2.2 in forecast modein the manner outlined in the flow charts as shown in Figure 3.19. These event-based forecasts are associated with a severe rainfall event that occurred in April 2019. The clear advantage of the event-based EPS forecast is its easy assessability, whether ridging systems are predictable or not.

It is clear in this example that there is uncertainty with regards to the inception of the event because of an ensemble spread of the timing of the inception of the ridging event. Another source of uncertainty is the duration of the events. There are rather large differences between the duration of events as predicted by the different ensemble members. However, at least for this particular case, the actual occurrence of the ridging high was predicted by all ensemble members. Unfortunately, the relationship between ridging highs and RWB does very little in reducing the uncertainties that have just been described, but explains other aspects in the predictability problem of ridging highs at the MRF time scale.

In Subsection 3.3.3 it was revealed that different aspects of the horizontal flow have different roles in bringing in moisture into the country. This must be tightly coupled with the orientation of ridging events relative to the country, and therefore might affect the associated rainfall forecasts. According to ERA Interim (see Figure 3.21), a ridging system developed at t = +156 hours on 20 April 2019. As expected, from the dynamical analysis above, a RWB on the 330 K (thick red contour) dynamical tropopause, a strong undulation is observed. The wave breaks as the ridging occurs. Given this coupling, the question then arises, does the NCEP GEPS predict this behaviour. Figure 3.22 displays the same fields as those shown in Figure 3.21 but for the NCEP GEPS ensemble mean. There are important differences, for the case presented here, between observations and the ensemble forecast. There is no observed overturning on the forecast 330 K dynamical tropopause behaviour, which is evident in ERA Interim data. This leads to a more zonally confined ridging high process, which can therefore affect the predictability of the rainfall that might occur in the South African domain. There is also a difference in the timing of the PV overturning between the model and observations, particularly on 340 K isentropic surface, which can be used to quantify the forecast skill of the event.

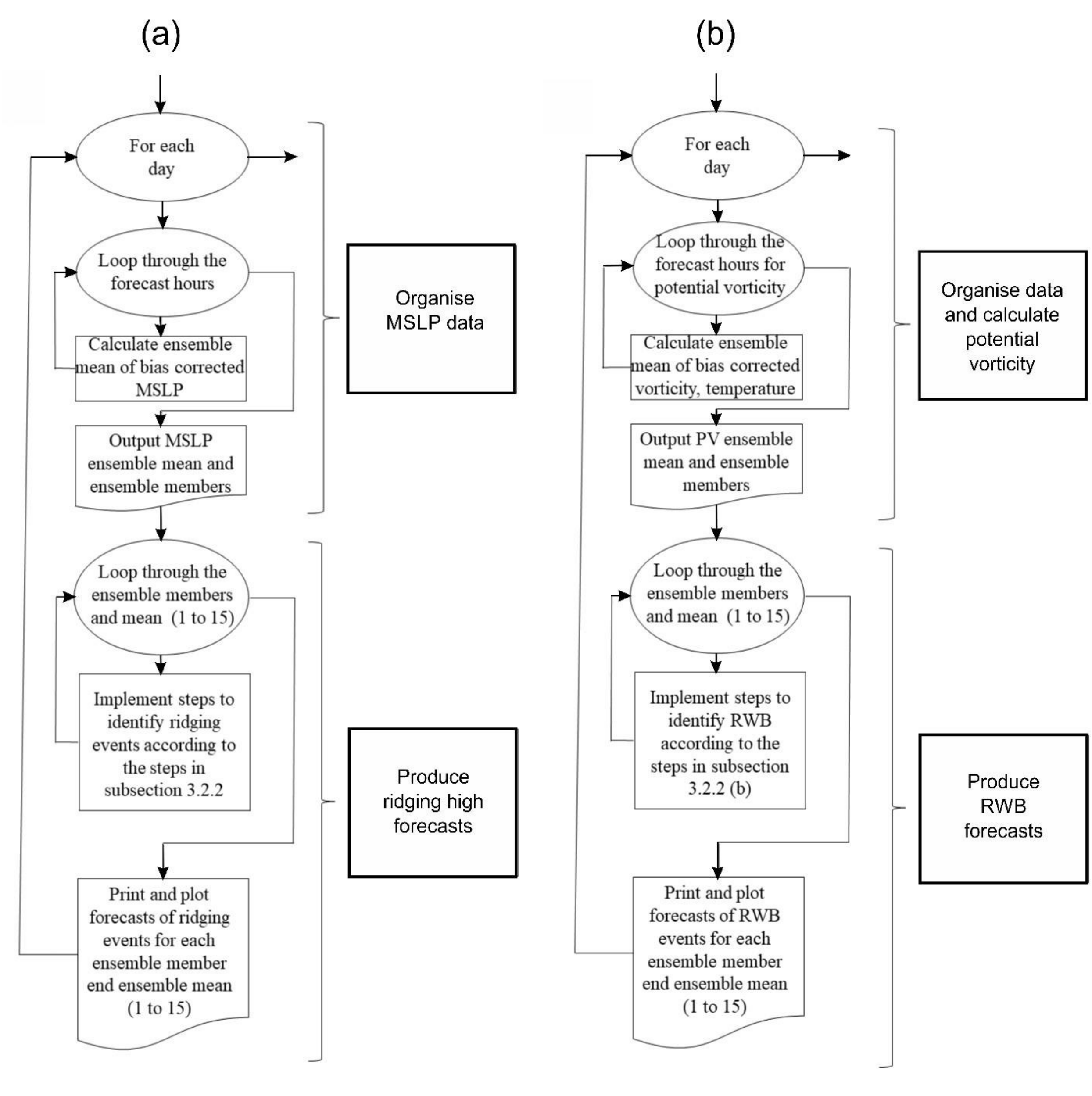

Figure 3.19: *(a) A flowchart of the ridging forecasting system and (b) the RWB forecasting system.*

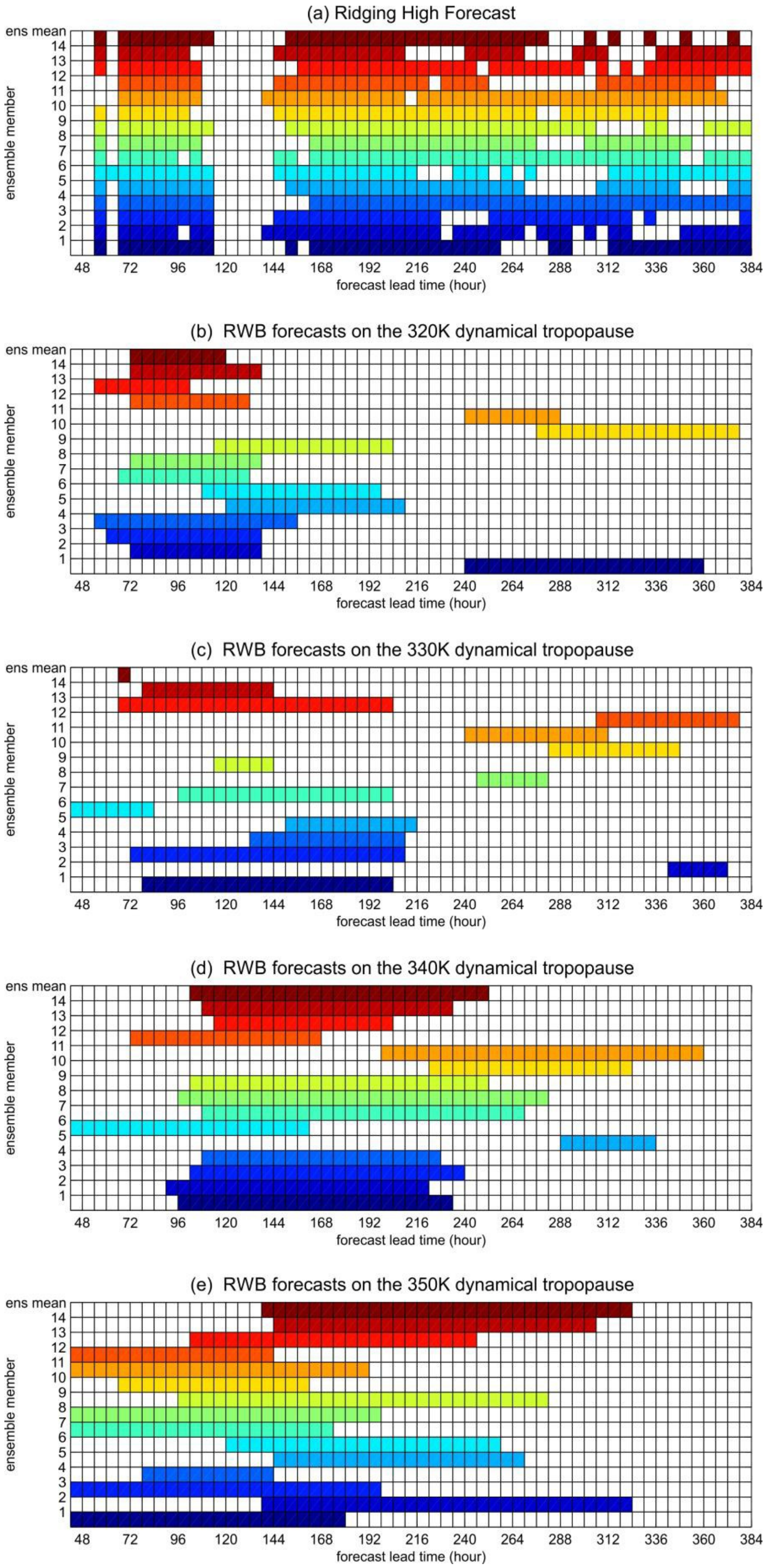

Figure 3.20: *Colour matrix representation of medium-range forecasts of*

(a) ridging systems and RWB events on the

(b) 320,

(c) 330,

(d) 340 and

(e) 350 K

dynamical tropopause produced by the NCEP GEPS on the 00:00 UCT 14 April 2019 up to 384 ahead.

The different colours in the scheme represent the forecasts of ridging highs by each ensemble member, with the ensemble mean at the top of the matrix. The white blocks represent hours for which no ridging high was predicted for this forecast window. The first (last) block with a colour represents the onset (cessation) of the ridging process as defined in the text. The total number of blocks on each row from left to right, with no interruption (i.e. no white) represents the duration of the riding event.

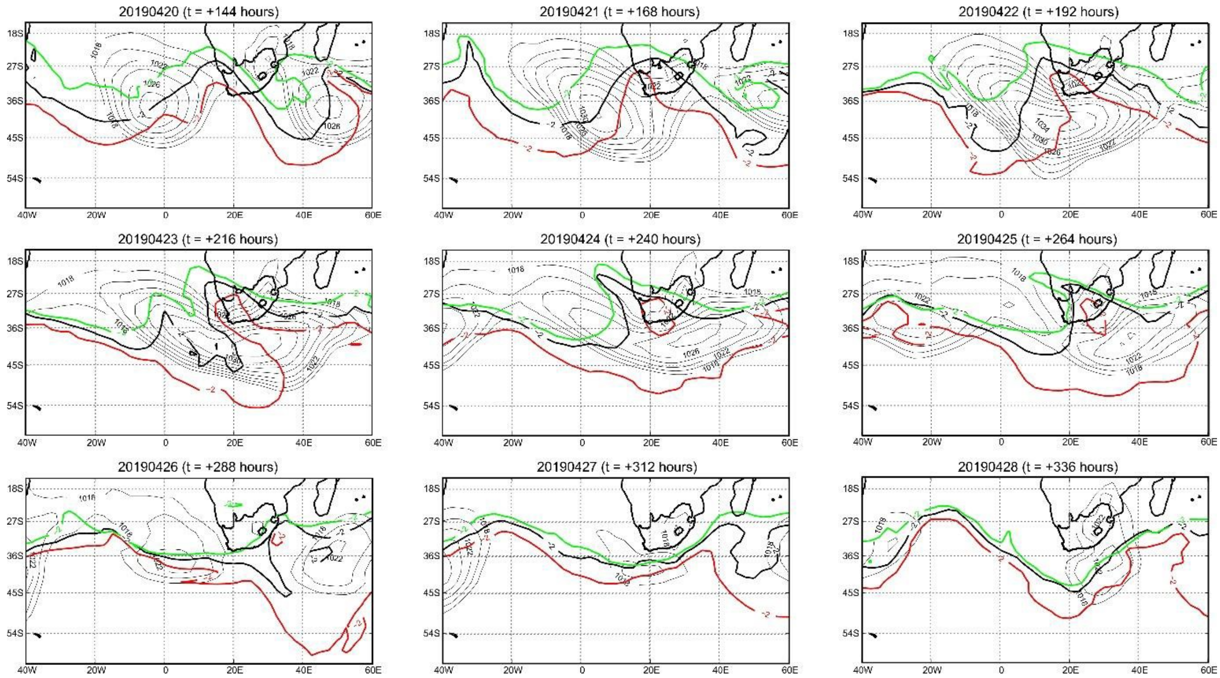

Figure 3.21: *An example of a ridging system in ERA Interim reanalysis that started on 20 April 2019 at 0:00 (t = +144 hours) to 28 April 2019 (t = +336 hours). The lead times of a forecast that was produced on 00:00 UCT 14 April 2019 are shown in brackets in the title of each panel. The fields shown are mean sea level pressure (thin black contours), PV = -2 PVU on the 330 K (thick red contour), 340 K (thick black contour) and 350 K (thick green contour).*

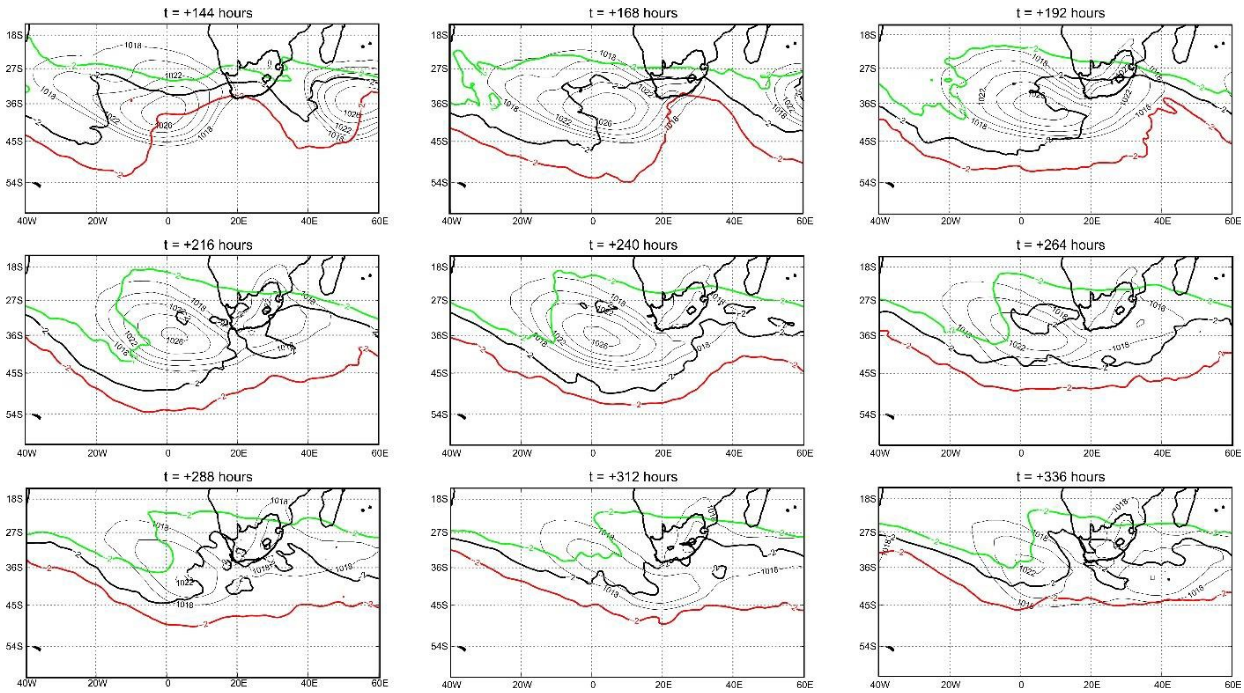

Figure 3.22: *Same as Figure 3.19 but for the NCEP GEPS ensemble mean.*

3.5 Summary

In this chapter, it was explained that ridging systems are coupled with lower stratospheric dynamical processes. The dynamics at this level are characterised using potential vorticity overturning, signalling the presence of breaking waves that are associated with the ridging high process. As the waves break, they propagate the information towards the surface by means of potential vorticity anomalies and vertical coupling mechanisms. In fact, the waves break before the ridging process commences. The morphology of Rossby wave breaking is anticyclonic and it is part of propagating the Rossby wave packet (or train) that originates from South America. In addition to the vertical coupling, the one way in which the ridging high events bring moisture into the South African domain was also considered, exploiting dynamical knowledge that can be used to incorporate processes in forecasting products.

This dynamical state of affairs is also seen in EPS data and is based on the successful implementation of the objective methods designed to identify ridging high and Rossy wave breaking events in forecast mode in EPS data. On this basis, event-based forecasts can now be produced. From the assessment presented in Section 3.4 ridging systems appear to be highly predictable because their occurrence is observed in all ensemble members. This is given credence to by the fact that the ensemble member also exhibits reasonable skill in predicting the associated Rossby wave breaking events. Therefore the addition of this new information to EPS forecasting can improve the predictability of these systems.

4

Cut-off low pressure systems

Chapter 4 is based on the following research outputs that were funded by this project:

- Ndarana T., Rammopo T.S., Bopape, M, Reason C. and Chikoore H. (2021). Downstream development during South African cut-off pressure systems. *Atmospheric Research*, 249, 105315.
- Ndarana T., Rammopo T.S. Chikoore H., Barnes M.A. and Bopape M. (2020) A quasi-geostrophic diagnosis of cut-off low pressure systems over South Africa and surrounding ocean. *Climate Dynamics*. 55, 2631-2644.

4.1 Background

In the previous chapter aspects of the general dynamics of the ridging high pressure systems and the dynamical processes that underlie how these systems transport moisture into South Africa, were discussed. Furthermore, the use of this knowledge about their dynamics was used to post-process MRF data to establish the hypothesis that the predictability of these weather systems on the ten day forecast horizon can be improved. As noted in that chapter, ridging high pressure systems by themselves do not cause rainfall because they are lower tropospheric processes and so they require upper air systems that provide a mechanism that causes vertical ascent in such a way that moist air saturates and rainfall occurs as a result. One such upper air system is the cut-off low (COL) pressure system. A COL is a deep low pressure system that develops from unstable baroclinic waves (Favre et al., 2013) and characterised by a closed, cold cored cyclonic circulation. Over South Africa, these systems occur on the equatorward side of the jet, where anticyclonic barotropic shear is found (Thorncroft et al., 1993), after having been detached from the westerly flow that is associated with this jet (Palmen and Newton, 1969; Pinheiro et al., 2017; 2019).

Nieto et al. (2005) presented the evolution of COLs as a four stage process, that includes a tear-off stage that is followed by a cut-off of the closed cyclonic circulation, thus defining the detachment mentioned above. The closed circulation that characterises these two stages of COL evolution is induced by negative potential vorticity (PV, Hoskins et al., 1985) in the Southern Hemisphere. This means that within the COL there is a blob of high PV air, signalling that this air has stratospheric origins. Ndarana and Waugh (2010) proposed that this air is transported isentropically from the lower stratosphere into the upper levels of the troposphere. They showed this by linking Rossby wave breaking to the COLs and showed that in one reanalysis dataset, about 89% of the COLs were preceded by the breaking waves. This was later confirmed by Barnes et al. (2021) using a different reanalysis dataset. As a matter of fact the latter showed that nearly every COL has a RWB event associated with it in the Southern Hemisphere. It follows then that COLs are preceded by RWB and this finding may be used to improve confidence in MRF forecasts of COLs as was the case with ridging high pressure systems.

RWB is influenced for the most part by the ambient flow. It was shown in Ndarana and Waugh (2010) and Reyers and Shao (2019) that the flow associated with the combined evolution of RWB and COLs is characterised by a split jet structure, with one large scale jet to the south of the closed circulation and a smaller scale jet to the north of the circulation. However, the dynamics of the evolution of these jet streaks had not been analysed before this project. An improved understanding of the dynamical processes involved in the evolution of the jet streaks was considered a good first step towards systematically understanding the dynamics of South African COLs, thereby potentially improving their predictability at the MRF time scale.

After understanding of the dynamics of the jet streaks associated with COLs has been established, their impact and role in the dynamical precursors of COLs need to be established, as a prerequisite to improving their predictability at the MRF. A critical concept that could be important for COLs is downstream development (Orlanski and Sheldon, 1995). Since it is not a well-known concept in South Africa, it would be instructive to provide details of it here using schematic diagrams. As discussed in the previous chapter, the flow may be decomposed into its geostrophic and ageostrophic component, such that $\mathbf{V} = \mathbf{V_g} + \mathbf{V_a}$. Figure 4.1 shows a schematic illustration of a propagating baroclinic wave and the flow associated with it in the Southern Hemisphere. As noted in Orlanki and Sheldon (1991) the flow will be subgeostrophic in the trough and supergeostrophic in the ridge. These flow conditions are characterized by $u_a < 0$ and $u_a > 0$, respectively. This is suggested by red curved arrows in Figure 3.1. Since the geopotential anomaly (φ^0) fields are negative (positive) in the trough (ridge), the correlation

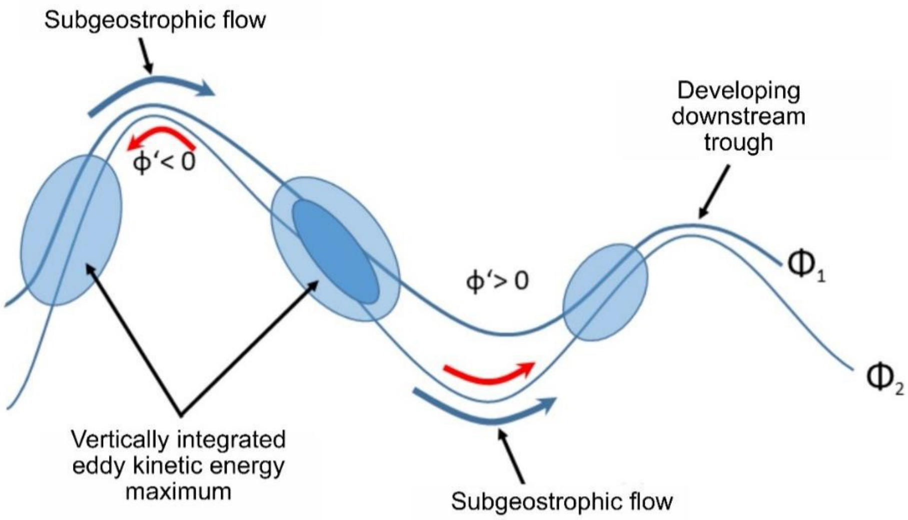

Figure 4.1: *A schematic representation of the relationship between the various components of a baroclinic wave. The upper level geopotential contours are represented by the thick blue contours labels* Φ_1 *and* Φ_2. *The geopotential anomalies are,* φ^0 *shown in regions where they are negative and positive and are a maximum (in absolute value) along the trough and ridge axes, respectively. Airflow relative to the wave is represented by means of the blue arrows, and the red arrows represent the ageostrophic flow. The oval shaped structures are the centres of the vertically integrated eddy kinetic energy and the differences in shading indicate the strength. [Adapted from Orlanski and Sheldon, 1993].*

between the ageostrophic flow and the anomalies (i.e. $u_a\varphi^0$) will always be directed downstream. This is an essential quantity in the downstream development process. Note that the eddy energy centres are located at the inflection points. Therefore the main point to this diagram is that the eddy kinetic energy in a baroclinic wave develops and dissipates away from the trough and ridge axes, and the energy transfer, which is facilitated by the flow across the trough and ridge axes, is likely to be always downstream.

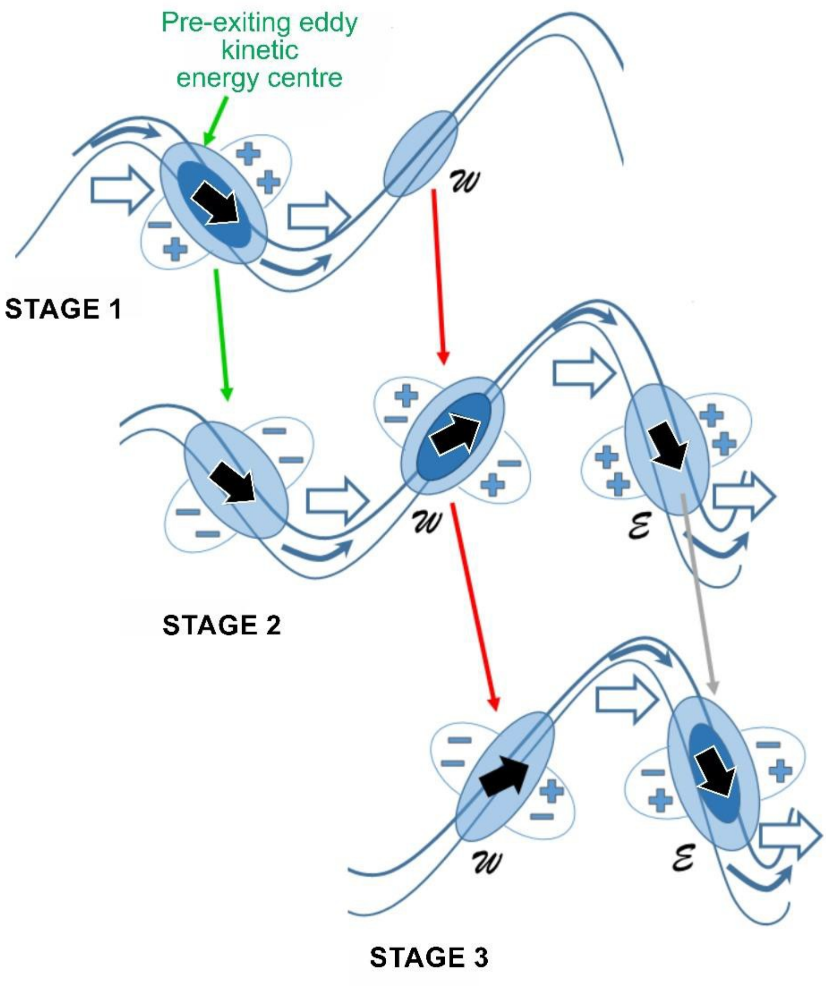

Figure 4.2: *A schematic illustration of the three stages of development during the evolution of a baroclinic wave. The oval shapes are the eddy kinetic centres (with the darker shades representing the strength of the centre), the plus and negative signs around the centres are the sources and sinks of eddy kinetic energy, respectively. The blue curved arrows are the upper airflow, the thick black contours are the eddy kinetic energy flux and the white arrows are the ageostrophic geopotential fluxes. Three stages are shown: Stage 1 – Upstream system decay and generation of energy centre W, west of the new trough via the ageostrophic geopotential fluxes. Stage 2 – Energy fluxes emanate from a mature W centre and foster growth of a new energy centre E east of the trough downstream trough. Stage 3 - The eddy kinetic energy W dissipates, whilst the energy centre E matures. [Adapted from Orlanski and Sheldon, 1993].*

Figure 4.2 shows a schematic representation of the evolution of a baroclinic wave and the associated eddy kinetic energy structures and their fluxes, which involves three stages of development. The various processes involved in the sequence of events presented below are described in terms of the eddykinetic energy equation (Orlanki and Katzfey, 1991), given by

$$\partial_t K_e = -\nabla_p \cdot (\mathbf{V}K_e) - \partial_p(\omega K_e) - \mathbf{v} \cdot \nabla_p\varphi + [\mathbf{v} \cdot (\mathbf{u} \cdot \nabla)\mathbf{V}_m] + \mathrm{R} \tag{4.1}$$

which is the K_e equation.

Orlanski and Katzfey (1991) decomposed the K_e generation term $-\mathbf{v} \cdot \nabla_p\varphi$ as follows

$$-\mathbf{v} \cdot \nabla_p\varphi = -\omega\alpha - \nabla_p \cdot (\mathbf{v}\varphi)_a - \partial_p(\omega\varphi) \tag{4.2}$$

The first term on the right hand side of Equation 4.2 (i.e. $-\omega\alpha$) is the baroclinic conversion term between the eddy available potential energy and eddy kinetic energy. It is likely to be strongest where the eddy kinetic energy centres are situated in the wave. As in Orlanski and Sheldon (1993), we assume a variable f so that

$$(\mathbf{v}\phi)_a = \mathbf{v}\phi - \mathbf{k} \times \nabla\left(\frac{\phi^2}{2f(y)}\right) \tag{4.3}$$

which is the ageostrophic geopotential flux. It follows then that K_e is generated by two processes, namely (a) baroclinic conversion, which is caused by vertical eddy heat fluxes and (b) ageostrophic flux convergence (second term on right hand side of Equation 4.2). This system of energy equations was then used by Orlanski and Sheldon (1995) to describe downstream development, involving two energy centres, one upstream and the other downstream, during which K_e is moved by means of energy fluxes ($\nabla_p \cdot (\mathbf{V}K_e)$), whilst the upstream centre radiates energy downstream into the centre to the east of it by means of the ageostrophic geopotential fluxes in Equation 4.3.

Based on this diagnostic framework, the three stages of the evolution of a baroclinic wave may be presented as follows

STAGE 1:

Upstream system decay and the generation of energy centre *W* west of a new trough. The analysis begins while the baroclinic wave is propagating, and so we assume a matured K_e centre that is located at the inflection point just west of the ridge axis of a pre-existing positive geopotential anomaly and east of the trough axis of a pre-existing trough. As this K_e centre is matured (and therefore cannot grow any further) it can only lose energy, and it does so by means of ageostrophic fluxes (i.e. $(\mathbf{v}\varphi)_a$), which are located at the ridge axes and directed downstream, as noted above. This downstream energy flux gives rise to the development of a new K_e centre, which is marked by the letter *W*, standing for west of the rough axis of an incipient trough. And so $\partial_t K_e < 0$ in the pre-existing K_e structure and $\partial_t K_e > 0$ at the K_e marked *W*. This pattern of local rate of change is caused by the divergence of the ageostrophic energy flux $-\nabla_p \cdot (\mathbf{v}\varphi)_a < 0$. This field has the opposite sign downstream where the *W* eddy kinetic energy develops.

STAGE 2:

Energy fluxes from mature *W* and growth of eddy kinetic energy centre *E*, east of the downstream trough. From stage 1 to stage 2, the pre-existing K_e centre dissipates (as seen by following the green arrow) and the western K_e has matured (follow the first red arrow). The maturing of *W* is the first signature of this stage. Because it can develop no further than this as it has saturated, it can only lose energy and does so by means of the ageostrophic flux, that is strongest at the trough axis, downstream of it. This energy is deposited at the inflection point located east of the trough axis, thus giving rise to the development as a new energy centre *E*. Because of ascending motion east of the trough axis, E is also generated by baroclinic conversion from eddy available potential energy ($-\omega\alpha > 0$). This is combined with $-\nabla_p \cdot (\mathbf{v}\varphi)_a > 0$ that is caused by the loss of energy from W and convergence of this energy flux at E.

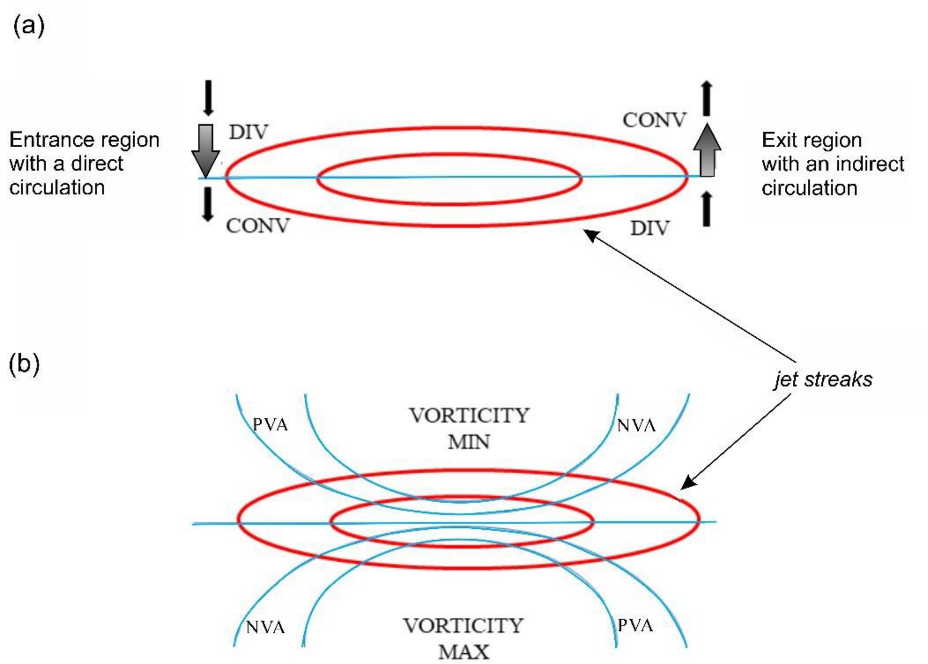

Figure 4.3: *Schematic representation of an upper level straight jet streak (red contours are the zonal isotachs) with patterns of (a) divergence/convergence and the transverse ageostrophic wind component associated with the jet entrance/exit regions and (b) positive vorticity advection (PVA) and negative vorticity advection (NVA). The thin blue contours in (b) represent the relative vorticity field, with a vorticity maximum and minimum on the cyclonic and anticyclonic of the jet streak, respectively. [Adapted from Uccellini and Kocin, 1987].*

STAGE 3:

Dissipation of energy centre *W*, maturation of energy centre *E*. From state 2 to stage 3, the W kinetic energy centre dissipates (as it is losing energy and saturated in stage 2). This can be seen by following the second red arrow. The E centre grows to reach maturity at this stage (follow the grey arrow).

The effect of $\mathbf{V}K_e$, represented in Figure 4.2 by means of the thick black arrows, has not been considered. The nature of the ageostrophic energy flux may be considered microscopic as it transfers energy from one K_e centre to the next one downstream. $\mathbf{V}K_e$ is the energy flux that is facilitated by the total flow within the system and therefore accounts for the translation of the whole system from west to east. In this sense, it may be considered macroscopic in nature. Note also that $\partial_p(\omega K_e)$ in Equation 4.1 and $\partial_p(\omega\varphi)$ in Equation 4.2 are small as a result of the vertical integration that is proposed when implementing these diagnostics and therefore need not be considered here as they are of little significance. Also $[\mathbf{v}\cdot(\mathbf{u}\cdot\nabla)\mathbf{V}_m]$ is a barotropic conversion from K_e to K_m, where the latter is defined as the mean kinetic energy. K_m is considered constant as a function of time unless the basic state is defined as the low frequency flow.

Embedded herein are issues of jet streaks. As reviewed in Keyser and Shapiro (1986) the jet streaks are co-located with the K_e centres in a baroclinic wave and seldom propagates across the trough axes. We present schematics of the relevant fields that are associated in Figure 4.3. At the jet entrance there exists a thermally direct ageostrophic circulation with divergence on the anticyclonic confluent flow of the jet streak and upward vertical motion across the isentropic surfaces. The air descends on the poleward side. The opposite takes place at the jet exit, where the transverse circulation is thermally indirect. Furthermore, the divergence (convergence) at both ends of the jet is associated with positive (negative) vorticity advection.

The breaking wave process that is associated with COLs and identified in Ndarana and Waugh (2010) and Reyers and Shao (2019) is caused by the propagating midlatitude jet streak, as it brings with it strong barotropic shear and increased strain rate (Nakamura and Plumb, 1994). Therefore, improving the understanding of dynamics of the jet streaks could contribute to improved predictability of COLs because these precede the formation of the closed circulation. The same applies to downstream development. However, the latter has not been established for COLs, certainly not for COLs in the South African domain.

4.2 Data and methods

4.2.1 Data

The same datasets as in the previous chapter are used.

4.2.2 Methods

(a) COL detection algorithm

The method for identifying COLs that is suitable for the applications to this project was described by Ndarana and Waugh (2010) and improved by Barnes et al. (2021) by including a calculation that identifies closed contours that exploit the *contourc* MATLAB function, as was done for ridging highs in the previous section.

First, for each 6 hourly time step, contours of 500 hPa geopotential heights at 10 gpm contour intervals from the minimum to the maximum geopotential height value, are obtained. For a contour to be considered closed, the longitudes and latitudes of the beginning and end of it must be exactly the same. The centre of each closed contour is the middle most grid point and these points are saved as potential COL points. In the second step, we exclude tropical, subpolar and polar lows as potential COLs by requiring that the latitude and longitudes centres of the closed contours be confined to the 15° – 50°S latitude ring, following Singleton and Reason (2007).

The first two steps identify potential closed circulations but do not distinguish between high and low pressure systems. To do this, in the third step we further require that the geopotential height value at each potential COL point be lower than the values of the 6 surrounding grid points by a minimum of 10 gpm (Nieto et al., 2005, Rebeita et al., 2006). The fourth step ensures that the closed contours comprise a cyclonic circulation that is detached from the westerly wind belt and in addition it is required that the zonal component of flow, south of the potential COL point, be negative.

COLs have a cold core (Pelmén and Newton, 1969). As in Ndarana and Waugh (2010), we use the 850 to 500 hPa thickness fields to separate potential COL points that comply with the cold core condition from those that do not. A COL point is considered to be associated with a cold core of the close cyclonic circulation if its thickness value is lower than that of at least five of the surrounding grid points surrounding it. All the COL points that do not comply with this requirement are then filtered out. This constitutes the fifth step of the algorithm.

In the sixth step, concentric closed contours are then grouped together and considered to characterise the same COL pressure system. This is done by requiring that COL points that belong to the same COL be within a 10° x 10° grid box. The final COL point is the centroid with the lowest 500hPa geopotential height and all the other COL points are discarded. A subjective inspection of the COL points revealed that some COL pressure systems have missing time steps in between. Porcu et al. (2007) observed a similar problem in their study. This is a problem that materialises in 6-hourly data because, in studies that employed daily data (Ndarana and Waugh, 2010, Reboita et al., 2010), it did not happen. A COL was deemed to have a gap if there were no more than two consecutive missing 6-hourly detections. Gaps in the COL were filled with a closed contour, low pressure minima point database. This database was created as with the COL database, but without applying zonal wind or cold core conditions. A gap was filled by a low pressure minimum point within a $5^{\circ} \times 5^{\circ}$ degree box of the previous COL point if it existed.

In the eighth and final step, we determine the evolution of the COLs. To do this, we employ the distance which a COL is likely to travel within a 6-hour period. Because COLs are synoptic systems, their time scale is $L/U \sim 10^5$ s. This translates to the fact that in six hours these systems are likely to travel less than 1000 km, assuming that $U \sim 10$ m s^2 (Holton and Hakim, 2014). Using this criterion, all consecutive COL points that occur within a 1000 km radius comprise a single system. After implementing all these steps, we found that the maximum distance between any two consecutive COL points is less than 1000 km and is 165 km on average. From this, the duration of COLs is then determined. Only cases that develop and dissipate east of 60°W and 50°E were considered for this study to cover South African and surrounding oceans.

(b) Composite analysis

We first calculate all the fields that will be used in the analysis, as will be discussed in Section 4.3. Unlike ridging highs in Chapter 2, there is much variability of the centres of the COLs, meaning that for the composite means to make climatological sense, the COLs (and all the fields used below) are brought into phase in the following manner

- For each variable, a subset of the data bounded by $(\varphi_c - 22.5^{\circ}, \lambda_c - 50^{\circ})$, $(\varphi_c - 22.5^{\circ}, \lambda_c + 50^{\circ})$, $(\varphi_c + 22.5^{\circ}, \lambda_c + 50^{\circ})$ and $(\varphi_c + 22.5^{\circ}, \lambda_c - 50^{\circ})$ is extracted from the SH fields.

- The subset fields are then brought together so that the (φ_c, λ_c) coincide. This essentially brings all the geopotential heights and other variables into phase, as noted above. The fields are then averaged and the evolving composite fields are produced as functions of relative latitude, relative longitude and time.

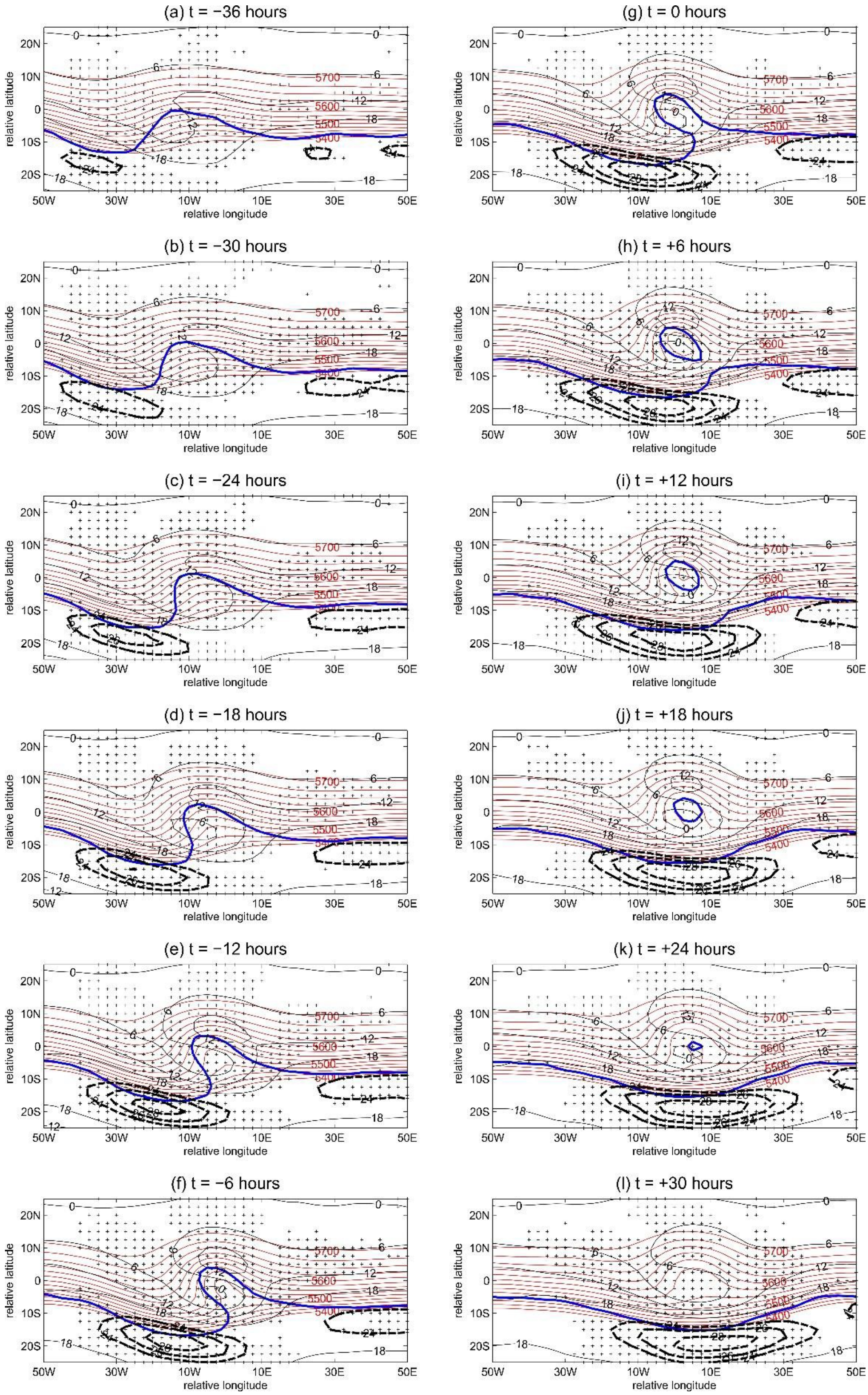

Figure 4.4: *Time-lagged composites of 500 hPa geopotential heights (red contours), zonal component of the 500 hPa geostrophic wind (black contours with thick dashed contours highlighting the jet streak) and -3 PVU contour (thick blue contour) on the 330 K isentropic surface. The zonal geostrophic isotachs are plotted in 6 m s^{-1}. The jet streaks highlighted by the thick black dashed contours are plotted in 2 m s^{-1}. The crosses represent areas in the composite where the zonal wind anomalies ($\delta u_g = U_g - u_g$, where U_g, is the seasonal cycle) are statistically significant at the 95% level. The COLs included in this composite calculation have a 48 hour duration. The composites are plotted from (a) t = -36 hours to (l) t = +30 hours, plotted in 6-hour intervals.*

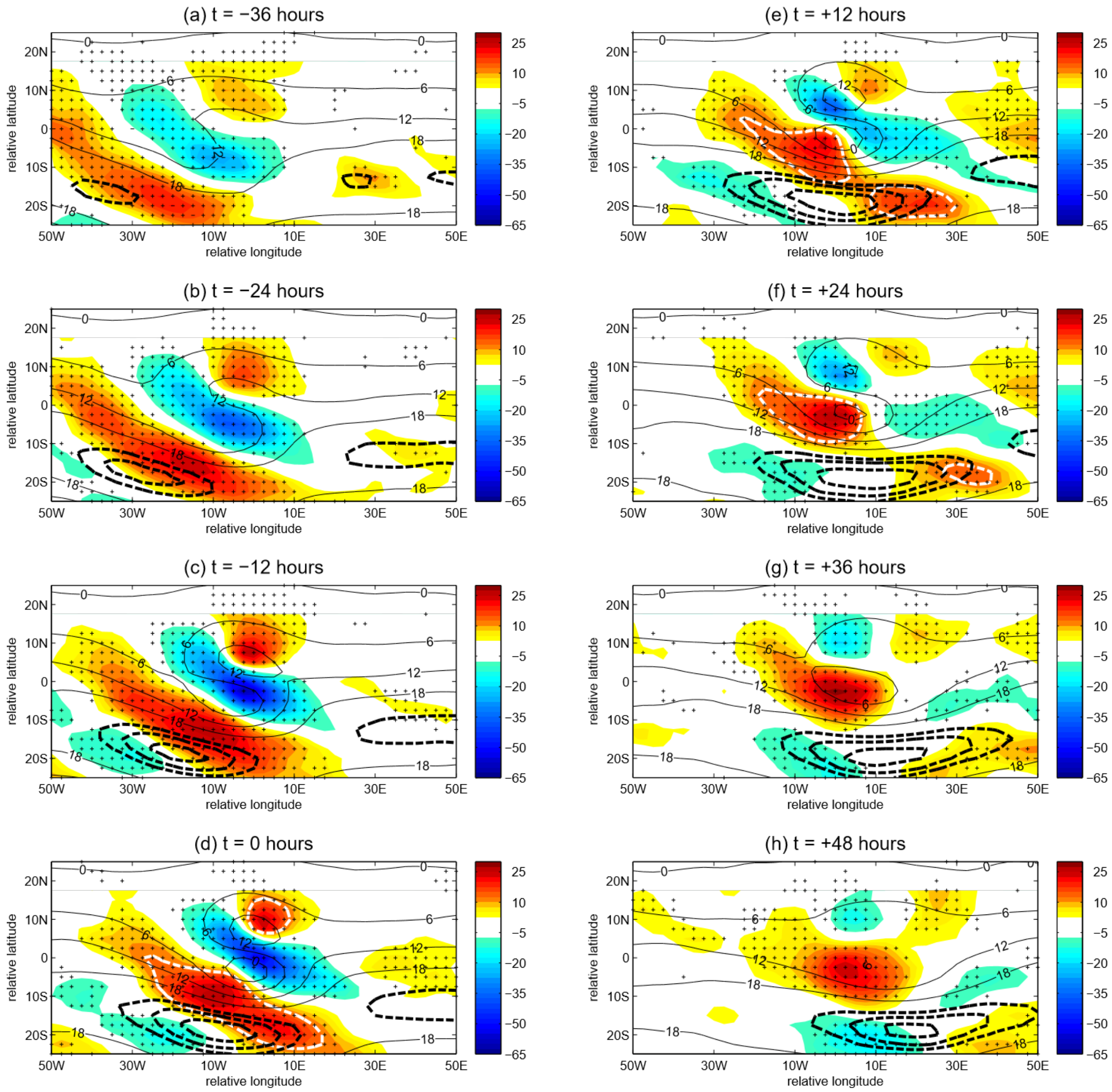

Figure 4.5: *Time-lagged composites of 500 hPa $\partial_t u_g$ (shaded), plotted in 10^6 m s^{-2}, the thin back contours are as in Figure 4.4. The white thick dashed contours represent $\partial_t u_g = 12.5 \times 10^6 m\ s^2$. The crosses represent areas where $\partial_t u_g$ is statistically significant at the 95% level. The composites are plotted from (a) t = -36 hours to (l) t = +30 hours, in 12 hour intervals.*

In the following two sections we discuss the various dynamical processes that are involved in informing the evolution of the zonal flow. In all the figures, the 95% level statistical significance of the composite fields is represented by the areas with crosses. It was calculated using Brown and Hall (1999).

4.3 Dynamical analysis

4.3.1 The evolution zonal flow

Ndarana and Waugh (2010) as well as Reyers and Shao (2019) discussed the evolution of the zonal isotachs that are associated with COLs. We repeat that analysis in this project, but using the geostrophic flow (as defined in Chapter 3) to show that the structures are similar. This will allow us to employ the quasi-geostrophic framework to diagnose the evolution of the jet streaks and explain the dynamics that underlie their evolution. The sequence of events (see Figure 4.4) begins with a weak jet streak, located southwest of the composite COL position. The jet streak increases in strength, likely because of an increasing low level meridional temperature gradient, as it propagates eastward. Note that its axis has a north-west/south-east orientation. As the jet streak increases in strength, whilst propagating east, the barotropic shear associated with it increases too, which in turn deforms the potential vorticity contours, so that the lower stratospheric air is transported isentropically in an anticlockwise fashion, signalling RWB. By the time the jet passes the composite COL position, and south of the position, the high PV air is pinched off, thus forming a high PV anomaly, which induces the cyclonic circulation (Hoskins et al., 1985) that characterises COLS. Note that the behaviour of the jet streak in the Southern Hemisphere is different from Northern Hemisphere, in that, the jet streak in the latter is found at the base of a trough (see Lang and Martin (2012), and it is found at the base of a ridge in the Southern Hemisphere. This will have important implication for the energy transfer that is to follow.

The wave breaking structure that occurs as a result of the above appears to be equatorward (and was shown in Ndarana and Waugh (2010) to be anticyclonic using wave activity diagnostics). Similar behaviour has been observed in idealised simulations (Thorncroft et al., 1993; Kunz et al., 2009; Wang and Polvani, 2011; Kunkel et al., 2016), where it was classified as Life Cycle 1(LC1). LC1 is of four categories of RWB and the others are LC2 which is cyclonic and equatorward. Peters and Waugh (1996) found poleward counterparts of these and called them P1 and P2. The causality between RWB and COL is still an open question. Be that as it may, it is clear from the composites that PV overturning precedes COL formation. This is a must of course because the high PV anomaly that induces the COLs can only be pinched off after the PV gradient has been reversed, as it has been shown in the idealised simulations highlighted above.

Clearly, changes in the zonal flow u_g induce an Eulerian acceleration field ($\partial_t u_g$). To calculate the latter, the zonal velocity fields at t = -6 hours and t = +6 hours is used. Composite of these fields, with the jet streak highlighted by means of the thick dashed contours, are shown in Figure 4.5. There is increasing deceleration in the region of COL formation, thus leading to the split structure that COLs are well known for in the Southern Hemisphere (Ndarana and Waugh, 2010, Reyers and Shao, 2019; Pinheiro et al., 2020). The midlatitude jet is characterised by $\partial_t u_g > 0$ in the anticyclonic divergence flow. This field indicates that the jet streaks move eastward very rapidly before the formation of the COL, it then propagates less rapidly, once the COLs have formed. As the midlatitude jet passes south of the closed circulation, the $\partial_t u_g > 0$ splits into two structures, with the one upstream propagating into the closed circulation and the other remaining in the jet exit (as highlighted by thick dashed white contour). The increasing strength of deceleration in the area of the closed circulation also changes to acceleration, thus signalling the dissipation of the split jet structure.

As noted previously, the use of u_g instead of u, and the similarity between these (compare with Ndarana and Waugh, 2010 and Reyers and Shao, 2019) allow the diagnosis of the evolution of the flow using the quasi-geostrophic framework. The question that is raised at this point what are the processes that inform $\partial_t u_g$. The proposition made here is that the COL ambient flow changes are induced by the redistribution of zonal momentum and so one approach that may be considered to understand the evolution of u_g and therefore $\partial_t u_g$ is the quasi-geostrophic zonal momentum equation, which is given by

$$\partial_t u_g = -\mathbf{V}_p \cdot \nabla_p u_g + (f_o + \beta y)(v_g + v_a) - \partial_x \Phi \tag{4.4}$$

In the midlatitudes, the contours in the geopotential field are almost zonal and therefore $\partial_x \Phi \sim 0$, and $f_o v$ is the torque that serves to change the direction of the flow. It is also an apparent force. The most important term in this analysis is therefore the advection of zonal momentum (i.e. $-\mathbf{V}_p \cdot \nabla_p u_g$) and its components $-u_g \partial_x u_g$ and $-v_g \partial_y u_g$. These fields are presented in left and right panels in Figures 4.6, respectively, with $-\mathbf{V}_p \cdot \nabla_p u_g = --6(+6) \times 10^6 \text{m}^2\text{s}^{-2}$ represented by the thick dashed red (blue) contours superimposed on them. Given the well-known structure of jet streaks (see Figure 4.3), $\partial_x u_g > 0$ in the confluent flow and $\partial_x u_g < 0$ in the diffluent flow and since $u_g > 0$ everywhere in the jet, we expected that the advection of zonal momentum by the zonal flow will negative at the jet entrance and positive at the exit. Note that there is a spatial agreement between the $\partial_t u_g$ (Figure 4.4) and $-u_g \partial_x u_g$ (Figure 4.5) fields more than any other field and so the former is influenced by these advective processes. The function of $\partial_x u_g$ is to advect momentum, thus redistributing it, from the jet entrance to the exit end of the jet, thus propelling it eastward. This occurs on the cyclonic side of the jet.

The jet also changes its north-west/south-east orientation prior to reaching south of the closed COL circulation, to become more zonal as it passes it and then slightly southwestern/northeastern beyond the closed circulation. We propose that $-v_g \partial_y u_g$ is responsible for this. The middle panels in Figure 4.5 show poleward (equatorward) meridional flow at the jet entrance (exit), and since $\partial_y u_g < 0$ ($\partial_y u_g > 0$) on the anticyclonic (cyclonic) side of the jet, we end up with the patterns that are shown in right panels of Figure 4.6. This means that the thermally direct circulation (see Figure 4.3. (a)) at the jet entrance advects zonal momentum in the poleward direction. The indirect circulation advects momentum equatorward. The combined impact of this seesaw effect on the jet is a change in its orientation.

Figure 4.3 (b) suggests that there are vorticity related processes at play in jet streak dynamics. The way to link these to the Eulerian acceleration of the jet is producing the u_g tendency equations, which is obtained by multiplying the geopotential tendency equation by $-g/f_o$ and then differentiating with respect to y (Dong and Colucci, 2015).

$$\left[\nabla_p^2 + f_o^2 \partial_p(\sigma^{-1}\partial_p)\right] \partial_t u_g = \partial_y \left[\mathbf{V}_p \cdot \nabla_p \eta\right] + f_o g \partial_y \left\{\partial_p \left[\sigma^{-1} \mathbf{V}_g \nabla_p (\partial_p z)\right]\right\} \tag{4.5}$$

where $\eta = \zeta_g + f$ and the rest of the symbols have been defined above. This equation can be used qualitatively by recalling that $\left[\nabla_p^2 + f_o^2 \partial_p(\sigma^{-1}\partial_p)\right] \partial_t u_g \propto \partial_t u_g$ (Holton and Hakim, 2014; Dong and Colucci, 2015), to infer the roles that different processes play in changing the zonal flow that is associated with COLs. It follows then that in particular that $\partial_t u_g \propto \partial_y [-\mathbf{V}_p \cdot \nabla_p \eta]$. Figure 4.7 shows the vorticity advection pattern. There is positive vorticity advection (PVA) to the west of the trough axis and negative vorticity advection (NVA) to the east of it. This, of course, is the well-known pattern that propagates baroclinic wave eastward, if the relative vorticity advection is more dominant than planetary vorticity advection (Holton and Hakim, 2014). The PVA is also located on the anticyclonic side of the confluent flow, as shown schematically in Figure 4.3 (b), and of course, there is a large NVA structure on the cyclonic side of the jet entrance. However, this vorticity advection patterns simply does not match that of $\partial_t u_g$. It is when the meridional divergence of the vorticity advection field is taken that a pattern that matches the Eulerian acceleration emerges.

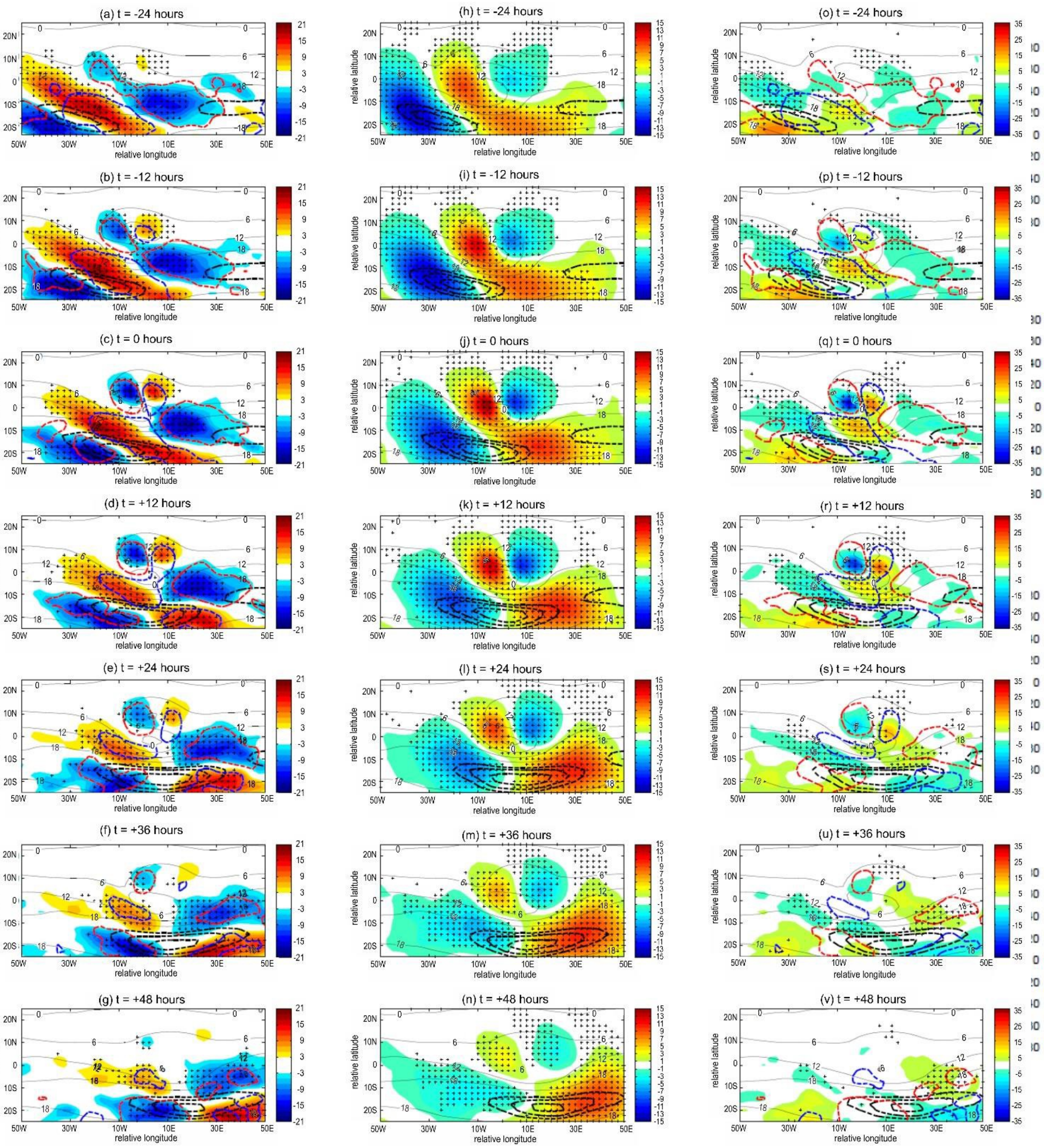

Figure 4.6: *Time-lagged composites of 500 hPa* $-u_g\partial_x u_g$ *(left panels),* v_g *(middle panels) and* $-v_g\partial_y u_g$ *(right panels) plotted in* 10^6 m^2 s^{-2}*. The red (blues) thick dashed contours in the left and right panels represent* $-\mathbf{V}_g \cdot \nabla_p u_g = -6\ (+6) \times 10^6\ m^2\ s^{-2}$*. The black contours are the same as in Figure 4.4. The crosses represent areas where the fields are significant at the 95% significance level. The composites are plotted from (a) t = -24 hours to (g) t = +48 hours, in 12 hour intervals.*

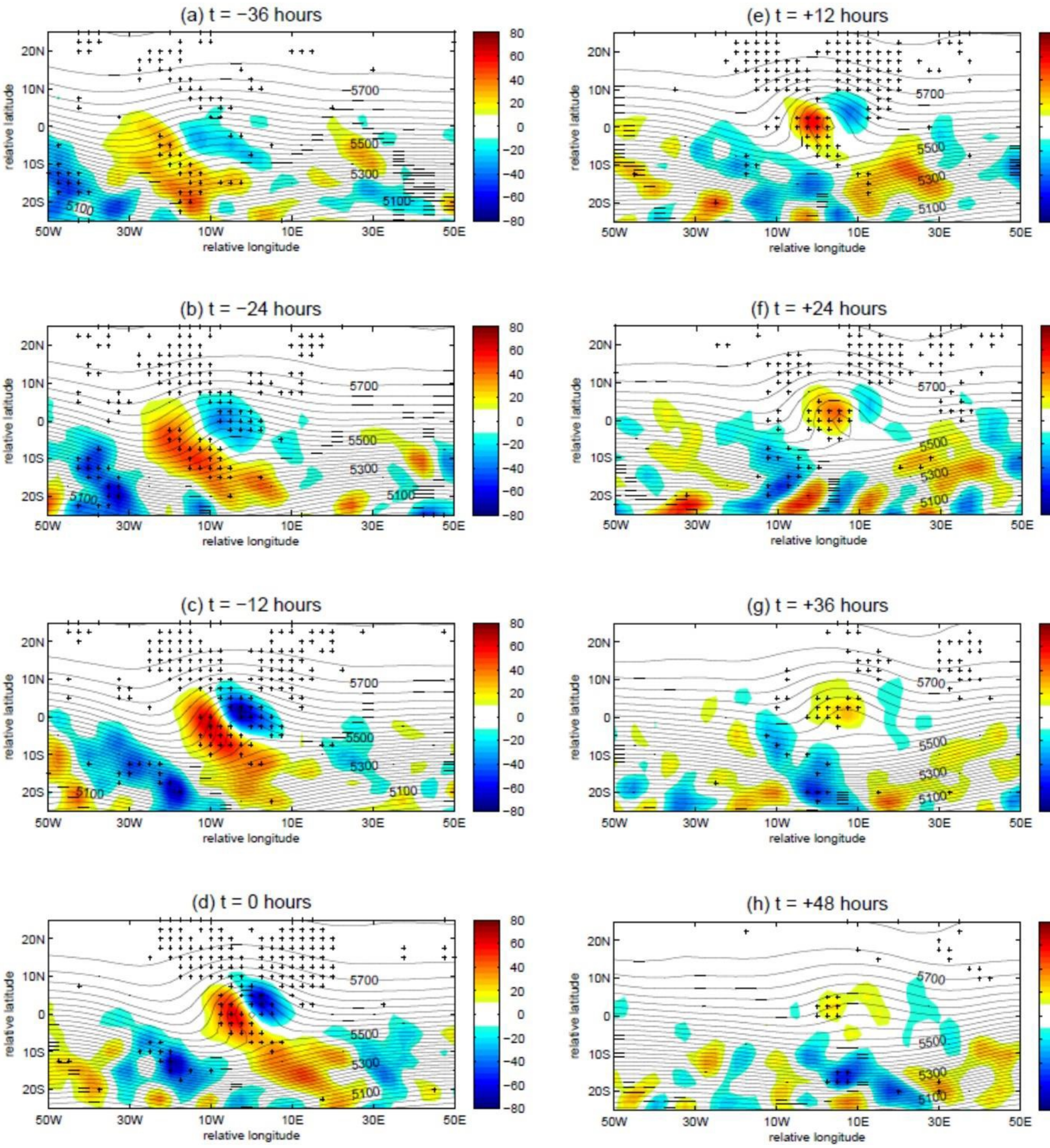

Figure 4.7: *Time-lagged composites of 500 hPa geopotential heights (black contours), and absolute vorticity advection,* $-\mathbf{V}_g \cdot \nabla_p(\zeta_g + f)$*, shaded and plotted in* $10^{11}\ s^{-2}$*. The crosses represent areas where* $-\mathbf{V}_g \cdot \nabla_p(\zeta_g + f)$ *is statistically significant at the 95% significance level. The composites are plotted from (a) t = -36 hours to (h) t = +30 hours, in 12 hour intervals.*

In the vicinity of the COL closed circulation, vorticity advection attains maximum and minimum values at the inflection points of the geopotential heights, where $\partial_x^2 z = 0$, after having increased from the ridge axis and then decreasing towards the trough axis, change sign beyond that point to reach minimum values between the axis of the COL and the eastern ridge. What this means is that between the two axes that lie on either side of the COL trough axis $\partial_y [-\mathbf{V}_p \cdot \nabla_p \eta] < 0$ (i.e. vorticity advection convergence -

VAC) and therefore $\partial_t u_g < 0$ also. The co-locations of VAC and the deceleration of the zonal flow is highlighted by the blue shaded region and the thick dashed red contour ($\partial_t u_g = -15 \times 10$ m s−2. Therefore VAC contributes to the development of the split jet. In fact, it explains the portion of $\partial_t u_g$ that $-u_g \partial_x u_g$ does not explain in the closed COL circulation region. The $\partial_t u_g > 0$ field that lies between the jet axis and the western inflection point of the COLs is explained by the fact that this is a vorticity advection

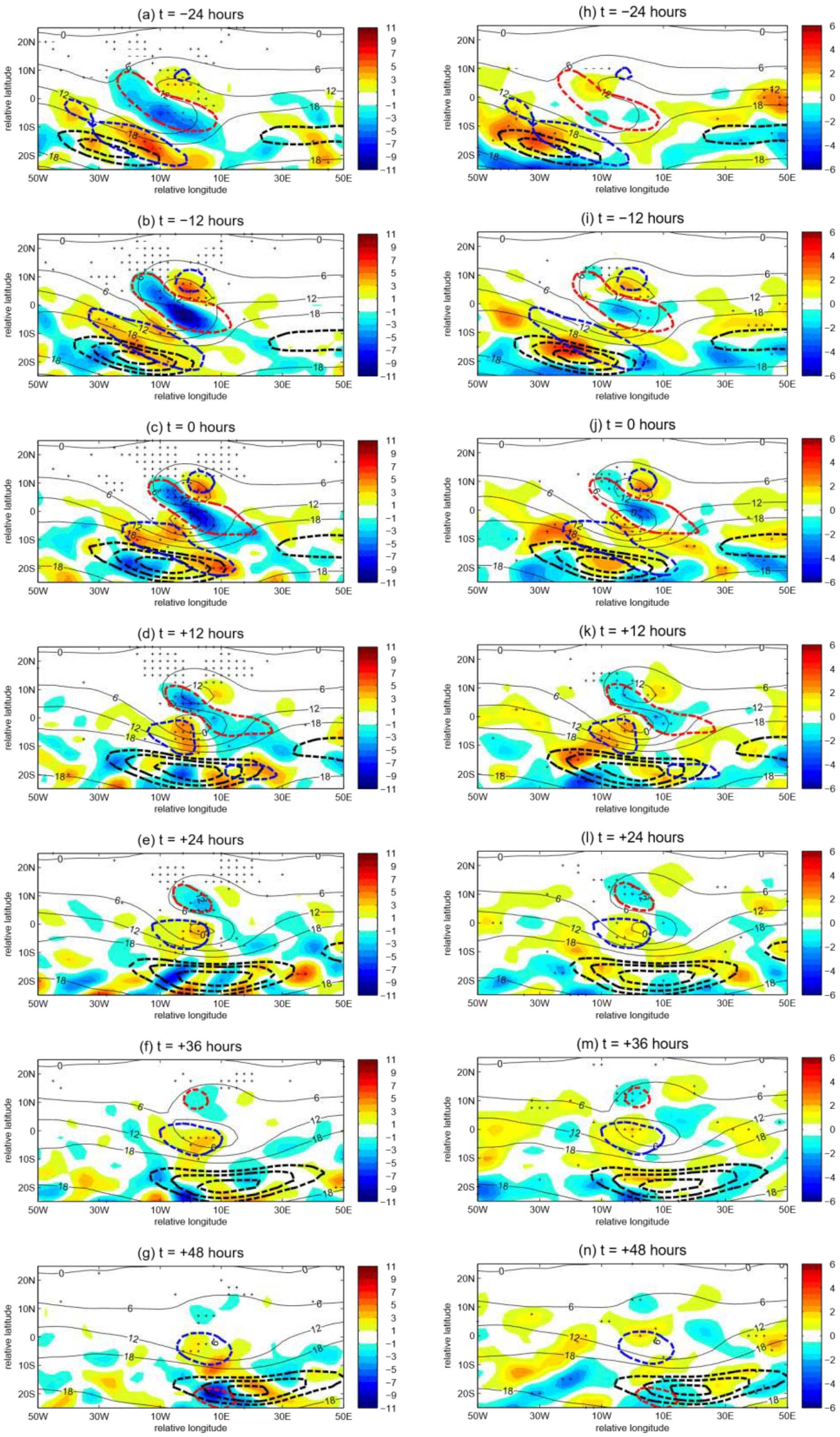

Figure 4.8: *Time-lagged composites of 500 hPa vorticity advection divergence (left panels) and temperature advection divergence (right panels), both plotted in $10^6\ m^{-1}\ s^{-2}$. The black contours are the same as in Figure 4.4. The crosses represent areas where the advection fields are significant at the 95% significance level. The composites are plotted from (a,h) t = -24 hours to (g,n) t = +48 hours, in 12 hour intervals.*

source (i.e. vorticity advection divergence – VAD). In the midlatitudes, it appears as though the VAC and VAD assist the $-u_g\partial_x u_g$ in propelling the jet eastward until the COLs form. Beyond that point the patterns change such that there are alternating VAC and VAD fields (instead of VAC and VAD being located at the jet entrance and exit, respectively). This suggests that the impacts may be too microscopic or localised to have the translational effect that $-u_g\partial_x u_g$ has on the jet (see Figure 4.6).

4.3.2 Eddy available potential energy and eddy kinetic energy during COL evolution

Understanding the dynamics associated with the jet streaks, as discussed in the previous subsection, is an important step towards understanding the evolution of the energy that is associated with COLs. In this subsection we discuss the eddy available potential energy and eddy kinetic energy budgets to understand the dynamics that precede COLs, as would be required for predictability studies. Equation 4.1 describes the rate of change of eddy kinetic energy (K_e), the presence of which according to classic energetics theory (Lorenz, 1955) comes from an energy cycle that begins by generating mean available potential energy (P_m) from diabatic processes. P_m is converted to eddy available potential energy (P_e); analysis in this project begins with the latter.

To analyse the energetics of individual weather systems, energetics fields that evolve in both space and time need to be generated and this is done by defining a 31-day time mean basic state flow (Orlanski and Katzfey, 1991; Lackmann et al., 1999; Danielson et al., 2006) centred on the day of the COL events and perturbations are deviations from that time mean. The total variables are then decomposed as follows:

$$\mathbf{U} = \mathbf{U}_m + \mathbf{u} \tag{4.6}$$

$$\mathbf{V} = \mathbf{V}_m + \mathbf{v} \tag{4.7}$$

$$\mathbf{\Phi} = \mathbf{\Phi}_m + \varphi \tag{4.8}$$

$$\mathbf{\Theta} = \mathbf{\Theta}_m + \theta \tag{4.9}$$

where the capital letters/Greek with no subscript m and with the subscript m represent the total and time mean variables, respectively. The lowercase symbols represent the perturbation fields and $\mathbf{U} = U\mathbf{i}+V\mathbf{j}+\omega\mathbf{k}$ where the hat over Θ represents the horizontal average. We employ the flux form of the Orlanski and Katzfey (1991) and Danielson et al. (2006) eddy available potential energy (P_e) equation given by

$$\partial_t P_e = -\nabla_p \cdot (\mathbf{V}P_e) - \partial_p(\omega P_e) + \omega\alpha + \frac{\alpha_m}{2\Theta_m}\frac{1}{d\widehat{\Theta}/dp}(\mathbf{v}\theta \cdot \nabla_p\Theta_m) + S \tag{4.10}$$

where α is the specific volume and the other terms have been defined above. The subscript p in the gradient operator means that it is evaluated whilst keeping pressure constant. At this point we re-write Equations (4.1) and (4.2) combined for convenience (as it should be read and interpreted in conjunction with Equation (4.11)

$$\partial_t K_e = -\nabla_p \cdot (\mathbf{V}K_e) - \partial_p(\omega K_e) - \omega\alpha - \nabla_p \cdot (\mathbf{v}\varphi)_a - \partial_p(\omega\varphi) + [\mathbf{v} \cdot (\mathbf{u} \cdot \nabla)\mathbf{V}_m] + \mathrm{R} \tag{4.11}$$

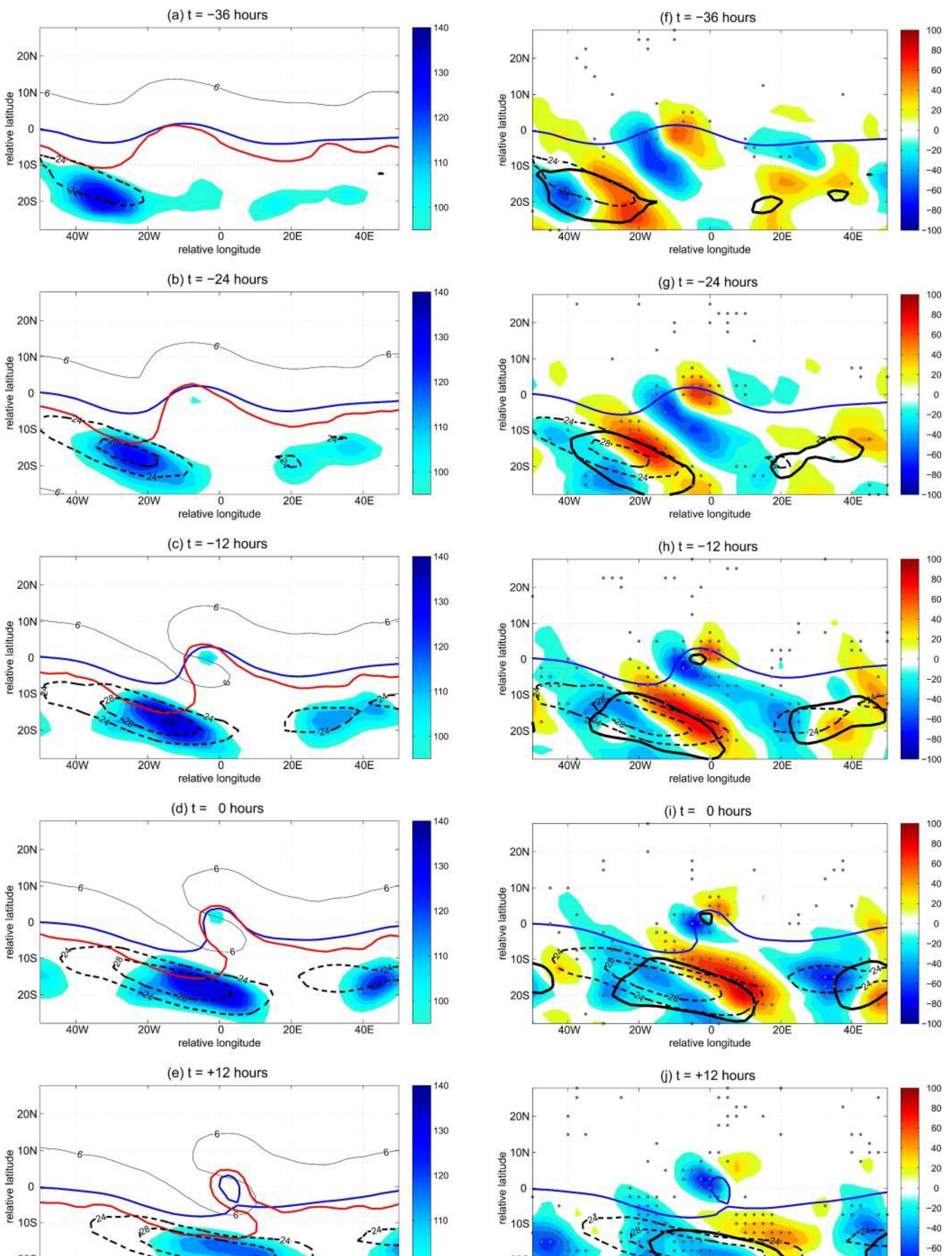

Figure 4.9: *Time-lagged composites of vertically integrated eddy available potential energy (shaded in blue) shown on the left panels. The eddy available potential energy is plotted from 95-140 m² s⁻². The thick red contour is the -2 PVU contour on the 330 K isentropic surface. The right panels show time-lagged composites of the tendency of vertically averaged eddy available potential energy(shaded) plotted in m² s⁻² day⁻¹. In all panels, the thick blue contour is the 5614 gpm geopotential height. The thin black contour is the 6 m s⁻¹ zonal isotach and the thick dashed black contours are the24 and 28 m s⁻¹ zonal isotachs, to highlight the location of the jet streak. The thick black solid contourin the right panels is the 100 m² s⁻² contour of eddy available potential energy and the grey dots represent areas where the tendency of the eddy available potential energy is significant at the 90% level. The composites are plotted in 12 hour intervals from (a,f) t = -36 hours to (e,j) t = +12 hours.*

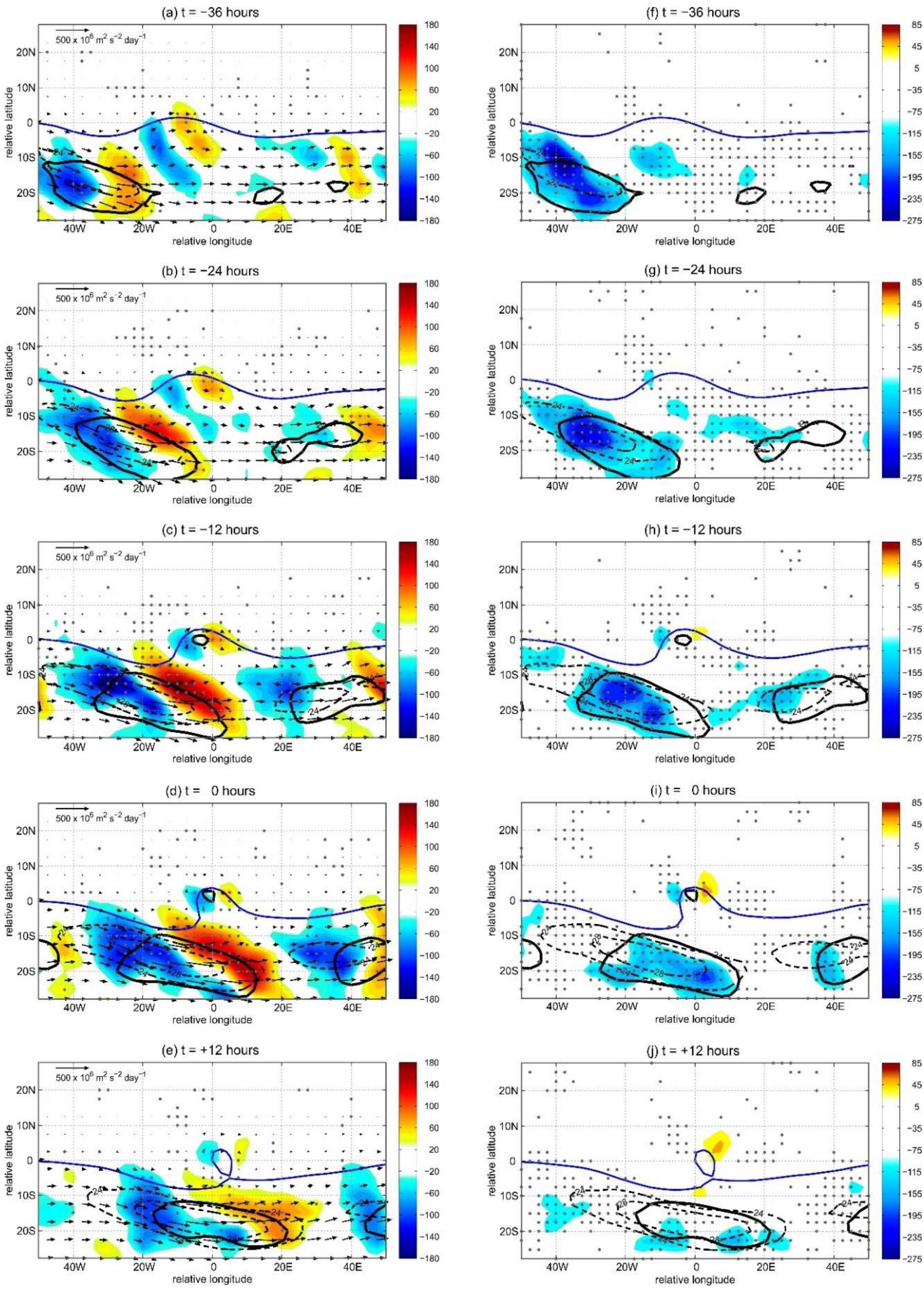

Figure 4.10: *Time-lagged composites of eddy available potential energy fluxes $\boldsymbol{V}P_e$ (arrows) and their divergence ($-\nabla\cdot(\boldsymbol{V}P_e)$, shaded) in left panels and baroclinic conversion (ωα) shaded in the right panels, both plotted in $m^2\,s^{-2}\,day^{-1}$. The blue contours, thin and thick dashed black contours and thick slid black contour and evolution time steps as in Figure 4.9.*

The first two terms on the right hand side of Equations (4.11) and (4.12) are the horizontal and vertical eddy available potential energy and eddy kinetic energy flux convergence terms, the third terms is the baroclinic conversion of P_e to K_e (as they are equal and have opposite signs). The fourth term in Equation (4.11) represents the conversion from mean available potential energy (P_m) to P_e. The mathematical form of P_m is the same as that of P_e in Equation 4.10, expect that the perturbation potential temperature, θ, is replaced by Θ_m−hΘ_mi, where h·i represents the global average, as in Murakami (2011). The sixth term in Equation 4.11 is the conversion from K_e to K_m. All the terms, as presented below, are integrated in the vertical and as a result all the vertical convergence terms (i.e. ∂_ph·i) are small.

Before the inception of this project, the last paper to employ dynamic meteorology concepts in understanding processes in the South African domain was Tennant and Reason (2005). In their study, the association between the global energy cycle and South African rainfall was established and they employed a different framework from the one discussed above. Following Wiin-Nielson (1962), Tennant and Reason (2005) decomposed kinetic energy into barotropic and baroclinic components, defined as $K_{BT} = \mathbf{V}_{BT}\cdot\mathbf{V}_{BT}\times 0.5$ and $K_{BC} = \mathbf{v}_{BC}\cdot\mathbf{v}_{BC}\times 0.5$, respectively. $\mathbf{V}_{BT}$ is the vertically integrated horizontal flow and $\mathbf{v}_{BC} = \mathbf{V} - \mathbf{V}_{BT}$. By considering this framework, we will be in a position to link the behaviour of the COL energetics to the Tennant and Reason (2005) result. All the results shown below are pressure-weighted vertical average of the diagnostics.

As shown in the previous section, the jet streak (black thick dashed contours) shown, again, in the left panels of Figure 4.9 is propelled eastward mainly by means of the zonal flow redistributing zonal momentum from the jet entrance to the exit. The jet streak propagates with P_e, whilst the latter is located from the centre to the jet exit. The P_e increases from the point that the jet streak develops and reaches a maximum on the day of the COL formation, after which it dissipates. The patterns of $\partial_t P_e$ shown in the right panels of Figure 4.9 show that the cyclonic confluent flow side of the jet is a P_e sink, whilst its source is located at the jet exit, north of the jet axis. The pattern of the terms

$$-\nabla\cdot(\mathbf{V}P_e) + \frac{\alpha_m}{2\Theta_m}\frac{1}{d\widehat{\Theta}/dp}(\mathbf{v}\theta\cdot\nabla_p\Theta_m) \tag{4.12}$$

are similar in structure to only $-\nabla\cdot(\mathbf{V}P_e)$, which is shown in Figure 4.10 (left panels), thus showing that the increase of P_e at the jet exit is caused by energy flux convergence and conversion from P_m, as indicated by the second term in Equation 4.12. Baroclinic conversion $\omega\alpha < 0$ from P_e to K_e occurs over the western flank of the jet streak, where there is energy flux divergence (which is negative when multiplied by -1), so a comparison of the right panels Figure 4.9 and the right panels of Figure 4.10 P_e suggests that P_e is lost there. It follows then that the negative rate of change of P_e west of the jet centre, P_e decreases as a function to time by conversion to K_e and by transporting potential energy to the front end of the jet streak.

We now turn our attention to the evolution of K_e presented in Figure 4.11. Figure 4.9 shows that P_e is confined to the midlatitude towards the jet exit, this stands to reason because this energy form is defined in terms of perturbation potential temperature, which would be a maximum where the temperature gradient is the largest. So the first difference between the P_e and K_e structures is that, whilst the latter is also found in the midlatitudes, its location is upstream that of P_e, closer to the jet entrance. This makes physical sense when one thinks about the fact that it is the P_e that must be converted to K_e and so the latter should be located upstream. The second difference between the structures of the two energy forms is that in the case of K_e there exists a second centre that develops outside the jet streaks. It is located at the inflection point of the evolving wave between the ridge and trough axes, which can clearly be seen if one pays attention to the positions of the K_e centres, relative to the potential vorticity contour (i.e. the thick red contour representing PV = -2 PVU) or even the geopotential contour represented by the thick blue contour. Curiously, similar behaviour of the Tennant and Reason (2005) kinetic energy is observed with the difference that the second K_e is located north of the COL trough axis, precisely where the smaller scale jet streaks from discussion in Subsection 4.3.1 is located. Regardless of these differences, both forms of kinetic energy behave in a way that is expected, because they are similar to the schematic representations of the K_e in a baroclinic wave shown in Figures 4.1 and 4.2.

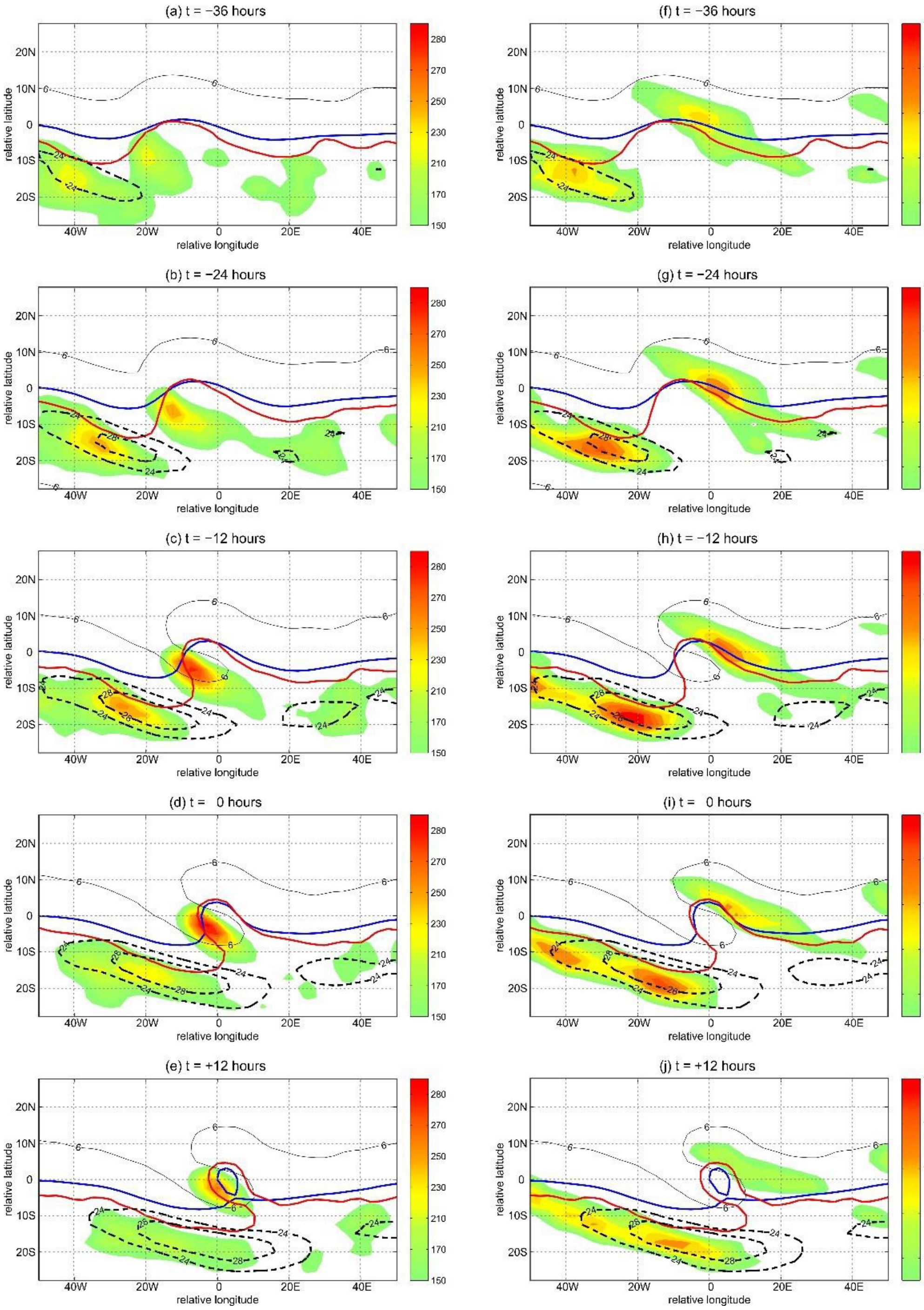

Figure 4.11: *Time-lagged composites of $\partial_t K_e$ (shading on the left panels) and $-\nabla \cdot (\mathbf{V}K_e)$ (shading on the right panels) and flux vectors $\mathbf{V}K_e$. The K_e tendency and the flux divergence are plotted in $m^2\ s^{-2}\ day^{-1}$. The thick solid black contour is the 170 $m^2\ s^{-2}$. The blue contours, thin and thick dashed black contours and evolution time steps as in Figure 4.9.*

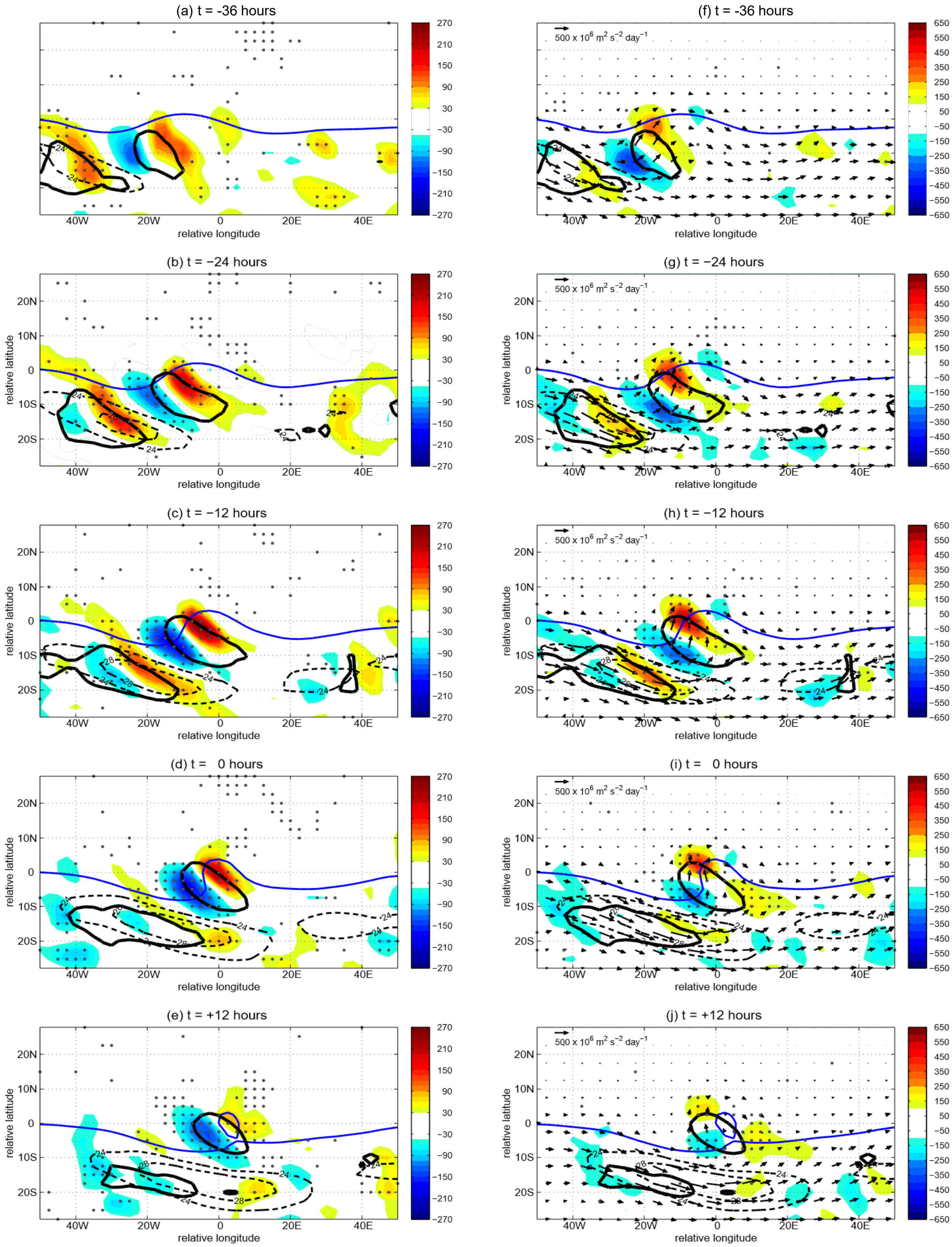

Figure 4.12: *Time-lagged composites of $\partial_t K_e$ (shading on the left panels) and $-\nabla \cdot (\mathbf{V}K_e)$ (shading on the right panels) and flux vectors $\mathbf{V}K_e$. The K_e tendency and the flux divergence are plotted in m^2 s^{-2} day^{-1}. The thick solid black contour is the 170 m^2 s^{-2}. The blue contours, thin and thick dashed black contours and evolution time steps as in Figure 4.9.*

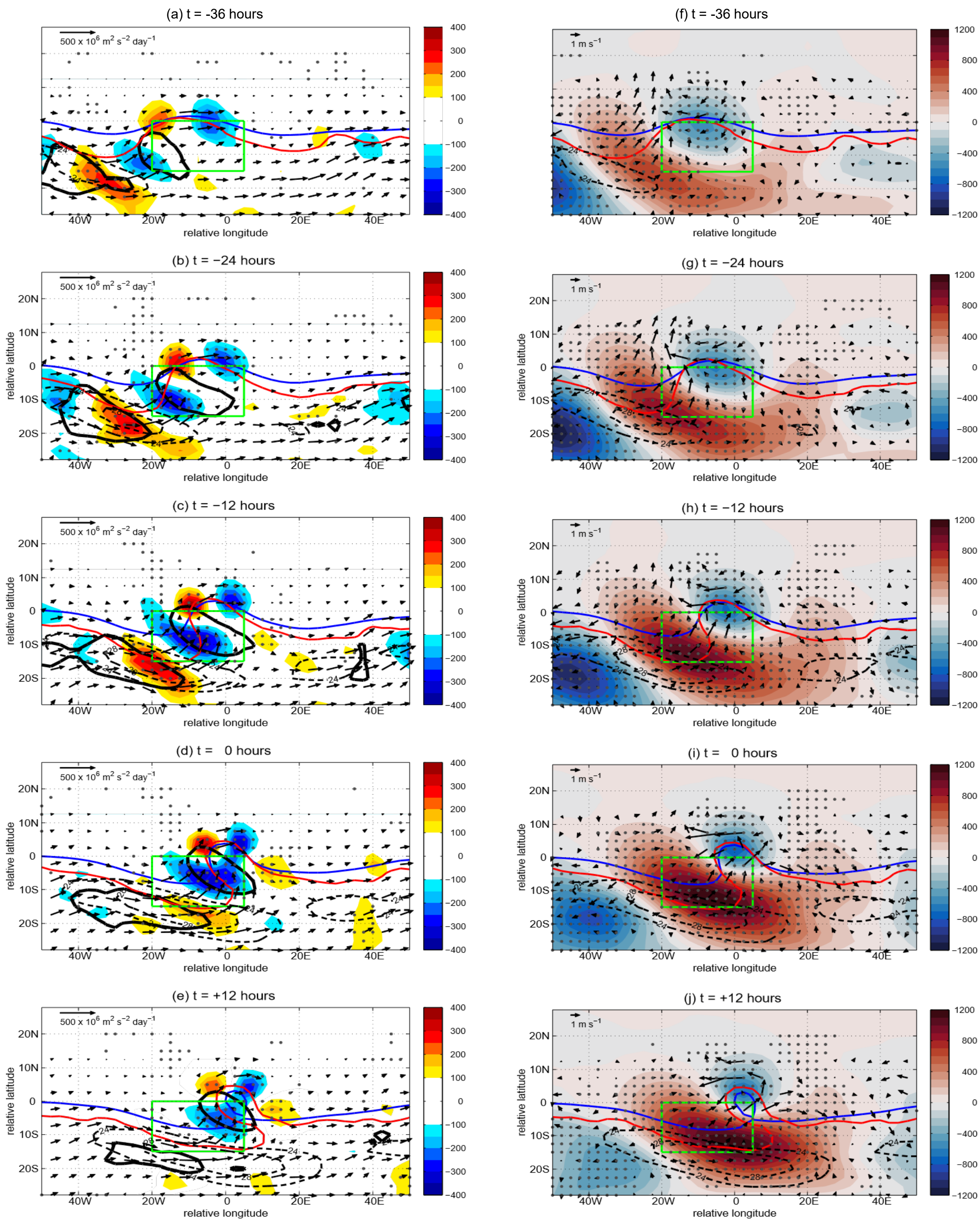

Figure 4.13: *Time-lagged composites of* $\nabla \cdot \mathbf{v_a}\varphi$ *(shading on the left panels) and the arrows represent the ageostrophic geopotential flux* $\mathbf{v_a}\varphi = (\mathbf{v} - f^{-1}\mathbf{k} \times \nabla\varphi)\varphi$*. The shading in the right panels represent* φ *and the arrows represent the ageostrophic flow* $\mathbf{v}_a = u_a\mathbf{i} + v_a\mathbf{j}$*. The thick slid black contour is the 170* $m^2 s^{-2}$*. The blue contours, thin and thick dashed black contours, and thick red contour and evolution time steps as in Figure 4.09. The green box represents the region bounded by 20°W - 50° relative longitude and 0° - 15°S relative latitude to highlight where* $\mathbf{v_a}\varphi$ *is most dominant.*

The left panels of Figure 4.12 show $\partial_t E_e$, which is the left hand side of Equation 4.11. The presence of the second K_e (unlike the P_e), patterns of $\partial_t K_e$ exhibit behaviour that mimics geopotential height or meridional wind anomalies structure in evolving baroclinic waves, as seen in Figure 2.10, for instance. There are several issues involved here. Firstly, the positive $\partial_t E_e$ located in the jet streak is contributed to by $\omega\alpha < 0$ (right panels of Figure 4.10 and third term on the right hand side of Equation 4.12), that is, P_e is converted into K_e. This shows that for COLs in the South African domain, baroclinic conversion is a midlatitude process. It partly informs the presence of the upstream positive and negative local rate of change of K_e pattern. Secondly, This upstream pattern has strong fluxes and their divergence (upstream) and convergence (downstream). Thus the upstream $\partial_t K_e$ structure is also informed by the first term on the right hand side of Equation 4.11. Note that the fluxes are strongest with the jet because the zonal flow is strongest there. The second $\partial_t K_e$ has no $\omega\alpha$ associated with it and therefore it is caused exclusively by $-\nabla \cdot (\mathbf{V}K_e)$, which is supported by the left panels of Figure 4.12.

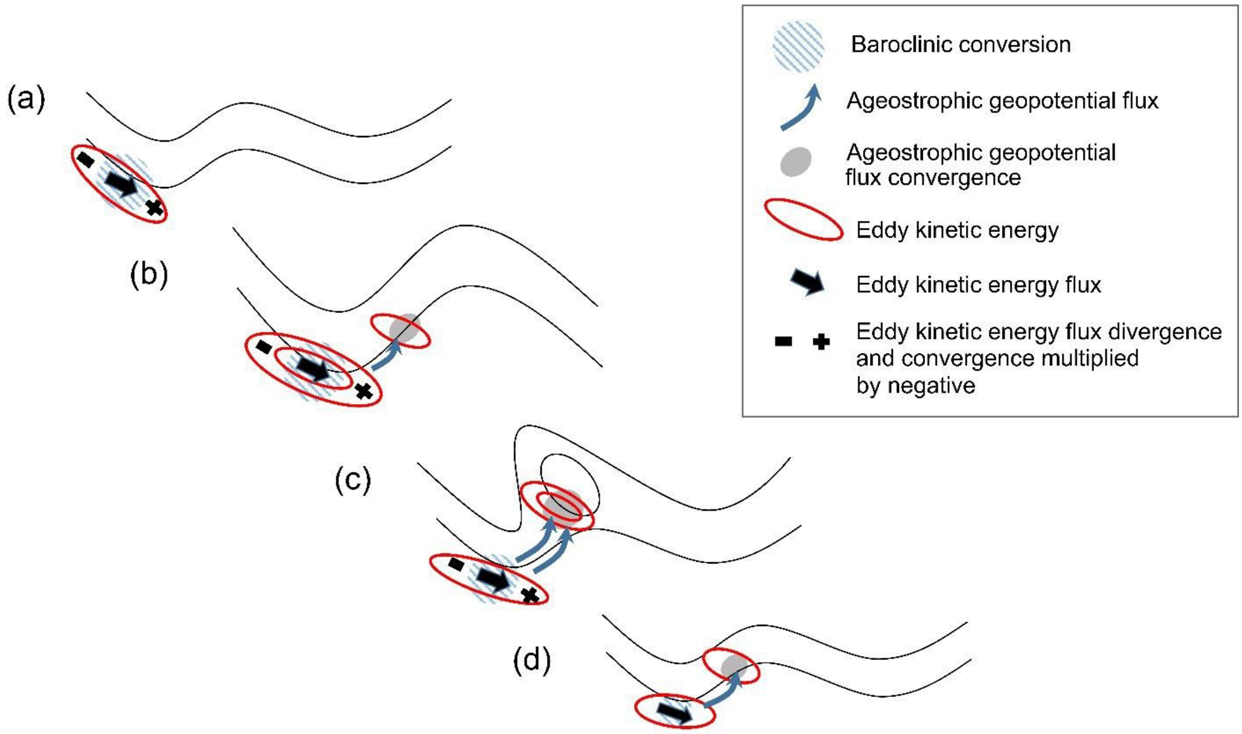

Figure 4.14: *Schematic representation of evolving eddy kinetic energy centres relative to COL formation. The eddy kinetic energy centres are represented by the red oval shapes, in which the number of concentric oval shaped contours represents the strength of the energy. The thick black arrows represent eddy kinetic energy flux, with its divergence and convergence in the rear and front ends of the upstream centres, respectively. The striped regions in blue are the baroclinic conversion from eddy available potential energy to eddy kinetic energy and the grey area found in the downstream, smaller scale eddy kinetic energy centre represents the ageostrophic geopotential flux convergence and the fluxes are the curved thick blue arrows. The thin black wavy curves represent upper level geopotential height fields, with the closed cyclonic circulation forming at (c), as the upstream eddy kinetic centre reaches maximum values. The panels represent the different stages of downstream development – (a) Stage 1: Development of upstream eddy kinetic energy from baroclinic conversion. (b) Stage 2: Maturation of the upstream eddy kinetic energy centre and growth of the downstream centre by means of ageostrophic geopotential fluxes. (c) Stage 3: Dissipation of upstream eddy kinetic energy centre and maturation of downstream centre on the day of the formation of the cut-off low closed circulation. (d) Beyond Stage 3: The dissipation of both energy centres.*

4.3.3 Downstream development during the evolution of COLs

Given the fact that $\partial_p(\omega K_e)$ and $\partial_p(\omega\varphi)$ are small, when the terms are integrated in the vertical, and also given the fact that $[\mathbf{v}\cdot(\mathbf{u}\cdot\nabla)\mathbf{V}_m]$ is the barotropic conversion from K_e to K_m, which does not have anything to do with the development of troughs, the term that remains to be discussed is $-\nabla_p\cdot(\mathbf{v}\varphi)_a$. These terms will be discussed in the context of downstream development, as described in Section 4.1.

First, we note the differences between the idealised presentation in Figure 4.2 of Section 4.1 and the data presented in Figure 4.11. Downstream development in Section 4.1 (and in baroclinic waves in general) occurs between K_e centres that are separated by the trough axis. Here it occurs between centres that are separated by the ridge axis. We call the centre that is co-located with the jet streak, the "K_e (upstream)" and the one located at the inflection point "K_e (downstream)". During the time steps leading up to the formation of the COL, the K_e (upstream) increases and reaches a maximum value just before the COL forms. K_e (downstream) also increases in strength but reaches a maximum on the day of the formation of the COL and dissipates. As shown in the previous section, the growth of K_e (upstream) is caused by baroclinic conversion ($-\omega\alpha$ in Equation 4.11). The growth of K_e (downstream) appears to come from $-\nabla_p\cdot(\mathbf{v}\varphi)_a > 0$, which is the convergence of energy flux, defined here as the ageostrophic geopotential flux ($(\mathbf{v}\varphi)_a$), that leaves the leading edge of K_e (upstream) centre as indicated by the pronounced arrows that follow the ridge in the left panels of Figure 4.13. In the schematic representation of this process in Figure 4.2, it would be the open white arrow located west of energy centre *W*. The direction of $\mathbf{v}\varphi)_a$ is informed by the fact that the flow in the ridge is supergeostrophic, as noted in Section 4.1 and that as the waves break (as indicated by the red PV contour) they cause $\varphi > 0$. It is therefore clear that wave breaking that Ndarana and Waugh (2010) suggest transports lower stratospheric air, also facilitates energy transport from the jet streak into the region of the closed COL circulation.

This state of dynamical affairs may then be summarised with the aid of a schematic diagram as follows

1. A few days before the formation of the closed COL circulation, the midlatitude jet streak first propagates in the south-eastward direction (by means of momentum advection processes – Section 4.3.1 and then more zonally, whilst gaining in strength. The jet streak propagates together with P_e in its diffluence regions and K_e further upstream in the confluence of the streak.
2. This midlatitude K_e centre grows by gaining energy from the P_e ahead of it by means of baroclinic conversion (as indicated by the blue striped areas in Figure 4.14), which continues up to the point when the closed COL circulation forms and appears to cease thereafter as the jet streak passes south of the COLs. The movement of the K_e is caused by energy fluxes by the total flow within the energy centre and they distribute the energy from the rear to the front end of the centre (represented by the thick black arrows, at the minus and plus signs in Figure 4.14). The strength and direction of the fluxes are influenced by the flow of the jet streak in the case of the midlatitude K_e centre.
3. The propagation of the jet streak and its increasing zonal flow, coupled with the smaller scale jet streak north of the COL region, constitute a split jet found in previous studies (Ndarana and Waugh, 2010; Reyers and Shao, 2019), which in turn, increases anticyclonic barotropic shear and shearing strain (Nakamura and Plumb, 1994) leading to anticyclonic RWB (Peters and Waugh, 2003), signalled by PV overturning. The wave breaking processes create a ridge southwest of the COL circulation but on the equatorward side, the jet and this ridge deepen as wave breaking evolves. As a result, the flow becomes increasingly supergeostrophic and the geopotential anomalies deepen, thus inducing ageostrophic geopotential fluxes (blue curves arrows in Figure 4.14), and with time, increasing their magnitude. The supergeostrophic flow that is associated

with the wave breaking is directed anticyclonically, which in turn informs the direction of the fluxes towards the COL regions because the geopotential perturbations are positive.

4. These ageostrophic geopotential fluxes are responsible for transferring energy from the upstream K_e to the one downstream. Thus the latter grows, not from baroclinic conversion, but from ageostrophic geopotential flux convergence. It then reaches a maximum at the point when the closed COL circulation forms (shown by the concentric red oval shapes in Figure 4.14 (c)).

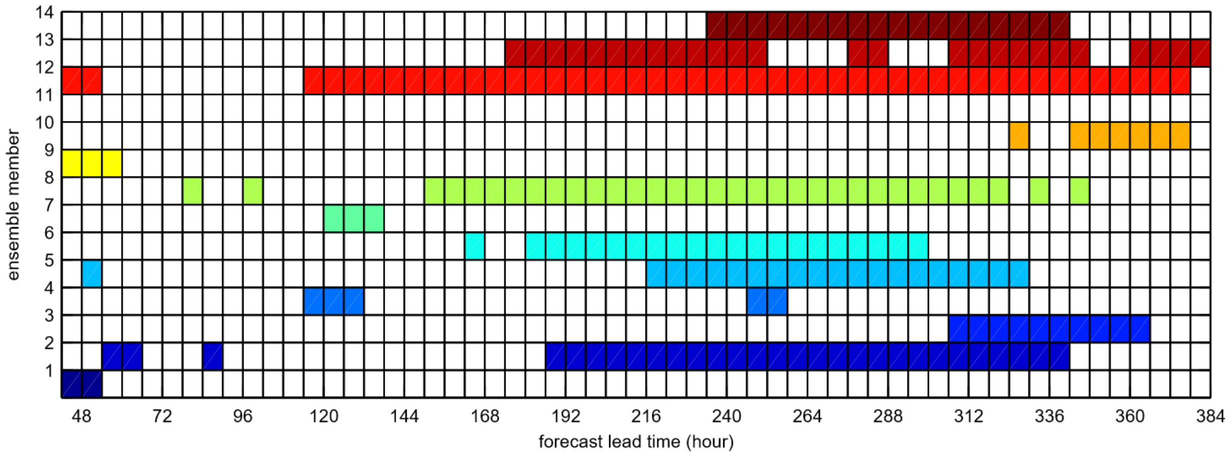

Figure 4.15: *Colour matrix representation of medium-range forecasts of the COL produced by the NCEP GEPS on the 00:00 UCT 14 April 2019 up to 384 ahead. The different colours in the scheme represent the forecasts of ridging highs by each ensemble member, with the ensemble mean at the top of the matrix. The white blocks represent hours for which no ridging high was predicted for this forecast window. The first (last) block with a colour represents the onset (cessation) of the ridging process as defined in the text. The total number of blocks on each row from left to right, with no interruption (i.e. no white) represents the duration of the riding event.*

Overall, the upstream K_e centre increases at Stage 1 (Figure 4.14 (a)), whilst another K_e centre develops downstream. The former reaches its maximum before the formation of the COLs , and the latter continues to grow at Stage 2 (Figure 4.14 (b)). By the time the downstream structure reaches a maximum at the point in time that the COLs form, the centre upstream has begun to dissipate at Stage 3 (Figure 4.14 (c)). Beyond Stage 3 both energy centres dissipate. This is a sequence of events that characterises downstream development and the growth and decay of these energy centres are informed by the processes listed above. Therefore COLs do indeed develop from unstable synoptic scale Rossby waves (Favre et al., 2012, Omar and Obiodun, 2020). This is also demonstrated by PV, which evolves to the point of overturning the PV contour.

4.4 Medium-range forecasts of COLs and downstream development

As in Chapter 3, the implementation of the COL event-based prediction system is presented. As previously this requires a preprocessing procedure that calculates the ensemble mean variables and then the methods for objectively identifying COLs is then implemented for each ensemble member and ensemble mean. As was the case with the ridging highs and RWB events, the ability to identify COLs in forecast mode presents an opportunity for producing forecasts of the actual COLs, instead of subjectively assessing the geopotential heights. An event-based forecast of the COL that occurred on 22 April 2019 is shown in Figure 4.16. It is clear from this figure that there is large uncertainty in the

EPS forecast of the COL because of the vast difference in how the ensemble systems see the future. It follows for this case, at least, that the predictability of COLs is very low, and for that reason, the confidence in the forecast might be extremely low. There could be a number of reasons for this. For one thing, the objective method assumes that a closed circulation should have formed for the COL to be objectively identified. However, the fact that some ensemble members do not simulate the closed circulation does not mean that a severe rainfall event might be approaching, as far as that ensemble member is concerned. Consequently, if the dynamical precursor requirements, namely a clear case of downstream development are met, but to a less extent, than would have been expected, confidence in the forecast about what might happen would be improved.

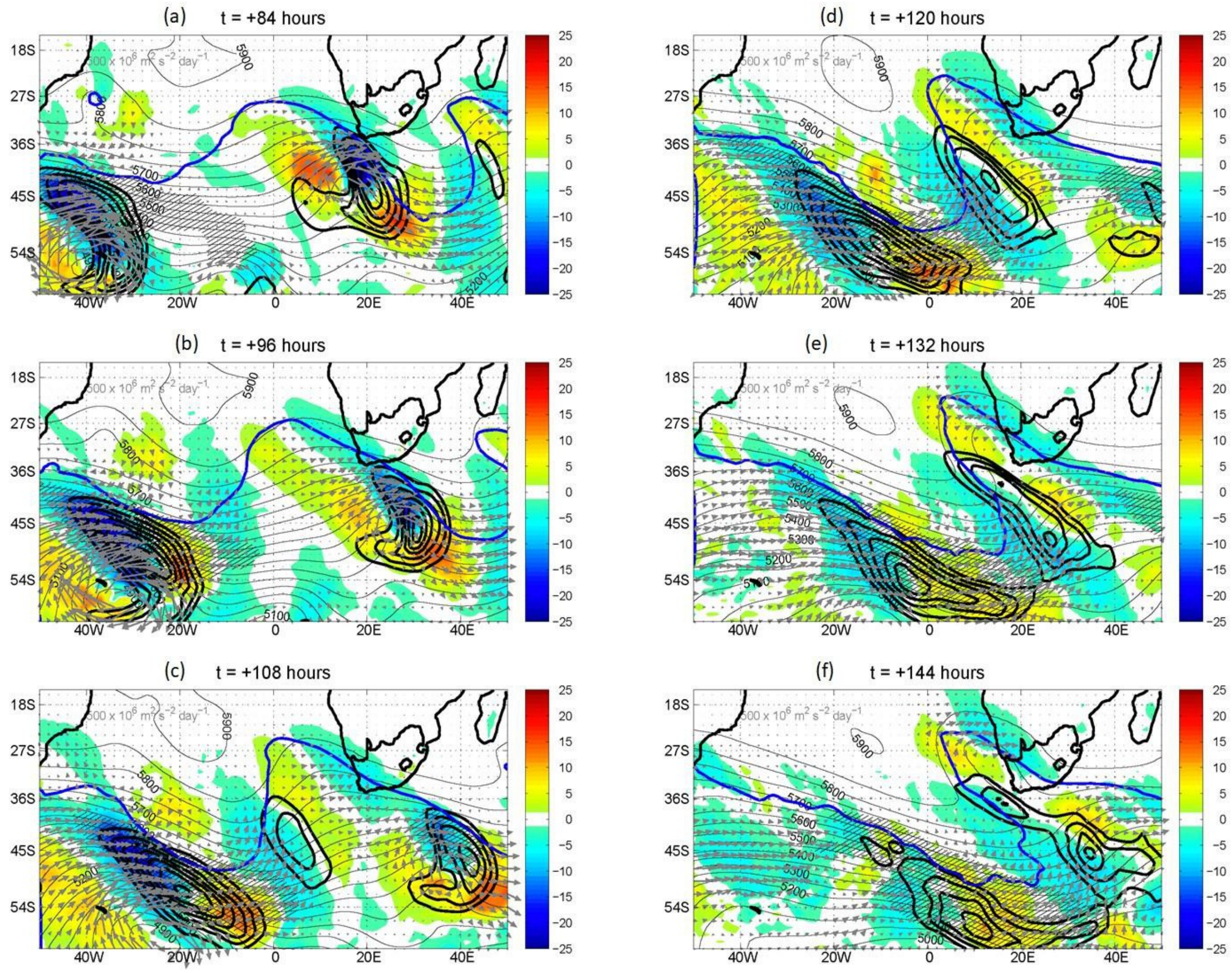

Figure 4.16: *NCEP GEPS forecasts of K_e (thick black contours), jet streaks (hatched areas), the divergence (yellow to red shading) and convergence (blue shading) of the ageostrophic geopotential fluxes (grey arrows), PV = -2 PVU contour on the 340 K isentropic surface (thick blue contour) and 200 hPa geopotential heights (thin black contours) for the COL that was forecast for 22 April 2019. The forecast hours shown are (a) t = +84 to (f) t = +144 hours, in 12 hour intervals.*

The advantage of the issues raised above and in Chapter 3 is that they are based on quantitative (or mathematical) quantities that can actually be calculated and be used to produce post-processed EPS data, which can then be used to give credence to forecasts of the systems involved. Figure 4.16 presents quite a lot of uncertainty, but forecasts of downstream development might change this state of affairs. In Figure 4.16 forecasts of downstream development are shown. It is clear from this diagram that there is evidence of downstream development much earlier than t = +144 hours, which is the forecast hour when the COL is predicted to take place. As expected from the discussion in subsections 4.3.2 and 4.3.3, there is a pre-existing K_e centre that is located just west of 20°W, and as the Rossby wave breaks (note the PV overturning where $\partial_y P < 0$) that is represented by the PV contour turning back on itself, thus causing the supergeostrophic flow to develop and the positive geopotential anomalies to be established, giving rise to the ageostrophic geopotential fluxes. These fluxes transport K_e downstream and as such, a new K_e develops just east of the Greenwich meridian, with its centre located at about 45°S. This centre intensifies and saturates on the hour that the COL is predicted to form, after which it dissipates. These are steps of downstream development that were discussed in the preceding sections, and the orientation of the energy structures are as in the schematic shown in Figure 4.14, indicating the presence of a COL later in the sequence of events. They are very different from the orientation of the K_e baroclinic waves in general as will be shown for the general case of Rossby wave packets in Chapter 5. It follows then that by quantitatively establishing the dynamical precursors of COLs in EPS forecast, we obtain a dynamical indication that a COL is approaching much earlier in the forecast than the actual day of the forecast.

4.5 Summary

Jet streaks have long been established as important in weather systems over South Africa (Tyson and PrestonWhyte, 2000). In this chapter, the dynamics of jet configurations associated with COLs have been explained. The main take-home message in this respect is that the zonal flow redistributes zonal momentum from the entrance to the exit, thus propelling it eastward. As the jet propagates eastward, it brings with it anticyclonic barotropic shear, which in turn increases the strain rate. Potential vorticity contours on the equatorward side of the jet turn back on themselves, as a result, thus transporting high potential vorticity air into the upper troposphere. This creates a high potential vorticity anomaly, signalling the presence of stratospheric air in the upper troposphere. This anomaly induces the closed COL cyclonic circulation. The novel contribution of this chapter is that the breaking waves provide dynamical conditions for downstream development to take place, which is characterised by downstream transfer of eddy kinetic energy. This downstream development always precedes COL formation.

Forecasts of the COL, made possible by implementing the objective identification procedure for identifying COLs in forecast mode, show a great amount of uncertainty because of the disagreement between ensemble members. This suggests that the closed circulation simply does not form in other EPS members, but this does not mean that a highly developed trough does not exist in the forecast. The incorporation of downstream development appears to improve this predictability state of affairs.

5

Rossby wave packets

This chapter is based on the following research outputs that were funded by this project

- Rammopo T.S. (2021) The characteristics of Rossby wave packets in the southern African domain. Unpublished MSc (University of Pretoria). 105 pp.

5.1 Background

The atmosphere has the ability to support many types of osculations, including sound and gravity waves (Holton and Hakim, 2014). These waves are characterised by their restoring mechanisms such as pressure perturbations, buoyancy and gravity. The wave of interest in this chapter is the Rossby wave that occurs in the upper troposphere. It owes its existence to meridional potential vorticity gradients and it is characterised by meridional excursions of air parcels. They have restricted zonal extent that may become non-linear such as their amplitude can become much larger than their wave length. When this happens they are referred to as finite-amplitude waves. Under these conditions, linear-wave theory becomes inadequate for their analysis. A Rossby wave is rarely purely sinusoidal along latitude circles and often exists as a group of waves with areas of superimposition and cancellation along its axis. This consequently suggests that these Rossby waves can be analysed from the point of view of wave packets (Zeng, 1983), which will simply be referred to as Rossby wave packets (RWPs, Lee and Held, 1993, Cheng, 2005, Zimin et al., 2003, Shapiro and Thorpe, 2004, B, Wirth et al., 2018). RWPs can be viewed as the envelope of zonally restricted local wave undulations.

One of the characteristics of RWPs is that they usually propagate with their group velocity zonally, which is faster than the zonal phase speed of propagation of the individual trough and ridge embedded in the wave packet. This is particularly important as group velocities can be associated with the development of new disturbances downstream which may develop into specific weather systems, (Chang, 1993, Holton, 2004, Ghinassi et al., 2018). This paradigm of wave development and decay is referred to as downstream development (see Chapter 4). During downstream development, the eastern flank of these RWPs is associated with the development of troughs and ridges, while the western edge is associated with the decay of the undulations thus having a potential impact on local weather.

Several studies have investigated the link between RWPs and high impact weather events such as heavy rainfalls, intense surface cyclones, heatwaves and drought (Ghinassi et al., 2018). O'Brien and Reeder

(2017) investigated the impact of Southern Hemispheric (SH) transient RWPs over Australia during summer. In that study, it was found that the generation of an upper tropospheric RWP in the extra-tropics was preceded by cyclogenesis associated with an initial, pre-existing disturbance. This suggests that RWPs can potentially be viewed as precursors to extreme weather events such as those giving rise to anomalous precipitation amounts (Wirth et al., 2018). The RWP life-cycle composites in (O'Brien and Reeder, 2017) also revealed the presence of RWPs over the south Atlantic ocean as they propagate eastward, suggesting that they may influence South African weather.

RWPs have also been deemed to have potential implications on predictability and usability in operational environments. Large scale, slow evolving dynamical processes (such as RWPs), are associated with high weather predictability (Warner, 2010), therefore an understanding of RWP dynamics over South Africa, and surrounding regions inherently gives rise to the potential to improve extreme weather forecasts. For example, a poorly forecast flood event associated with a quasi-stationary low pressure system over central Europe was associated with a long-lived RWP (Wirth et al., 2018). This suggests that the knowledge of RWPs as precursors to extreme weather events may significantly improve the forecast in the event of increased levels of uncertainties between Numerical Weather Prediction (NWP) models. In addition, RWPs have the ability to propagate forecast errors downstream. This gives rise to the potential of detecting sources of forecast errors and track the respective errors (and uncertainty) as they grow and propagate in space and time, effectively supplementing the current measures of forecast uncertainty (Szunyogh et al., 2002, Hakim, 2005, Wirth et al., 2018) over the southern African domain. In addition, several studies have associated the propagation of errors developed at earlier time steps and regions, with a modification of forecast skill. Seemingly contradictory results were found in that some studies on associated long lived RWPs were linked to an increase in forecast skill while the very presence of these RWPs was associated with a degradation of forecast skill (Wirth et al., 2018). This leads to the need to elucidate the effect of the RWPs on the skill of medium-range forecasts (i.e. about 10 days).

The utility of the wave packet concept can be extended to optimization studies related to the assimilation of specific observations known to sufficiently reduce analysis errors effectively improving predictability at longer time scales (e.g. medium-range forecasting (MRF) scale). Through a variance signal, the Ensemble Transform Kalman Filter (ETKF) is able to predict the influence of a set of observations on synoptic scale medium-range forecasts. The structure, growth and propagation of this signal can be interpreted as an upper level RWP (Sellwood et al., 2008). In light of the highlighted various applications of RWPs, it seems plausible to view RWPs as a prospect in terms of extreme weather diagnostics and predictability over the southern African domain. It is therefore the aim of this study to assess the feasibility of exploiting the utility of RWPs in South African weather forecasting. The overall aim of the study is to assess the feasibility of the utility of RWPs to improve predictability over South Africa (SA) by determining RWP characteristics, dynamics and relation to high impact weather phenomena and to relate RWPs to medium-range forecasting (MRF).

5.2 Data and methods

5.2.1 Data

To compute the necessary diagnostics we used the 1979-2019 NCEP reanalysis 2 dataset for the wind fields (*u,v,* and *w*), temperature (*T*) as well as the geopotential height (z^0) comprising the standard 17 isobaric levels. The horizontal resolution of the dataset is 2.5° x 2.5° which is sufficient for the purpose of this study given the large scale nature of the processes under study. Later on, we make use of the NCEP ensemble prediction forecasts (EPS) to demonstrate aspects of the knowledge acquired in the study. The forecast data comprises 20 ensemble members and has the same resolution as the re-analysis dataset.

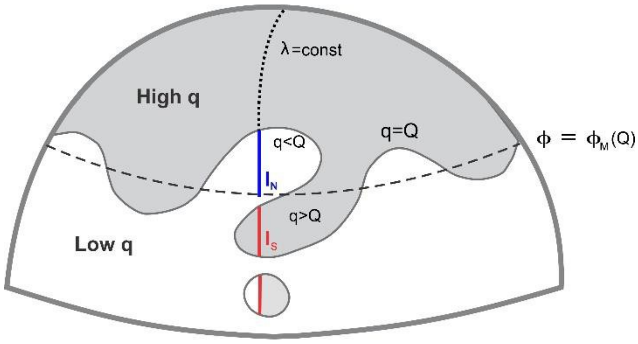

Figure 5.1: *Illustration of the relationship between distorted PV contours, the associated mass equivalent latitude and paths of integration along the meridian.*

Adapted from Ghinassi et al. (2018)

5.2.2 Methods

(a) FAWA diagnostic

The growing interest in the study of Rossby waves from RWP viewpoint, as an atmospheric phenomenon (Lee and Held, 1993, Cheng, 2005, Zimin et al., 2003, Shapiro and Thorpe, 2004, O'Brien and Reeder, 2017, Wirth et al., 2018) gave rise to the development of several RWP diagnostics over the years. These were based on Hovmöller diagrams (Hovmöller, 1949) using the meridional wind v, eddy kinetic energy K_e (Orlanski and Sheldon, 1993), various wave activity formulation (Nakamura and Solomon, 2011, Huang and Nakamura, 2016, Ghinassi et al., 2018; Wirth et al., 2018), envelope reconstruction of the meridional wind (Zimin et al., 2003, Wirth et al., 2018). While most of these diagnostics are useful, their utility is sometimes constrained by some of the assumptions made in their formulation (e.g. the assumption of linear-wave theory in QG formulations, subjectivity in diagnostic frameworks). For this study, we employ Equation 5.1, a novel local Finite Amplitude Wave Activity (FAWA) diagnostic formulated by (Ghinassi et al., 2018) as a diagnostic for RWPs. This formulation is useful in that, it is has been shown to adequately represent local RWPs as coherent structures. This is attractive for the purpose of this chapter as it would enable a straight forward way to objectively identify RWP structures within the computed wave-activity field. The current FAWA formulation can be loosely considered a combination of the strengths of Nakamura and Solomon (2011), and Huang and Nakamura (2016). This effectively suggests that non-linear processes in the subtropics can be adequately represented, unlike with its QG counterpart (Huang and Nakamura, 2016). Figure 5.1 describes the paths of integration and the general idea of wave-activity as a deviation of PV contours from some reference meridional coordinate ($\Phi_M(Q)$).

$$A(\lambda, \Phi_M, \theta) = \frac{1}{\cos \Phi_M} \left[\int_{l_s} (q - Q)\, \sigma \cos \phi d\phi + \int_{l_N} (Q - q)\, \sigma \cos \phi d\phi \right]. \tag{5.1}$$

where λ : Longitude
Φ_M : Mass equivalent latitude
θ : Isentropic surfaceσ
: Isentropic density Q:
PV contour
q : Ertel PV

$$l_s : q \geq Q, \varphi < \Phi_M, l_N : q \leq Q, \varphi > \Phi_M. \tag{5.2}$$

$$\iint_{q \geq Q} \sigma dS = \iint_{\phi \geq \Phi} \sigma dS \tag{5.3}$$

dS : Area element in spherical coordinates

To compute A from gridded data, we adopt the procedure outlined by Ghinassi et al. (2018) and the steps are briefly summarized below:

1. First, one needs to θ select an isentrope that well defines the dynamical tropopause through its intersection with a suitable PV isoline. For the purpose of SA this is usually the 330K or the 350K θ surfaces.
2. Then we linearly interpolate u,v and T to covert the vertical coordinate from isobaric to θ coordinates. The missing quantities (e.g., $\omega = \zeta_\theta + f$ and $\sigma = -g \frac{\partial \theta}{\partial}$) are approximated using centred differences to enable the calculation of isobaric Ertel Potential vorticity (PV).
3. The computation of A requires that a relationship between data/grid latitudes Φ and the reference PV contour Q be established by computing the left and right hand sides of Equation (5.2). This essentially enables us to obtain $Q(\Phi)$ through linear interpolation. The integral is evaluated using the trapezoidal rule.
4. Lastly, FAWA is computed from Equation (5.1) and is subsequently zonally filtered using Equation 5.4.

$$\lambda_d(\lambda, \phi) = \frac{2\pi a \cos\phi}{s_d(\phi, \lambda)} . \tag{5.4}$$

(b) RWP detection algorithm

To detect the actual RWP structures from the FAWA field we make use of a simple algorithm. We leverage the structure of zonally filtered RWPs as seen from (Ghinassi et al., 2018). It is clear that a well-defined RWP will be characterised by closed concentric contours with values decreasing as you move away from the centre of the structure. We therefore leverage MATLAB functions to detect such structures that are closed, and concentric, and have values decreasing significantly away from the centre. We first compute the centre of the maximum contours through the Haversine function, then we collect all the surrounding contours associated with it to detect the decreasing trend described away from the centre. However, we impose restriction on the minimum FAWA value so that insignificant structures are ignored and regarded as noise. The dates and attributes of the occurrence of such events are collected and stored in a database file. Then we discard the possibility of the frequent detection of the same event by analysing the temporal and spatial trends of the dates detected. That is we associate detected structures based on the distance between the centres. Conceptually, it is unlikely to have two RWPs overlapping within 1000 km of each centre, therefore we regard events detected at subsequent steps as part of the same event if they fall within the 1000 km imposed radius.

(c) Composite analysis

To extract the climatological structure of RWPs, we resort to composite analysis. We follow the ”phasing” procedure outlined in previous chapters (e.g. as described in details in the previous chapters).

5.3 Dynamical analysis

5.3.1 Morphology of FAWA RWPs

This section serves to discuss the general evolution, structure, and characteristics of RWPs that mature in the SA domain. The choice of the θ surfaces of interest was motivated by the climatological vertical distribution of $\theta(p)$ and $q(p)$ computed over the defined SA domain (Figure 5.2). Figure 5.2 depicts a sharp increase in vertical gradients of q with decreasing pressure observed between -1 PVU (solid black contour) and -2 PVU (red contour) isolines. Therefore, following the "PV-gradient method" (Hoskins et al., 1985, Morgan and Nielsen-Gammon, 1998, Kunz et al., 2011), where the dynamical tropopause isdefined as the region of the sharpest increase in $\partial_p q$. The dynamical tropopause is expected to be approximately defined by a PV isoline lying between -1 and -2 PVU accordingly.

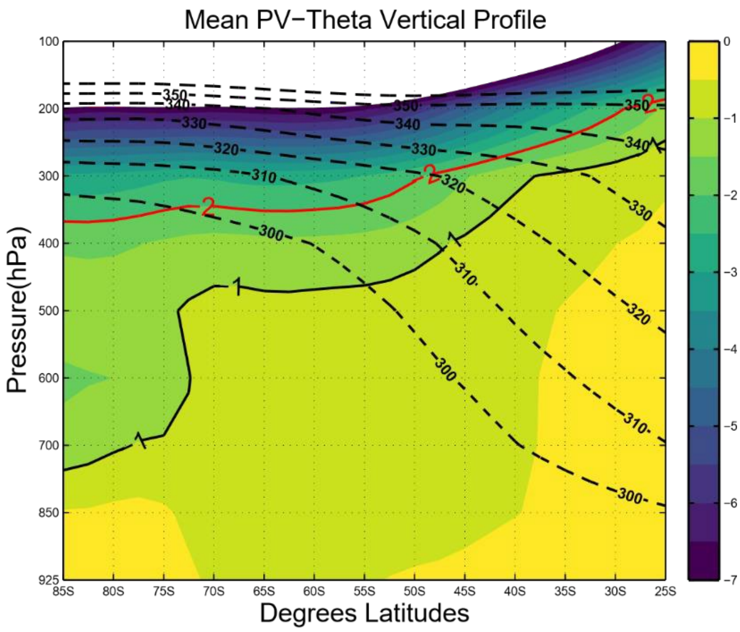

Figure 5.2: *The climatological vertical profile of θ (K),(broken contours) and PV = q (1 PVU = 10^{-6} K kg^{-1}m^{2}s^{-1}), (shaded). The solid black (red) contour denotes PV = -1 (-2) PVU.*

Ndarana and Waugh (2010) showed the spatial frequency of RWB on the 330 K and 350 K θ surfaces, which suggested that the choice of an isentropic surface in the study of Rossby waves may depend on the region of interest so that the 330 K (350 K) θ surface may be adequate when considering processes immediately to the south (north) of SA in the midlatitudes and parts of higher latitudes (subtropics). This notion is further supported by the discussion Chapter 4, where it was observed that the intensity of certain processes during cut-off low formation varied based on the region of interest, and the chosen θ surface. These observations are corroborated by Figure 5.1 which shows that the 330 K θ surface is sufficient for the diagnosis of upper tropospheric processes in the vicinity of 40° S while the 350 K isentropic surface may sufficiently elucidate stratospheric/lower stratospheric dynamical processes in the subtropics (≈ 35°S25°S). The above discussion is particularly important for this study given that the possibility of tropical-extratropical interactions in the development of the RWPs of interest exists.

3091 RWPs were identified in the entire SA domain for the period 1979-2019 on θ_{330K} while only 2125 were identified on θ_{350K}. Table 5.1 depicts the breakdown of RWP identified within subregions of interest within the study domain. It is evident that most RWPs (θ_{330K} = 37.2% and θ_{350K} = 32.85%) reach maturity over the South Indian Ocean (SI), followed by the South Atlantic SAT domain with 996 and 698 (θ_{330K} = 32.2% and θ_{350K} = 28.75%) cases of mature RWPs while the region centred between the two oceans (SSA) of mature RWPs detected. We begin the discussion on the characteristics of RWPs by establishing the general morphological structure of the FAWA RWPs identified in the FAWA data field by means of time-lagged composite analysis. For this purpose, we will consider the ”phased” time-lagged composite means in lieu of geographical composites. The former is computed by aligning and putting into phase the centres of individual mature RWP events over the entire SA domain which sufficiently eliminates the probability of some dynamical features of the evolution being subdued owing to the geographical averaging of sparse events.

Table 5.1: *Number of RWPs detected per region in the SA domain.*

θ surface	Area	Number of RWPs
330 K	South Atlantic (SAT)	996
	Middle of South Africa (SSA)	946
	South Indian (SI)	1149
350 K	South Atlantic (SAT)	698
	Middle of South Africa (SSA)	611
	South Indian (SI)	816

First, we consider the evolution on the θ_{330K} surface (Figure 5.3). During the evolution of RWPs, the development and termination phases are of particular interest. The sequence of events begins at t = -96 h (Figure 5.3 (a)) with a pre-existing belt of FAWA extending across the domain (90W-90E) and is comprised of three areas of local FAWA maxima located on the western (most intense) and eastern bounds of the domain, as well as one rooted approximately in the centre. While the eastern half of the domain depicts a fairly zonal distribution of FAWA, the western portion is oriented north-eastward extending from the local maximum. During this time, the relative maximum located on the west bound (and between 20°S and 20°S) of the domain is clearly in response to a weak trough (and a ridge downstream) as depicted by the juxtaposed $v^0 > 0$ and $v^0 < 0$ isotachs located in the vicinity of the relative FAWA maximum as well as the small northward bulge in the PV contours over the area. Between t = -96 and -48h (Figs 5.3 (a-c)), we see an intensification of the trough-ridge system as it propagates north-eastwards towards the 0° relative longitude with v^0 isotachs assuming a north-west-south-eastward orientation in line with that of the FAWA field. This observation is more evident on the $\theta_{350}K$ surface (see Figure 5.4).

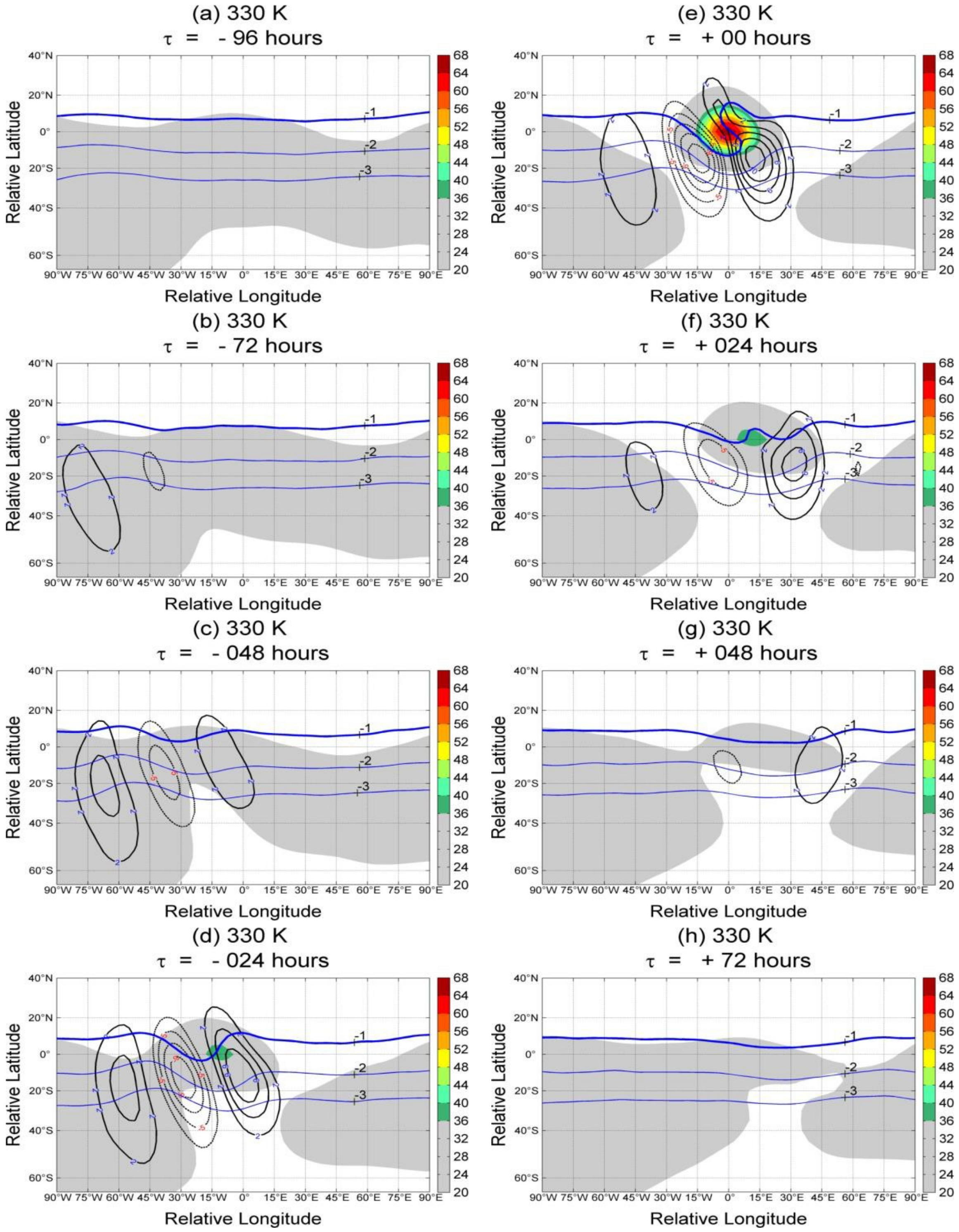

Figure 5.3: *The θ_{330K} evolution of RWP as depicted by the FAWA field (A)(filled, units = ms^{-1}). The thin broken and solid black contours denote $v'_{330K} > 0$ and $v'_{330K} < 0$ respectively (contour interval = 4 ms^{-1}). The thin and (thick) blue contours indicate the PV -3,-2 and -1 isolines (PVU).*

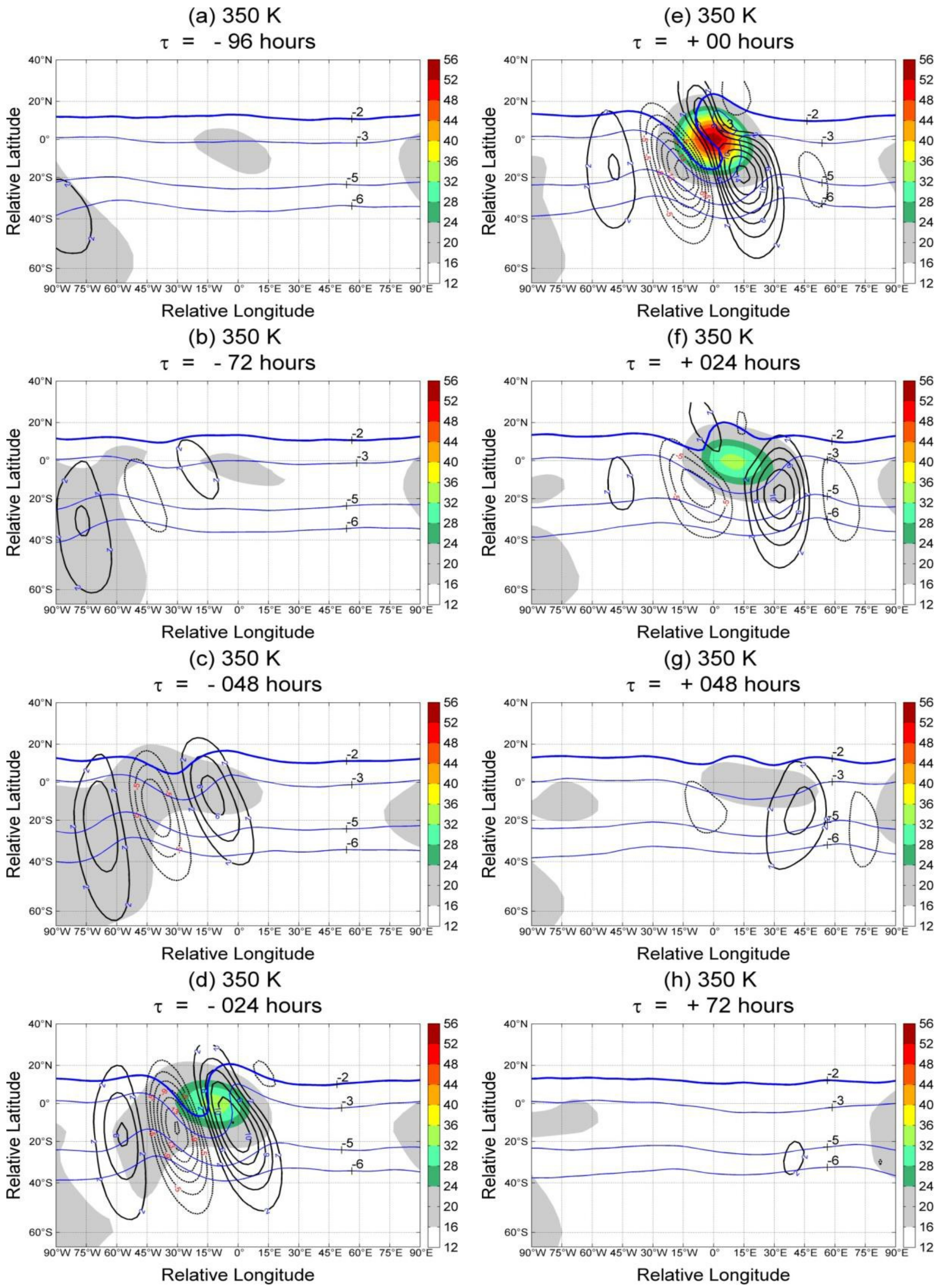

Figure 5.4: *As in Figure 4.3 but for* θ_{350K}.

The orientation of the western flank of the upstream trough assumes a north-south orientation and ceases to intensify indicating that the active portion of the system is located downstream. At this point, we speculate that this observation is a result of the decaying of the system upstream. Therefore, the north-west-south-eastward (north-south) orientation of the v^0 isotachs indicates the baroclinicity (barotropicity) of the system. The above sequence of events suggests that the source of wave activity exists at higher latitudes and propagates north-eastward towards lower latitudes. In response to the intensification of the system, the undulations of the PV contours increase in amplitude which gives rise to the development of a local FAWA maximum downstream (characterised by closed concentric contours) of the trough-ridge-trough wave system and enveloping the active portion of the wave (the downstream ridge-trough couplet), this is clearer at t = -24h and is located at ≈ (15°W,0°S). In line with the current framework, we regard t = -48h as the inception time of the RWP. While this is the case, it is evident that the development of this RWP is preceded by the decay of an incipient RWP structure as depicted by the pre-existing trough alluded to previously, at earlier time steps. The fact that the ensuing FAWA diagnostic was unable to detect the weak perturbations at earlier times as coherent structures is a consequence of the zonal filtering employed which seeks to discount phase information of the system (Ghinassi et al., 2018). Therefore, to make the distinction between the two, we refer to the pre-existing perturbation as the initial Rossby wave train (RWT) which gives rise to the RWP in question. In addition, the zonally coherent belt of FAWA is broken at t = -24h with the first fault occurring downstream the disturbance at about 15°E while the upstream connection disappears by t = 0h. At earlier time steps, the system depicted some linearity owing to the structure and orientation of the PV isolines' orientation. However, at t = -24h the slight anticyclonic orientation of the trough bulge is a tell-tale sign of the onset of non-linearity of the system, which is indicative of the increasing maturity of the system and its approach to the decaying stage. In light of the above sequence of events, we regard the period t = -96 to t = -24h as the development phase of the RWP.

The onset of the termination stage of a RWP is usually marked by RWB (Wirth et al., 2018). It consequently follows naturally that we ought to identify the onset of this process in our evolution to sufficiently recognise the onset of the termination stage in the life-cycle of the RWP. The RWP propagates zonally within 48 hours such that it is located at 0° at t = 0h when the system is at its most mature. At this time, it is marked by maximum deformation of the PV contours (-1 PVU ≈ dynamical tropopause) as well as v^0 isotachs characterised by stretching equatorward in an anticyclonic direction. The orientation of these structures is characteristic of the termination stage in the life-cycle of baroclinic waves (life-cycle 1 in the study of Thorncroft et al., 1993).

Correspondingly, the FAWA local maximum is at its most intense ($A_{\theta 330K} \approx 68ms^{-1}$, $A_{\theta 350K} \approx 56ms^{-1}$) and sufficiently envelopes the highly deformed ridge-trough couplet as per the definition of FAWA (e.g. Huang and Nakamura, 2016, Ghinassi et al., 2018). The termination stage is further emphasized by the rapid decrease in the amplitude of the RWP beyond t = 0h. Downstream the decaying RWP, there exists a weak and newly developed trough which briefly attempts to intensify at its leading edge at t = 24h but the overall growth is halted by the rapidly decaying components upstream as the overall system propagates eastward. The eastward propagation is accompanied by a small meridional component which sees the overall propagation becoming south-eastward at latter time steps, and is accompanied by south-eastward orientated deforming RWP structure. If one considers the propagation of the RWP during the entire evolution while considering the phase information as offered by the v^0 contours, the overall movement of the disturbance can be summarized as: north-eastward, eastward, then south-eastward. This propagation characteristic is reminiscent of a Rossby wave undergoing wave refraction followed by wave reflection. This may be of relevance for the current study region given that some studies (e.g. Reason et al., 1987, O'Brien and Reeder, 2017) have discussed and observed the possibility of the occurrence of Rossby wave reflection in the vicinity of SA, particularly over the SAT sector. This discussion is continued in subsequent sections.

The role of the jet stream in the evolution of RWPs is noteworthy. The evolution is characterised by a zonally coherent single jet (SJ) structure at earlier time steps, but approximately follows the deformation and undulations of the FAWA field as well as the PV isolines. An inspection of Figure 5.5 reveals that when considering the phase information, the RWP propagates along the jet stream and is most evident during the north-eastward propagation during the development phase. This further alludes to the importance of the position and orientation of the jet stream in inducing the propagation of Rossby waves as studies have found in general (e.g. Hoskins and Ambrizzi, 1993, Wirth et al., 2018), and more recently for SA (see in Chapters 3 and 4). The apparent orientation of the jet stream is associated with the behaviour of the PV isolines as it is known that its structure follows that of the perturbations of the PV contours found in regions of large meridional gradients of the PV isolines (Harvey, 2016, Wirth et al., 2018). This behaviour can be readily observed in Figure 5.5, particularly from t = -24 h where the orientation of the *u* isotachs enveloping the jet streak seemingly coincides with that of the undulations of the -1 PVU isoline. In addition, this observation further gives credence to the notion of the jet stream as a wave guide for Rossby waves (Hoskins and Ambrizzi, 1993; Ambrizzi et al., 1995; O'Kane et al., 2016; Wirth et al., 2018).

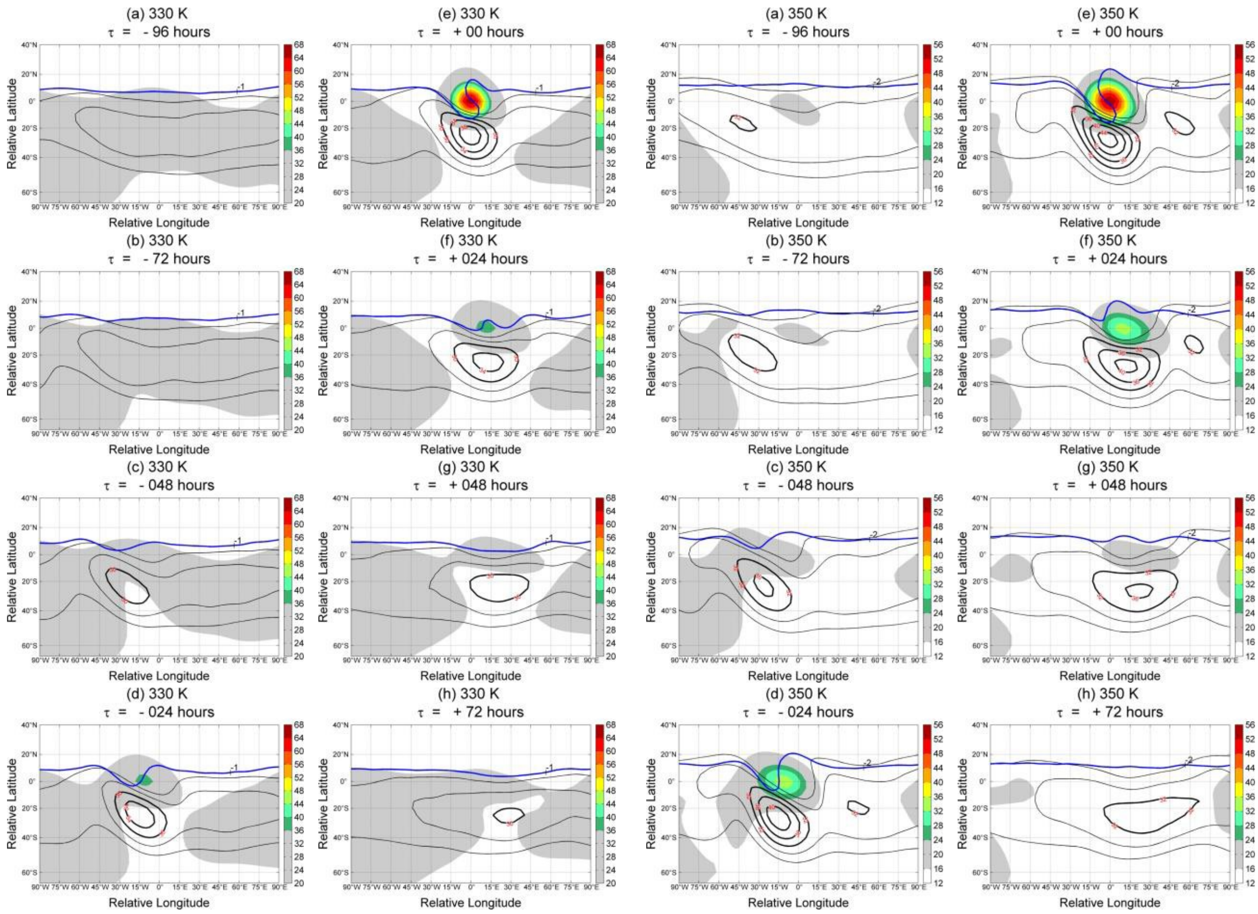

Figure 5.5: *The shading denotes FAWA evolution as in Figure 5.4, but includes the isotachs of the mean zonal flow, u (black contours, interval = 4ms^{-1}) for θ_{330K} left panels (first two) and θ_{350K} right panels. The jet core is highlighted by the orange isotachs.*

Regarding the θ_{350K} surface, the above arguments hold as the processes are similar in nature, and are mostly associated with a few notable differences. First, it is evident that the coherent FAWA structure is thin relative to the distribution on θ_{350K} and has a larger northward meridional component. This orientation is also mimicked by the jet stream isotachs and may be suggestive of the possibility of the existence of the connection between the higher latitudes and the tropical/extratropical regions given how far north the FAWA field extends and is oriented. Another difference is seen in the anticyclonic RWB. In the former, the dynamical tropopause was defined by the PV = -1 PVU isoline, while in the case of the latter it is defined by the PV = -2 PVU material contour. This observation is consistent with the conclusions drawn from Figure 5.2. That is, the θ_{330K} (θ_{350K}) may be suitable for the diagnosis of Rossby waves (e.g. RWB) slightly north (south) of SA. To complement this observation, the overall consensus as suggested by Figures 5.3 to 5.5 is that the initial perturbations originate from higher latitudes and altitudes (stratosphere) as guided by the jet stream.

5.3.2 Spatio-temporal characteristics of RWPs over SA

Prior to the discussion of RWP dynamics, it is important to examine the climatological distribution of FAWA. It can be seen that there exists some variability in the spatial distribution of the mean FAWA field with the progression of the seasons, with the greater degree of variability evident on the 350 K isentropic surface (Figure 5.6). It is also evident that a large portion of the SH FAWA distribution exists between the Pacific and parts of the South Atlantic oceans owing to the existence of areas of large localized values of FAWA within the domain for both θ surfaces. The austral summer season boasts the largest values of FAWA in the midlatitudes, with the maximum centred south-east of New Zealand for both θ surfaces. While this region of maximum FAWA exists throughout the year, it progressively weakens as its centre shifts eastward (180°E to 150°E) between summer (DJF) and winter (JJA) seasons where it is at its weakest centred at ≈ 150°E in the vicinity of the subtropical jet between Australia and New-Zealand. There exist two areas of local FAWA maxima between 150°W and 0° at ≈ 25°S with the relative maximum centred between South America and New Zealand at ≈ 25°S during summer months and the secondary maximum is positioned over the coast of Brazil. It is worth noting that, unlike the midlatitude summer FAWA maximum which decays steadily with time, the two areas of enhanced FAWA in the subtropics seem to disappear at a greater rate and would have completed decayed by winter. These relative maxima of FAWA exist within a belt of coherent FAWA which spans the entire latitude circles in the midlatitudes during all (DJF and MAM) seasons for the θ = 330 K (350 K) case. This belt is ducted within the SH climatological jet streams and indeed coincides with the SH storm track which points to the baroclinic nature of the mean flow (Berbery and Vera, 1996; Hoskins and Hodges, 2005; Wirth et al., 2018). It is known that jet streams can serve as efficient wave guides in the midlatitudes such that their geographical position coincides approximately with that of the midlatitude wave guide and storm tracks (Berbery, 1991, Wirth et al., 2018). It follows then that the climatological distribution of FAWA in the SH midlatitude approximates the locations and distribution of the midlatitude Rossby wave guide in the SH.

While this structure is predominantly confined in the midlatitudes for the θ = 330 K case, the distribution of FAWA for the θ =350 K case has a greater and variable meridional extent in such a way that climatological features of the lower stratosphere FAWA distribution within the subtropical regions (e.g. the two FAWA maxima alluded to above) are exposed. With the progression of time, the SH FAWA becomes less concentrated in the Pacific-South Atlantic Ocean domain as a weak maximum develops over South America during MAM months accompanied by enhanced FAWA values between the South Atlantic and Indian Oceans, and a marked decrease in intensity of the SH FAWA maximum. During the SON season, the intensity of the SH FAWA maximum begins to increase while the observed summer FAWA configuration begins its recovery. The sequence of events then suggests that the SH experiences most of the wave activity during the summer months and the least amount during the winter months. In addition, it is evident that large values of FAWA are observed in the vicinity of various jet streams in the SH. This stands to reason as it is known that jet streams play a role in the propagation and breaking of Rossby waves (Peters and Waugh, 2003). For example, the fact that an area of local FAWA maximum occurs in the vicinity of the subtropical jet in the ”double-jet downstream (DD)” configuration in Peters and Waugh (2003), where a polar jet is observed downstream of a subtropical jet, suggests that poleward-anticyclonic RWB is prevalent in that region. Furthermore, the seasonal variability of the spatial distribution of FAWA appears to be similar to the seasonal variability of the spatial distribution of anticyclonic RWB (AWB) frequency in the SH of Ndarana and Waugh (2010), (see their Figure 8). For example, it can be seen that the frequency of AWB decreases around 180°E with time as it increases between 60°E and 120°E. This shift in frequency is mirrored by a similar shift in e.g. the New Zealand FAWA maximum alluded to above. This then suggests that there might be a relationship with regions of maximum localized FAWA and AWB.

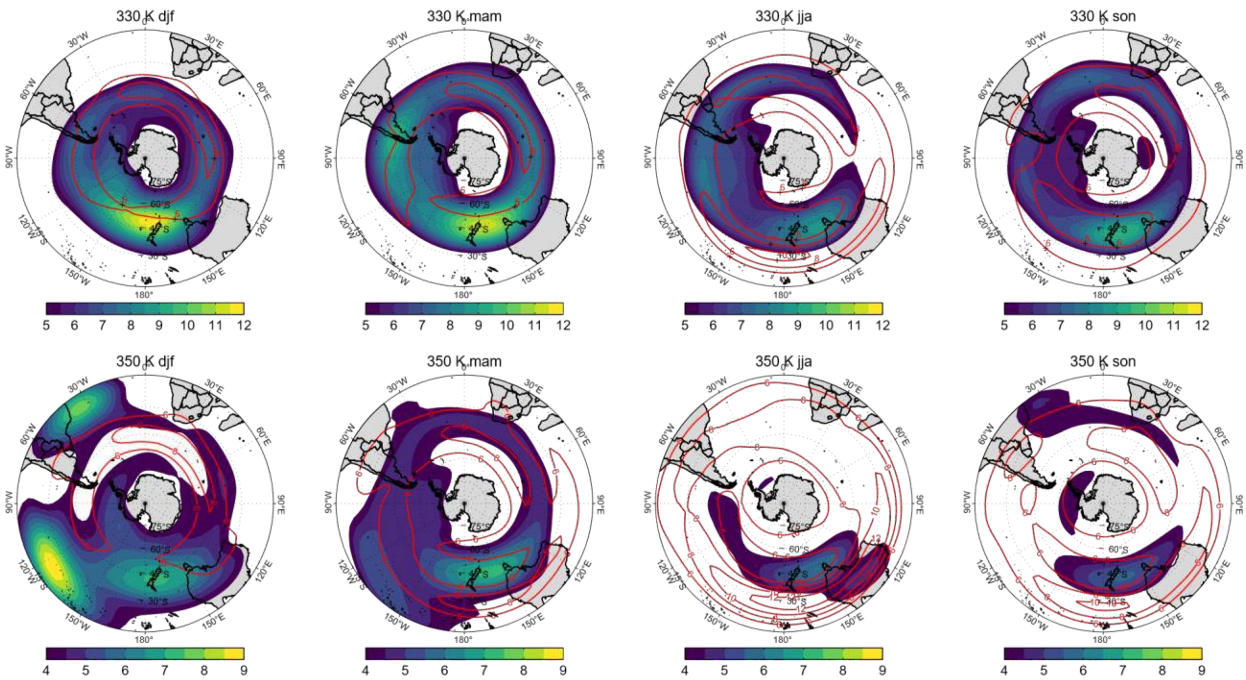

Figure 5.6: *Seasonal distribution of 330K (top panel) and 350K (bottom panel) FAWA (filled contours) where the contour interval is 0.5 ms^{-1}. The thin red contours are the corresponding mean isotachs of the zonal component of the wind on the respective θ surfaces.*

In line with the study objectives, the distribution of FAWA in the SA domain is of particular interest. It is evident that the FAWA field in the region is more pronounced during the transition seasons (MAM and SON), particularly over the South Atlantic Ocean and just south of SA (see top panel SON and MAM respectively). Perhaps the most interesting features of the seasonal variation of FAWA in the vicinity of SA is elucidated by FAWA on the 350 K θ surface. As alluded to above, there exists a local region of pronounced FAWA values on the coast of Brazil during the austral summer months. This area of pronounced waviness coincides with the approximate position and season of occurrence of the South Atlantic Convergence Zone (SACZ). This is a well-known rain-bearing climatological feature of the subtropical summer season over South America characterised by the north-west-south-east orientation of convective cloud bands extending over the Amazon basin, over Brazil and into the west sectors of the South Atlantic Ocean (Liebmann et al., 1999; Robertson and Mechoso, 2000; Carvalho, 2003). The formation of the SACZ has in part been associated with the existence of a Rossby wave guide which gives rise to the propensity of wave activity to converge in the region of SACZ on the coast of Brazil. As the observed DJF structure on the coast of Brazil (in conjunction with the SACZ) disintegrates at the back end of summer, FAWA attains maximum values over the South Atlantic and South Indian Ocean areas neighbouring SA during the transition seasons. In addition, the FAWA distribution during DJF and SON in this region assumes a north-west-south-east type of orientation extending away from the region of maximum FAWA in the domain. The synchronous disintegration of the local maximum over the coast of Brazil and the maximization of FAWA together with the local orientation and distribution of FAWA in the SA domain suggest that the latter might be associated with the wave activity occurring in the SA domain so much so that it may be seen as a potential source of wave-activityfor the SA domain in the lower-stratosphere. This speculation would appear to be reasonable given thefindings of Berbery et al. (1991) and Ambrizzi et al. (1995) which found that wave trains emanating from the south tip of South America can be diverted either equatorward towards the vicinity of the coastof Brazil (large meridional component), towards SA (slightly small meridional component) or more zonally ducted within the core midlatitude Rossby wave guide. In the second case, we speculate that the SACZ may potentially play a role in the reflection of the wave activity emanating from the southerntip of South America so that it is ultimately deposited in the vicinity of SA over the SAT domain. Furthermore, the speculation is further fuelled by the fact that the local FAWA maximum over the Brazil coast (or the SACZ) coincides with the climatological austral summer Rossby wave source (Trenberth et al., 1998, Holton and Hakim 2004, Sardeshmukh and Hoskins, 1988) reported by Shimizuet al. (2009) and Nie et al. (2019) in the upper troposphere.

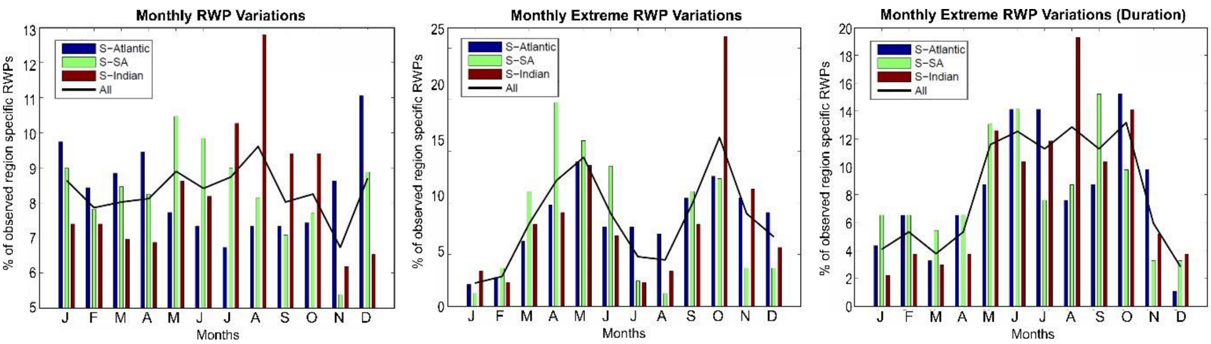

Figure 5.7: *The interannual trends in RWP occurrence within each subregion (SAT is blue bars, south of SA is green, and SI is maroon. The overall trend is depicted by the black solid line over the bars). This is calculated by computing the percentage of events relative to the total number of events within the entire SA domain. From left to right: Monthly variation, Monthly extreme variations in terms of intensity, Monthly extreme variations in terms of intensity (duration).*

Regarding the temporal variability of RWPs in the SA domain, Figure 5.7 summarises the intra-annual frequency of occurrence of mature RWPs within the subregions of SA to detect any region-specific trends of events. These are defined as follows: the region within the South Atlantic Ocean (SAT, 10°W-10°E), the South Indian Ocean region (SI, 30°E-50°E), and the region bounded by the two oceans (south of SA (SSA), 10°E-30°E). The leftmost tile in Figure 5.7 reveals a general trend in the frequency with peaks during transition seasons (May and August months). The peak observed during August is largely attributable to the occurrence of events in the SI domain, and thus serves as an anomaly relative to the observed trends for other domains. It is also noteworthy that between July and October, the frequency of events is still generally higher over the SI region. Likewise, it is evident that the SAT domain experiences a peak in RWP occurrence during summer as indicated by the sharp increase in December. In the study of RWPs, extreme events are of interest. In this study, we examine two attributes of RWPs in this regard, namely: the intensity and duration. The tile in the middle is a depiction of the intra-annual occurrence of extreme RWP cases over SA. We define such events as those with amplitudes (duration for the right panel) greater than the 90th percentile of the dataset. A clear trend exists and it shows that the frequency of extremely intense RWPs peaks during MAM and SON, are at a minimum during winter months for all the subregions. In contrast, the same trend is not readily observed for the anomalous RWP events occurrence, with the bulk of the events occurring mostly at the latter stages of MAM and the beginning of winter. However, except for the anomalous accounts in the SI domain, a trend similar to that of extremely intense events is observed during the onset of SON. Figure 5.8 depicts the inter-annual trend in the occurrence of RWPs for the entire SA domain. The regression line suggests that there is a significant upward linear trend in the occurrence of events over the SA domain. This regression explains ≈ 19 % of the observed variation ($R^2 = 0.19$).

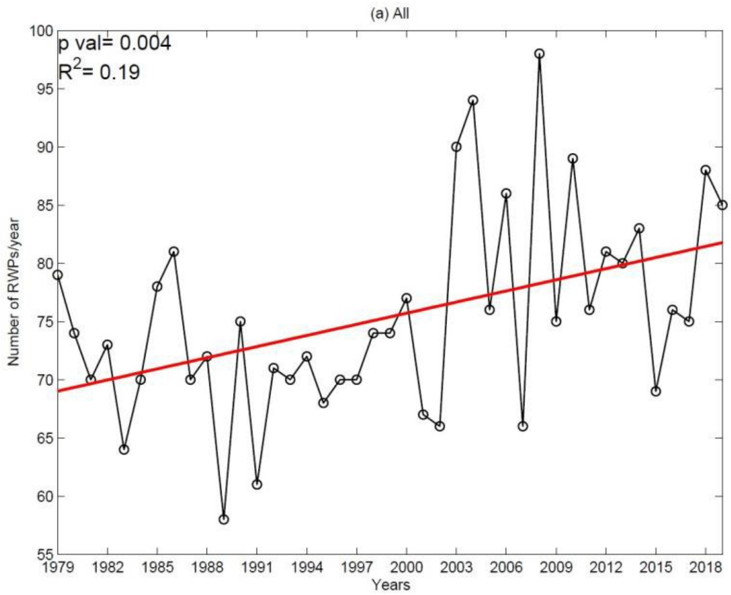

Figure 5.8: *Annually observed frequency counts of RWPs over the SA domain.*

5.3.3 Dynamics of RWPs over SA

In the previous sections, we established some of the morphological, spatial and temporal characteristics of RWPs. Having done so, it is now of relevance establishing the structure and characteristics relative to the landmasses given the practical quest of the current study. Figure 5.9 summarises the evolution of RWPs that attain maximum amplitude in the SAT domain on θ_{350K} surface. This region will be the subject of study for the remainder of the analysis. This comes as initial results showed that the underlying processes are independent of subregions within the SA domain for the most part. There appears to be consistency between the composite evolution from the point of view of relative grids and that taking place in geographical space. First, we note the correlation between the FAWA belt extending across the midlatitudes and the position of the jet stream. The importance of this observation is discussed in previous chapters and essentially demarcates the midlatitude Rossby wave guide. Therefore, for the purpose of brevity, the geographical evolution in Figure 5.9 should be contrasted with its relative latitude-longitude space counterpart. The key points from this evolution are as follows. It becomes clear that there is a link between the evolution of RWPs that make their way to the SA domain and processes occurring in the South American domain. For example, the northeastward extension of FAWA alluded to previously is more evident at earlier time steps (Figures 5.9 (a) to (d) (left panel)) when FAWA residing west of the southern tip of South America extends north-eastward towards the region of the SACZ. Later steps further reveal clear development of a FAWA RWP emanating from this region in the SACZ after interacting with the pre-existing climatological feature in that area.

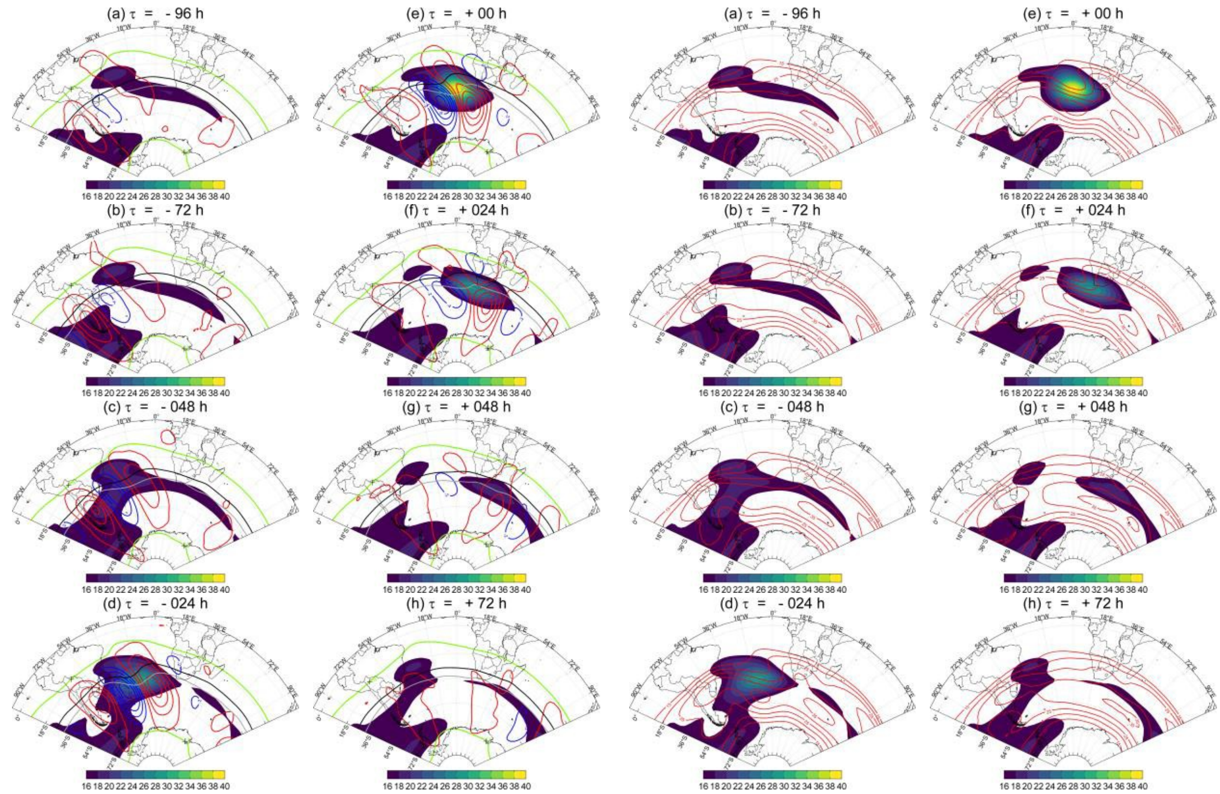

Figure 5.9: *As in Figure 5.3, but for geographical latitudes.*

The pre-existing disturbance is confirmed by Figure 5.10 (a) (t = -96 h) to be a pre-existing RWP which seemingly is equivalent barotropic (indicated by the coincidence of surface z'_{850hPa} (filled) and upper tropospheric z'_{200hPa} contours) at its trailing edge, which is an indication of the decaying of the ridge (red contour fill) structure in that region (along the coast of Chile). The leading edge of this RWP is clearly baroclinic as shown by the westward lag of the z'_{200hPa} contours relative to the surface disturbances and subsequently goes on to mature farther downstream. This trough is visibly associated with surface cyclonic circulation and is further corroborated by the small areas of localized $\zeta_{850hPa} < 0$ contours (orange) within the surface trough region. The area of $\zeta_{850hPa} < 0$ becomes more coherent with time as the system intensifies. The surface cyclone observed at earlier time steps is located within the south-eastern Argentina region (RG3 in Reboita et al., 2009) which was found to be one of three climatologically favourable regions for cyclogenesis in the South Atlantic (Reboita et al., 2009). In addition, they found that this region boasted the most number of cyclogenesis cases as well as the greatest number of intense cyclogenesis cases. Moreover, other studies (e.g. Simmons and Hoskins, 1978, Gan and Ra, 1991, Sinclair, 1996, Reboita et al., 2008) have attributed the prevalence of cyclogenesis in the region to the baroclinic instability associated with the ambient westerlies as well as the transient upper level troughs moving into the region from the Pacific Ocean (Necco, 1983a; Reboita, 2008). Studies (e.g. Hoskins et al., 1985; Glatt and Wirth, 2013; O'Brien and Reeder, 2017; Ndarana et al., 2020a) have alluded to the interaction between surface and upper air systems, citing surface cyclones as triggers of upper air systems. In this case, however, it is unclear whether the surface cyclone occurred first and intensified the upper air trough, or the wave energy emanates from the pre-existing upper air trough.

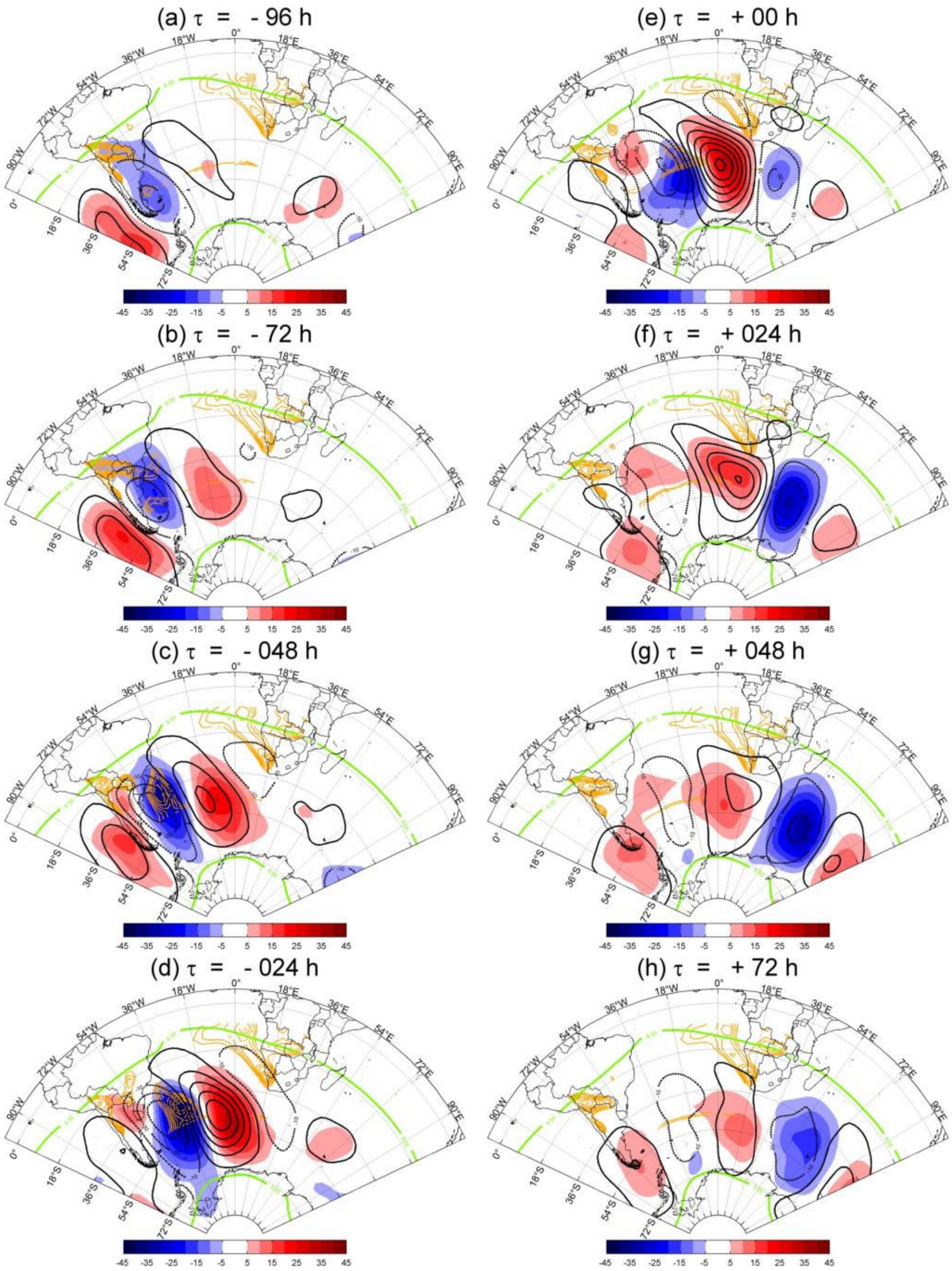

Figure 5.10: *The evolution of* z'_{200hPa} *(black dashed contours indicate* $z'_{200hPa} < 0$*, solid black contours represent* $z'_{200hPa} > 0$*). The blue (negative) and red (positive) shadings denote the 850 hPa* z^0 *(m). The green contour denotes the critical latitude and the orange contours indicate the* $\zeta_{850hPa} < 0$ *(*s^{-2}*).*

The interesting propagation mechanism observed and discussed previously is evident here. That is, the wave activity emanating from the high latitudes towards the high latitudes seemingly bounces off the SACZ structure so that the propagation of the ensuing RWP becomes mostly horizontal prior to the termination stage, followed by a south-eastward movement reminiscent of wave reflection. O'Brien and Reeder (2017) found evidence of Rossby wave reflection in the vicinity of SA over the SAT domain and can be characterised by the sharp north-west to south-east orientation of the orientation of v^0 or z^0 contour structures and propagation towards higher latitudes, but with a zonal component. The process of wave reflection is known to occur in the vicinity of the critical boundary which is defined as the latitude in which the phase speed c_p of the RWP equals the speed of the mean zonal flow u and is characterised by highly non-linear processes. Furthermore, in this region, RWPs can undergo significant deformation leading up to RWB, or their associated wave activity can be reflected or absorbed. In this study, $c_p \approx 8.55 ms^{-1}$ (light green contour) is estimated from the Hovmoller plot of v^0 prior to the onset of the RWP termination stage (not shown). Therefore, the critical latitude (green contour) is located between 5° S and 10° S as denoted by the c_p contour. We note that the equatorward bulge of the critical boundary just north of the SACZ region is reminiscent of the bulge observed in the study of RWPs over southwest Africa in O'Brien and Reeder (2017) (see their Figure 15 (a)). It is at this point that wave reflection was identified, and was subsequently followed by the intensification of a disturbance downstream that would later make its way towards Australia. In contrast, we observe the intense deformation of the RWP in the vicinity of the critical latitude so much so that RWB follows. Just after the RWB occurs, we see the decaying system propagating slightly south-eastward. Therefore, it is not immediately clear that the process occurring between t = - 24 h and t = 0 h is either simply RWB or a combination of RWB and wave-reflection.

5.3.4 Energy and downstream development

Given the limitations of the employed FAWA diagnostic, we resort to the well-known K_e equation to diagnose key processes governing the evolution of RWPs over the SA domain. Ndarana et al. (2020) demonstrated the utility of this framework (proposed by Orlanski and Katzfey, 1991) in diagnosing downstream development leading to CoL formation. In the study, a schematic was provided, which highlighted key processes governing this evolution, namely: baroclinic conversion and the ageostrophic geopotential flux convergence. These processes are further identified by Wirth et al. (2018) as important mechanisms in the life-cycle of RWPs. Therefore, in this section, we diagnose the life cycle of RWPs maturing over the SAT subregion using the proposed framework, with particular interest in the two processes described previously.

The left panel in Figure 5.11 illustrates the evolution of K_e during the life-cycle of the ensuing RWP. Between t = -72h and -48 h (Figures 5.11 (a) and (b) – left panel), we observe a local area of growing K_e downstream the pre-existing trough outlined earlier. This region approximately coincides with the local maximum of FAWA discussed previously, observed in the region. During this period, it is evident that there was a pre-existing local K_e centre located on the south tip of South America but subsequently disappears with the progression of time. This can be associated with the ageostrophic geopotential flux divergence as indicated by the corresponding ageostrophic geopotential flux vectors pointing north-eastward downstream of the trough. It is also evident that the development of the growing EKE upstream of the growing disturbance is through baroclinic conversion as illustrated by the coincidence of the intensifying $-\omega\alpha$ contours with the local K_e area, and in line with Stage 1 in Chapter 4.

The newly developed K_e centre continues to intensify and by t = -24 h, it is located farther downstream than the now weakening trough and is collocated with a newly developing K_e centre in response to the deepening ridge. This is evidence of Stage 2 observed in Ndarana et al. (2020). This is further corroborated by the ageostrophic geopotential flux vectors as it intensifies at this time and point upstream away from the maturing K_e centre and into the newly developing K_e centre indicative of the role of the convergence of ageostrophic geopotential fluxes in the development of K_e centres.

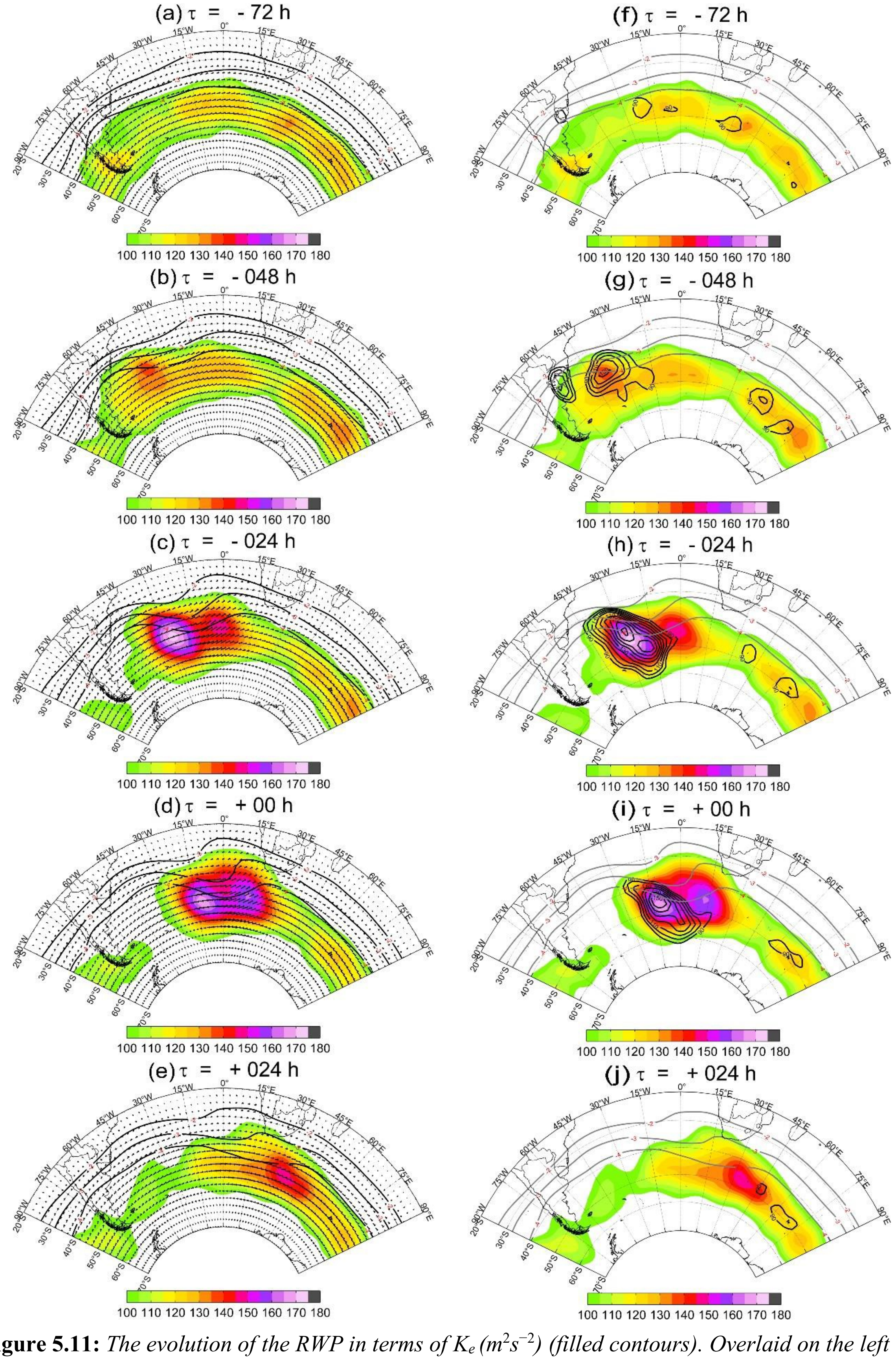

Figure 5.11: *The evolution of the RWP in terms of K_e (m^2s^{-2}) (filled contours). Overlaid on the left panel are the vectors depicting ageostrophic fluxes of geopotential as well as PV contours (-2,-3,-4 PVU) on θ_{350K}. The right panel depicts $-\omega\alpha$ (black contours) where the units are m^2s^{-2}/6h.*

At t = 0 h the newly formed K_e centre has intensified with the deepening ridge at the expense of the old centre (now dissipating) still located downstream of the decaying trough. This process is also indicative of a weakening baroclinic conversion. It is at this time that the RWP termination occurs and is usually accompanied by RWB as previously discussed. Unlike the CoL case, the cut-off structure and associated circulation is not immediately observable in the PV contours, however previous results point to the existence of such a circulation, albeit weaker in this case because not all RWPs undergo RWB and the phase destructiveness of the computation of the composite means. Lastly, the K_e dissipates completely while its newly formed counterpart upstream of the newly developed trough lingers propagating eastward while steadily decaying, marking the end of the downstream development of the baroclinic wave, and the continuation of the termination phase of the RWP. This result extends the findings in Chapter 3 to RWPs. That is, like CoLs, the development of baroclinic RWPs over SA is largely associated with the process of downstream stream development.

5.4 RWPs and predictability

5.4.1 Cut off lows and RWPs

To demonstrate the usefulness of the concept of RWP as a prediction tool, we consider the case of a well-known CoL that brought lots of rainfall over the east coast region of SA on 22 April 2019. To achieve this, we make use of the NCEP EPS data that comprises 20 ensemble members (perturbed) to mimic what would have been a forecast issued on 14 April 2019, 8 days before the onset of the CoL over SA. FAWA was computed at θ_{330K} for all 20 ensemble members for the entire forecast window. The aim of this exercise is not to objectively quantify the accuracy of the forecast itself, but to assess how the qualitative information acquired by computing the ensemble mean of the computed, and filtered FAWA could have been useful in the forecasting procedure, given the knowledge acquired in this study. By considering the forecast window between the 18th and 23rd of April 2019 (96 hours up to 228 hours of the forecast time step) the typical evolution associated with a baroclinic wave as found in the current study was evident. Figures 5.12 (a-d) depict the typical SACZ-ward extension of wave activity emanating from the higher latitudes as revealed by the composites. The climatological structure over the SACZ region is equally evident as well as its interaction with the SAT domain. By 19 April the RWP would have already started developing over the SAT region and continued to intensify with time until the onset of the CoL clearly visible on 22 April 2019 at 00Z (Figure 5.12 (i)). This is marked by the deformation of the -1 PVU (red) and -2 PVU (blue) PV giving rise to the cut of structure that lingered in the vicinity of Cape Town. Due to the cut-off low (which can be seen as RWB), the system dissipates, marking the termination stage of the RWP.

5.4.2 Heatwaves and RWPs

Another interesting extreme weather phenomenon is heatwaves. Some studies have associated the relationship between extreme temperatures (heatwaves) and RWP occurrence (e.g. Fragkoulidis et al., 2018). Given the influence of this weather phenomenon over SA and their increased frequency of occurrence (Mulovedzi, 2017), it warrants some analysis of the structure of RWPs associated with heatwaves. Figure 5.13 depicts the evolution of a pre-existing RWP located over the SACZ 10 days (Figure 5.13 (a)) prior to the onset of the composite heatwave. This system is characterised by a deep trough-ridge-trough configuration of disturbances as indicated by the PV streamers associated with it.

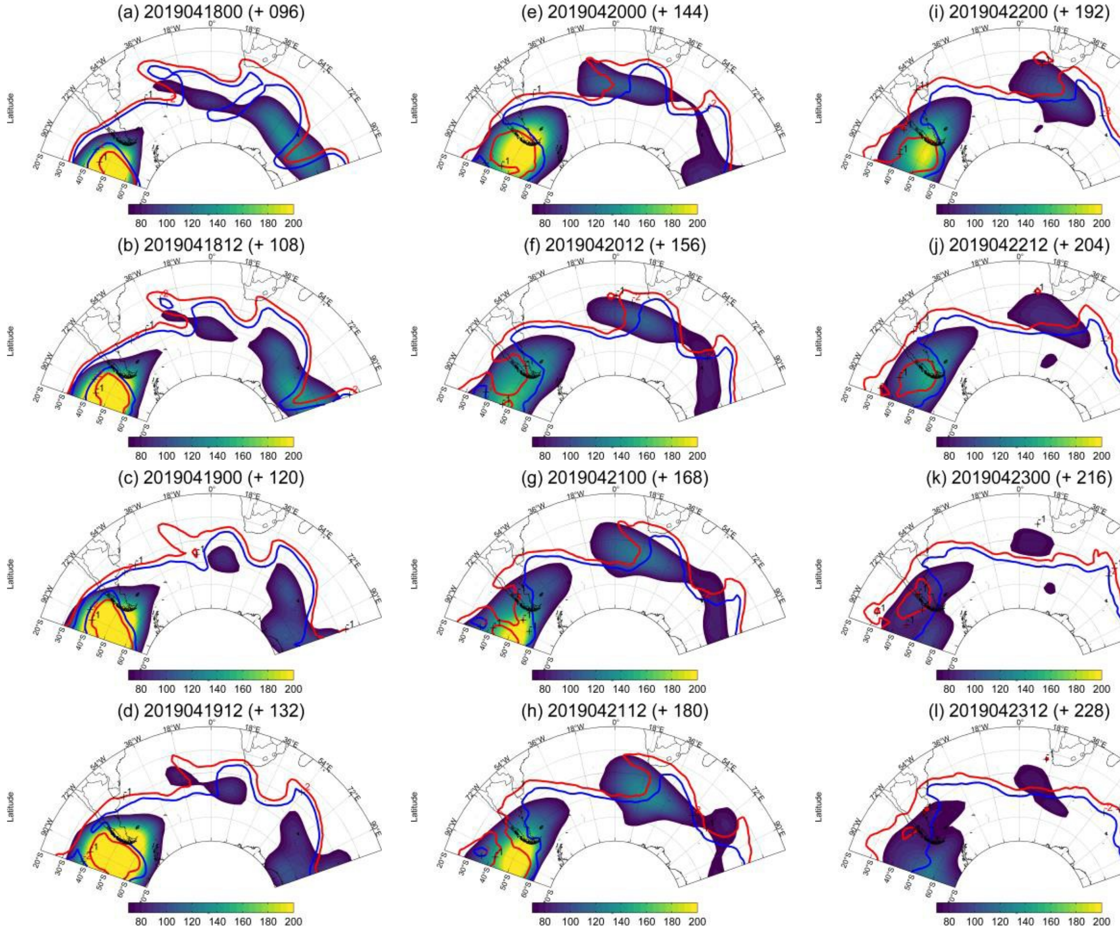

Figure 5.12: *NCEP EPS ensemble mean forecast of FAWA (shaded) and PV (thin contours). The forecast was produced on the 14th of April 2019 to detect the evolution of an RWP associated with CoL formation over SA. FAWA units are ms*$^{-1}$ *and the PV contours are in PVU (red = -1 and blue = -2) on* θ_{330K}.

The RWP then propagates downstream towards the South Atlantic, west of SA and gradually decays following the established path of the previously identified baroclinic RWP along the wave guide. Interestingly, with the gradual dissipation of the RWP, the overall system spreads eastward so that the ridge propagates slowly while positioned over SA. This sequence of events is favourable for the occurrence of heatwaves due to the positioning of the upper-tropospheric ridge overland, which is associated with subsidence. As a result, the quasi-stationary ridge persists beyond t = 0 h, which is the approximated onset of the heatwave events. The fact that the initial RWP located upstream was associated with the occurrence of a heatwave downstream is an interesting observation, and thus may present the opportunity to diagnose, and predict heatwaves from a RWP perspective.

5.5 Summary

This study sought to investigate some of the characteristics associated with RWPs affecting weather processes over SA. This is a consequence of a recent study (see Wirth et al., 2018 review) on the possibility of the utility of RWPs improving medium-range forecasts of extreme weather phenomena.

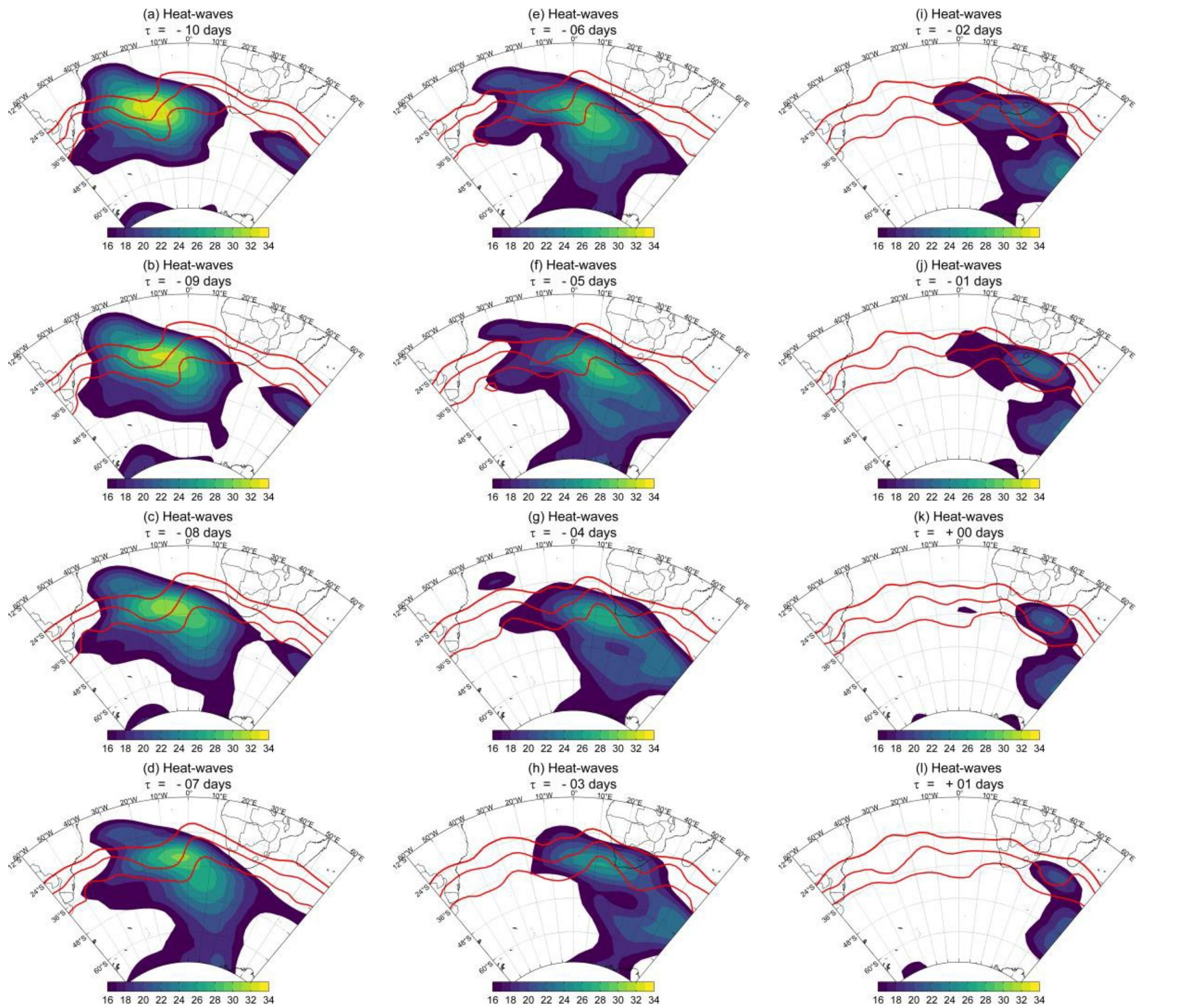

Figure 5.13: *11 day evolution of composite means of 11 heatwave events over SA diagnosed using FAWA (shaded) and PV (thin contours) on θ_{330K}. FAWA units are ms^{-1} and the PV contours are in PVU (-1.3, -2 and -3 PVU) on θ_{330K}.*

The objectives were as follows:

1. to objectively identify RWPs using a suitable diagnostic,
2. to produce a climatological and variability pattern of RWPs in the SA domain,
3. to elucidate the key processes in the life-cycle of the RWPs, and lastly
4. to assess the feasibility of the utility of RWPs in the forecasting process.

To achieve the first objective, we utilized a FAWA diagnostic (Ghinassi et al., 2018) together with NCEP reanalysis 2 data. Closed, concentric contours of the calculated FAWA (using the methods of Ghinassi et al., 2018) field were objectively identified as RWPs, with further subjective thresholds subjectively imposed to discard weak structures. The climatological characteristic was then deduced from the populated database resulting from the first objective to satisfy the second objective. Following this, composite analysis was conducted to determine the morphology of RWPs in general prior to their consideration relative to the landmass. It was found that the RWPs in question undergo a series of well-known processes (development and termination) in their life cycle. The role of EKE in the development of the RWP was also examined using the framework of Orlanski and Katzfey (1991).

Using this, it was found that the two dominant processes in the evolution of EKE (and indeed the RWP) were the convergence of the ageostrophic geopotential fluxes as well as the baroclinic conversion term. These findings are consistent with Chapter 4 and thus give credence to the schematic produced in the study. It follows then that the findings of that chapter can be extended to general baroclinic RWPs. The wave activity and EKE associated with the RWP was found to emanate from high latitudes w of Brazil towards the SACZ which was found to interact with the extra-tropical disturbance. Later on, the developing system undergoes anticyclonic RWB as it begins to decay in line with the conceptual model of a baroclinic RWP (Wirth et al., 2018). The source of the RWB was further probed using wave refraction arguments inspired by the findings of Summarises and Reeder (2017). In this study, it was found that the RWB occurs in the vicinity of the critical latitude upon which the z^0 and v^0 contours behaved similarly to those observed in Summarises and Reeder (2017) during wave-reflection southwest of Africa. However, this aspect of the discussion was left open-ended given the subjectivity of the analysis. Lastly, the structures of heatwave events and CoLs were established from a filtered FAWA perspective. These two systems were chosen on the basis of their known extreme impact on society. Regarding heatwaves, it was found by computing the composite means of 9 identified events of a RWP that preceded the onset of these events. This ultimately gives credence to the possibility of utilising RWPs in the forecasting of heatwaves. Furthermore, the evolution of the well-known 22 April 2019 CoL is also observed in NCEP EPS data to mimic and simulate a forecasting procedure of a CoL based on the objective identification of RWPs. It was found that the key aspects of the evolution of a baroclinic RWP making its way to the SAT domain were visible and well-identified in the forecast data. The implication of these findings is thus important for the purpose of the objective identification of high impact systems such as CoLs and heatwaves over SA. As such, Figure 5.14 illustrates an example of a possible routine framework in utilising NWP products together with the FAWA to objectively identify RWPs in forecasting data.

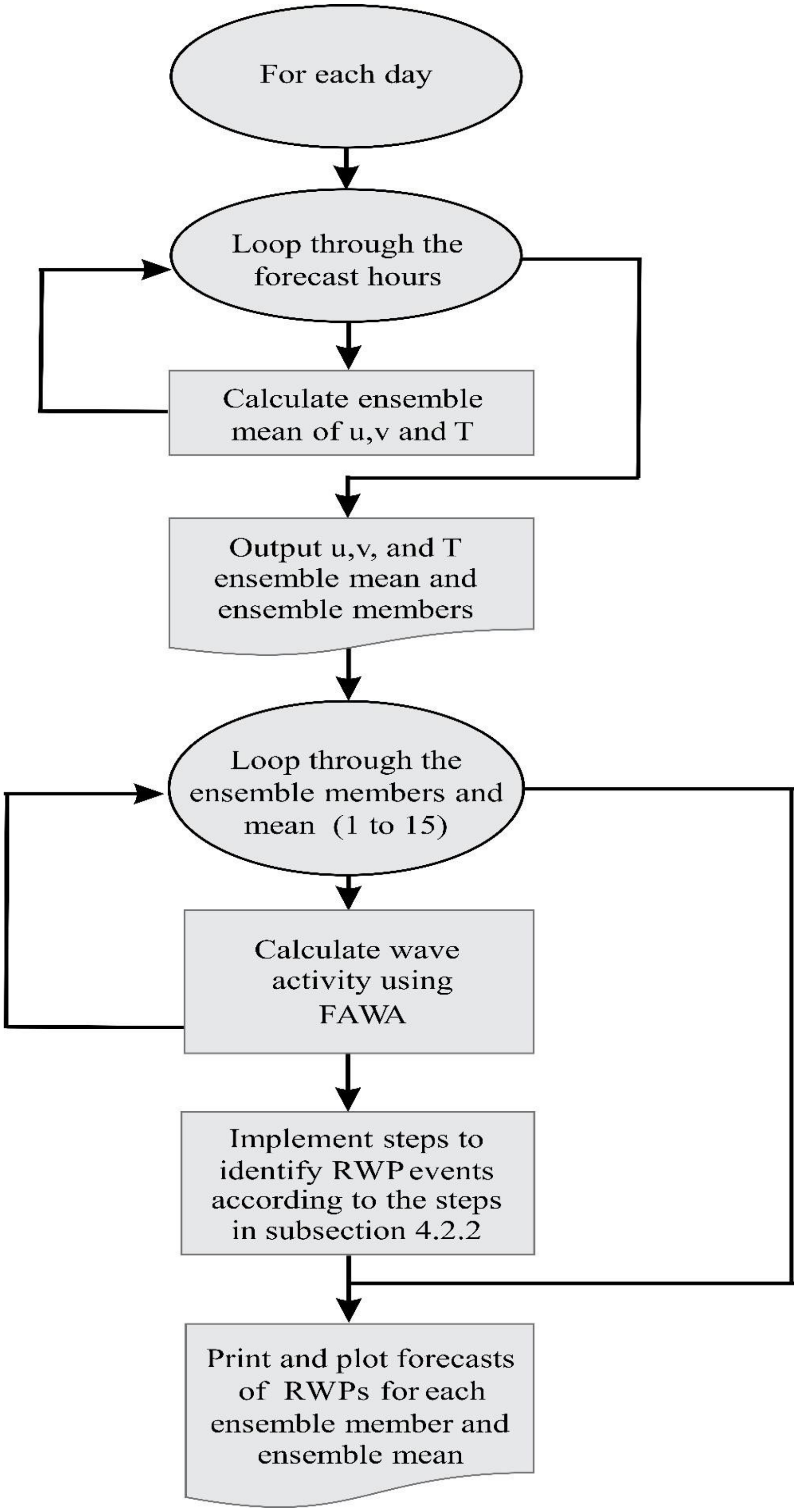

Figure 5.14: *An illustration of a possible forecasting procedure for RWPs.*

6

Conclusions and recommendations

6.1 Conclusions

Medium-range forecasts (MRF) suffer from inherent model biases that are caused by inadequate observations, imperfect model physics and an incomplete understanding of the dynamics that underlie the evolution of phenomena. This has profound adverse implications for the predictive skill of atmospheric phenomena, which diminishes rapidly towards the 10-day lead time that marks the end of the MRF time scale. In the South African domain, these biases are most dominant over the surrounding oceans. This could be caused by the fact that there are fewer observations in those areas compared to over the land. The bias also increases in strength as a function of lead time because the validity of the initial conditions diminishes with time. The bias correction measure that was implemented in this project was efficient in removing these biases. Its main advantage is that it is easy to implement and therefore may be used operationally without increasing the computational time required to post-process MRF data.

As noted above, one of the contributing factors to limitations of predictability of phenomena is an incomplete understanding of the dynamics of phenomena, and in the case of this project, rainfall producing weather systems. This was highlighted in THe Observing System Research and Predictability EXperiment (THORPEX) of the WMO. As such, one of the objectives of the project was to understand aspects of the dynamics of ridging highs and cut-off low pressure systems. Ridging high pressure systems are not, by themselves, rainfall producing systems. Their main function is to transport moisture from the Southwest Indian Ocean into South Africa. It was revealed in this project that ridging high pressure systems are induced by lower stratospheric dynamical processes that are characterised by Rossby wave breaking (RWB). These RWB events bring about high potential vorticity (PV) anomalies, that are communicated towards the surface by means of vertical coupling, to induce the ridging process. RWB events are also embedded in Rossby wave trains or packets that develop in the South American region, and then propagates in a north-easterly direction to the South African domain. This means that ridging highs are regulated by large scale propagating waves.

The processes involved in how ridging highs transport moisture into South Africa were also considered. The flow that underlies the moisture fluxes was decomposed into its ageostrophic and geostrophic components. On the basis of this decomposition, it was shown that moisture that enters the country from the Southwest Indian Ocean originates from different parts of the ocean. The ageostrophic moisture divergence is mostly confined to the coast and it is located south of 30°S right through the ridging process. As a result, the ageostrophic moisture fluxes enter South Africa along the southern coast and roughly follow the geometry of the coast. The geostrophic fluxes originate from further afield and enter the country mostly from the southern parts of the Mozambique Channel, and branch out anticyclonically into the interior of South Africa. A second branch turns cyclonically so that the moisture is transported towards Botswana and Namibia.

Ridging high pressure systems bring the moisture that COLs require to cause rainfall over the country. It was established in earlier studies that the latter is preceded by RWB and that the PV anomaly that characterises them is evidence of stratospheric air known to dominate in their closed circulation. The wave breaking process is induced by the jet streak that moves eastward in the midlatitudes. This jet is propelled by the redistribution of zonal momentum by the flow from the jet entrance to the exit. It also changes orientation due to poleward advection of zonal momentum at its entrance, and an equatorward momentum advection at the exit. This eastward movement of the jet is coupled to the downstream development process because as the jet is propelled, the eddy kinetic energy moves along with it. This energy centre intensifies as the waves break as a result of the increasing barotropic shear and strain rate. The energy centre saturates just before the formation of the closed circulation that characterises the COLs and starts losing its strength thereafter. This energy is lost from the midlatitudes by means of ageostrophic geopotential fluxes that transport or radiate energy downstream into the COL region. The energy centre that develops in this region reaches a maximum as the closed circulation forms. It follows from this sequence of events where the RWB plays the critical role of inducing the supergeostrophic flow and positive geopotential anomalies that are central to downstream development during COL evolution.

Characteristics of Rossby wave packets (RWPs) affecting South African weather processes have also been examined using NCEP reanalysis 2 data. RWPs were diagnosed objectively from the latest filtered finite-amplitude wave activity diagnostic in isentropic coordinates. Through composite analysis, the morphological characteristics of such RWPs were established. It was found that the evolution of RWPs in question is consistent with the known life-cycle of baroclinic RWPs. The development phase involved the northeastward propagation of an initial disturbance, followed by zonal propagation briefly before the onset of the termination stage indicated by Rossby wave breaking. Subsequently, the RWP propagates approximately south-eastward. In addition, the climatology of RWPs revealed that most events occur during the transition seasons, with a majority of the events being detected within the South Indian Ocean domain. The evolutionary characteristics of RWPs were also analysed using an eddy kinetic energy diagnostic. The evolution of the eddy kinetic energy essentially diagnoses the ensuing downstream development associated with baroclinic waves. Key processes involved in the evolution of the eddy kinetic energy structure were found to be a baroclinic conversion and a divergence of the ageostrophic geopotential fluxes. The downstream development found for RWP is more general than that found in COLs, as indicated by the differences in the orientation of the eddy kinetic energy centres.

Studying these dynamical processes is made possible by the objective methods for identifying the weather systems in large datasets that were specially developed for this project. This presents an opportunity to develop a MRF post-processing procedure that enables objective event-based medium-range forecasts and consider the dynamics that precede the events to give credence to the forecasts, thereby potentially improving the predictability of weather systems. Event-based forecasts show that ridging highs are highly predictable, as confirmed by the RWB forecasts associated with them. The situation is different for COLs. Event-based MRF forecasts of COLs exhibit low levels of predictability, but downstream development is more predictable due to one thing, it occurs earlier in the forecast.

The utility of RWPs as a diagnostic tool was explored through two examples. The first showed that the onset of 11 composited heatwave events was preceded by a pre-existing RWP structure located in the vicinity of the SACZ. Furthermore, it was shown that the 22 April 2019 cut-off low event was also associated with a RWP that developed at an earlier time upstream. It was shown that the ensemble mean of a forecast issued on 14 April 2019 at 00Z by the NCEP EPS system revealed the development of the RWP at about t = + 96 hours of the forecast window.

6.2 Recommendations

This project has successfully implemented some aspects of predictability that were proposed in the THORPEX programme. However, our understanding of the dynamics that underlie the evolution of South African weather systems is far from being complete.

The first recommendation is that a systematic study of the weather systems should be undertaken. This could begin by first establishing the current state of the art of synoptic meteorology knowledge in South Africa, after which the dynamics can then be studied.

A more systematic research project to study the predictability of weather systems is required. This will require considerable investment into data archive resources because of the extensive nature of the MRF data. This predictability study should be based on the findings of the first recommendation.

Finally, event-based studies should be considered for early warning systems. Organisations such as the SAWS should consider these types of forecasts in their bouquet of product offering.

REFERENCES

1. Ambrizzi, T., Hoskins, B. J., & Hsu, H. H. (1995). Rossby wave propagation and teleconnection patterns in the austral winter. Journal of Atmospheric Sciences, 52(21), 3661-3672.
2. Berbery, E. H., & Lozano, A. (1991). Regional characteristics of persistent height anomalies in the Atlantic and South Pacific oceans. Annals of VI Congremet, 153-154.
3. Berbery, E. H., & Vera, C. S. (1996). Characteristics of the Southern Hemisphere winter storm track with filtered and unfiltered data. Journal of Atmospheric Sciences, 53(3), 468-481.
4. Carvalho, L. M., Jones, C., & Liebmann, B. (2004). The South Atlantic Convergence Zone: Intensity, form, persistence, and relationships with intraseasonal to interannual activity and extreme rainfall. Journal of Climate, 17(1), 88-108.
5. Chang, E. K. (1993). Downstream development of baroclinic waves as inferred from regression analysis. Journal of the Atmospheric Sciences, 50(13), 2038-2053.
6. Chang, E. K. (2001). The structure of baroclinic wave packets. Journal of the Atmospheric Sciences, 58(13), 1694-1713.
7. Danielson, R. E., Gyakum, J. R., & Straub, D. N. (2006). A case study of downstream baroclinic development over the North Pacific Ocean. Part ii: Diagnoses of eddy energy and wave activity. Monthly Weather Review, 134(5), 1549-1567.
8. Dee D. P., Uppala S.M., Simmons A.J., Berrisford P., Poli P., Kobayashi S., Andrae U., Balmaseda M. A., Balsamo G., Bauer P., Bechtold P., Beljaars A. C., van de Berg L., Bidlot J., Bormann N., Delsol C., Dragani R., Fuentes M., Geer A. J., Haimberger L., Healy S. B., Hersbach H., Hlm E. V., Isaksen L., Kllberg P., Khler M., Matricardi M., McNally A. P., MongeSanz B. M., Morcrette J., Park B., Peubey C., de Rosnay P., Tavolato C., Thpaut J. & Vitart F. (2011) The ERA Interim reanalysis: configuration and performance of the data assimilation system. Q J R Meteorol Soc 137: 553-597.
9. Dong L., Colucci S. J. (2015) The Role of Non-quasigeostrophic Forcing in Southern Hemisphere Blocking Onsets. Mon Weather Rev, 143: 1455-1471.
10. Dyson L. (2015) A heavy rainfall sounding climatology over Gauteng South Africa, using self-organising maps. Clim Dyn, 45: 3051-3065.
11. Favre A., Hewitson B., Lennard C., Cerezo-Mota R., Tadross M. (2013) Cut-off lows in the South Africa region and their contribution to precipitation. Clim Dyn 41: 2331-2351.
12. Fragkoulidis, G., Wirth, V., Bossmann, P., & Fink, A. H. (2018). Linking Northern Hemisphere temperature extremes to Rossby wave packets. Quarterly Journal of the Royal Meteorological Society, 144(711), 553-566.
13. Gan, M. A., & Rao, V. B. (1991). Surface cyclogenesis over South America. Monthly Weather Review, 119(5), 1293-1302.

14. Ghinassi, P., Fragkoulidis, G., & Wirth, V. (2018). Local finite-amplitude wave activity as a diagnostic for Rossby wave packets. Monthly Weather Review, 146(12), 4099-4114.

15. Glatt, I., & Wirth, V. (2014). Identifying Rossby wave trains and quantifying their properties. Quarterly Journal of the Royal Meteorological Society, 140(679), 384-396.

16. Hakim, G. J. (2003). Developing wave packets in the north pacific storm track. Monthly Weather Review, 131(11), 2824-2837.

17. Hakim, G. J. (2005). Vertical structure of midlatitude analysis and forecast errors. Monthly Weather Review, 133(3), 567-578.

18. Harvey, B. J., Methven, J., & Ambaum, M. H. (2016). Rossby wave propagation on potential vorticity fronts with finite width. Journal of Fluid Mechanics, 794, 775-797.

19. Holton, J. R. (2004). An introduction to dynamic meteorology (Vol. 41) (No. 5). AAPT.

20. Hoskins, B. J., McIntyre, M. E., & Robertson, A. W. (1985). On the use and significance of isentropic potential vorticity maps. Quarterly Journal of the Royal Meteorological Society, 111(470), 877-946.

21. Hoskins, B. J., & Ambrizzi, T. (1993). Rossby wave propagation on a realistic longitudinally varying flow. Journal of Atmospheric Sciences, 50(12), 1661-1671.

22. Hoskins, B. J., & Hodges, K. I. (2005). A new perspective on Southern Hemisphere storm tracks. Journal of Climate, 18(20), 4108-4129.

23. Hovmöller, E. (1949). The trough-and-ridge diagram. Tellus, 1(2), 62-66.

24. Huang, C. S., & Nakamura, N. (2016). Local finite-amplitude wave activity as a diagnostic of anomalous weather events. Journal of the Atmospheric Sciences, 73(1), 211-229.

25. Liebmann, B., Kiladis, G. N., Marengo, J., Ambrizzi, T., & Glick, J. D. (1999). Submonthly convective variability over South America and the South Atlantic convergence zone. Journal of Climate, 12(7), 1877-1891.

26. Mulovhedzi, P. T. (2017). Towards a heat-watch warning system for South Africa for the benefit of the health sector (Masters Dissertation, University of Pretoria).

27. Morgan, M. C., & Nielsen-Gammon, J. W. (1998). Using tropopause maps to diagnose midlatitude weather systems. Monthly Weather Review, 126(10), 2555-2579. Kunz, A., Konopka, P., Muller, R., & Pan, L. L. (2011). Dynamical tropopause based on isentropic potential vorticity gradients. Journal of Geophysical Research: Atmospheres, 116(D1).

28. Ndarana, T., & Waugh, D. W. (2010). The link between cut-off lows and Rossby wave breaking in the Southern Hemisphere. Quarterly Journal of the Royal Meteorological Society, 136(649), 869-885.

29. Necco, G. V. (1982). Behaviour of the cyclonic vortices in the South American region during FGGE. Cyclogenesis (Comportamiento de vortices ciclonicos en el area sudamericana durante el FGGE Cicligenesis). Meteorologica, 8, 7-20.

30. Nielsen-Gammon, J. W., & Lefevre, R. J. (1996). Piecewise tendency diagnosis of dynamical processes governing the development of an upper-tropospheric mobile trough. Journal of the Atmospheric Sciences, 53(21), 3120-3142.

31. Nie, Y., Zhang, Y., Yang, X. Q., & Ren, H. L. (2019). Winter and Summer Rossby Wave Sources in the CMIP5 Models. Earth and Space Science, 6(10), 1831-1846.

32. O’Brien, L., & Reeder, M. J. (2017). Southern hemisphere summertime Rossby waves and weather in the Australian region. Quarterly Journal of the Royal Meteorological Society, 143(707), 2374-2388.

33. O’Kane, T. J., Risbey, J. S., Monselesan, D. P., Horenko, I., & Franzke, C. L. (2016). On the dynamics of persistent states and their secular trends in the wave guides of the Southern Hemisphere troposphere. Climate Dynamics, 46(11), 3567-3597.

34. Orlanski, I., & Katzfey, J. (1991). The life cycle of a cyclone wave in the southern hemisphere. Part i: Eddy energy budget. Journal of the Atmospheric Sciences, 48(17), 1972-1998.

35. Orlanski, I., & Sheldon, J. (1993). A case of downstream baroclinic development over western North America. Monthly Weather Review, 121(11), 2929-2950.

36. Palmen, E., & Newtown, C. W. (1979) Atmospheric circulation systems, their structure and physical interpretation. Academic Press.

37. Peters, D., & Waugh, D. W. (2003). Rossby wave breaking in the Southern Hemisphere wintertime upper troposphere. Monthly Weather Review, 131(11), 2623-2634.

38. Reason, C. J., Mysak, L. A., & Cummins, P. F. (1987). Generation of annual-period Rossby waves in the South Atlantic Ocean by the wind stress curl. Journal of Physical Oceanography, 17(11), 20302042.

39. Reboita, M. S. (2008). Extratropical cyclones over the South Atlantic Ocean: climatic simulation and sensibility experiments. University of Sao Paulo, Sao Paulo, 294.

40. Reboita, M. S., Da Rocha, R. P., Ambrizzi, T., & Sugahara, S. (2010). South Atlantic Ocean cyclogenesis climatology simulated by regional climate model (RegCM3). Climate Dynamics, 35(7-8), 1331-1347.

41. Robertson, A. W., & Mechoso, C. R. (2000). Interannual and interdecadal variability of the South Atlantic convergence zone. Monthly Weather Review, 128(8), 2947-2957.

42. Sardeshmukh, P. D., & Hoskins, B. J. (1988). The generation of global rotational flow by steady idealized tropical divergence. Journal of Atmospheric Sciences, 45(7), 1228-1251.

43. Sellwood, K. J., Majumdar, S. J., Mapes, B. E., & Szunyogh, I. (2008). Predicting the influence of observations on medium-range forecasts of atmospheric flow. Quarterly Journal of the Royal Meteorological Society: A Journal of the Atmospheric Sciences, Applied Meteorology and Physical Oceanography, 134(637), 2011-2027.

44. Shapiro, M. A., & Thorpe, A. J. (2004). THORPEX International Science Plan. WMO/TD, 1246.

45. Shimizu, M. H., & de Albuquerque Cavalcanti, I. F. (2011). Variability patterns of Rossby wave source. Climate Dynamics, 37(3-4), 441-454.

46. Simmons, A. J., & Hoskins, B. J. (1978). The life cycles of some nonlinear baroclinic waves. Journal of Atmospheric Sciences, 35(3), 414-432.

47. Sinclair, M. R. (1996). Reply to comments on ”Climatology of cyclogenesis for the Southern Hemisphere”. Monthly Weather Review, 124(11), 2615.

48. Szunyogh, I., Toth, Z., Zimin, A. V., Majumdar, S. J., & Persson, A. (2002). Propagation of the effect of targeted observations: The 2000 winter storm reconnaissance program. Monthly Weather Review, 130(5), 1144-1165.

49. Tennant, W. (2004) Considerations when using pre-1979 NCEP/NCAR reanalysis in the southern hemisphere. Geophys Res Lett 31: L11112.

50. Takaya, K., & Nakamura, H. (2001). A formulation of a phase-independent wave-activity flux for stationary and migratory quasigeostrophic eddies on a zonally varying basic flow. Journal of the Atmospheric Sciences, 58(6), 608-627.

51. Thorncroft, C. D., Hoskins, B. J., & McIntyre, M. E. (1993). Two paradigms of baroclinic-wave life-cycle behaviour. Quarterly Journal of the Royal Meteorological Society, 119(509), 17-55.

52. Trenberth, K. E., Branstator, G. W., Karoly, D., Kumar, A., Lau, N. C., & Ropelewski, C. (1998). Progress during TOGA in understanding and modeling global teleconnections associated with tropical sea surface temperatures. Journal of Geophysical Research: Oceans, 103(C7), 14291-14324.

53. Warner, T. T. (2010). Numerical weather and climate prediction. Cambridge University Press.

54. Wirth, V., Riemer, M., Chang, E. K., & Martius, O. (2018). Rossby wave packets on the midlatitude wave guide — a review. Monthly Weather Review, 146(7), 1965-2001.

55. Zeng, Q. C. (1983). The evolution of a Rossby wave packet in a three-dimensional baroclinic atmosphere. Journal of Atmospheric Sciences, 40(1), 73-84.

56. Zheng, M., Chang, E. K., & Colle, B. A. (2013). Ensemble sensitivity tools for assessing extratropical cyclone intensity and track predictability. Weather and Forecasting, 28(5), 1133-1156.

57. Zimin, A. V., Szunyogh, I., Patil, D., Hunt, B. R., & Ott, E. (2003). Extracting envelopes of Rossby wave packets. Monthly Weather Review, 131(5), 1011-1017.